PHOTONICS INSIGHTS

# Spatiotemporal optical wavepackets: from concepts to applications

**Xin Liu,[a,b,c] Qian Cao,[a,d] and Qiwen Zhan[a,d,e,f,*]**

[a]School of Optical-Electrical and Computer Engineering, University of Shanghai for Science and Technology, Shanghai, China
[b]Shandong Provincial Engineering and Technical Center of Light Manipulations and Shandong Provincial Key Laboratory of Optics and Photonic Device, School of Physics and Electronics, Shandong Normal University, Jinan, China
[c]Collaborative Innovation Center of Light Manipulations and Applications, Shandong Normal University, Jinan, China
[d]Zhangjiang Laboratory, Shanghai, China
[e]Westlake Institute for Optoelectronics, Hangzhou, China
[f]International Institute for Sustainability with Knotted Chiral Meta Matter (WPI-SKCM2), Hiroshima University, Hiroshima, Japan

**Abstract.** Spatiotemporal optical wavepackets refer to light fields with sophisticated structures in both space and time. The ability to produce such spatiotemporally structured optical wavepackets on demand attracted rapidly increasing interest as it may unravel a variety of fundamental physical effects and applications. Traditionally, pulsed laser fields are treated as spatiotemporally separable waveform solutions to Maxwell's equations. Recently, more generalized spatiotemporally non-separable solutions have gained attention due to their remarkable properties. This review aims to provide essential insights into sculpting light in the space–time domain to create customized spatiotemporal structures and highlights the recent advances in the generation, manipulation, and characterization of increasingly complex spatiotemporal wavepackets. These spatiotemporally non-separable light fields with diverse geometric and topological structures exhibit unique physical properties during propagation, focusing, and light–matter interactions. Various novel results and their broad potential applications as well as an outlook for future trends and challenges in this field are presented.

Keywords: spatiotemporal wavepacket; ultrafast pulse; spatiotemporal optical vortex; transverse orbital angular momentum; optical topology; pulse shaper; light manipulation; spatiotemporal coupling.

Received Sep. 27, 2024; revised manuscript received Nov. 20, 2024; accepted Dec. 6, 2024; published online Dec. 28, 2024.



[DOI: 10.3788/PI.2024.R08]

## 1 Introduction

The term "structured light" (also termed tailored light, shaped light, customized light, or sculpted light) refers to light fields that are engineered to have specific spatial or temporal patterns and degrees of freedom (DoFs)[1–11], such as their intensity, phase, polarization (or spin of photon), frequency (or wavelength), time, and coherence. Unlike a standard laser beam, which has a uniform (plane wave) or Gaussian distribution of light intensity, structured light can be manipulated to exhibit a variety of complex forms in the space or time domain. With the rapid advancement of optical shaping technologies and laser sources, manipulating the spatial DoF has also experienced significant maturation, leading to the development of new classes of optical beams. Consequently, a variety of spatially structured light fields have been proposed and experimentally realized, including Airy beams[12–18], Bessel beams[19–25], Weber beams[26–28], Mathieu beams[29,30], Ince–Gauss beams[31–34], Caustic beams[35–41], Laguerre–Gauss (LG) beams[42–47], and Hermite–Gauss (HG) beams[48–53]. These beams exhibit distinctive optical properties, such as non-diffraction[54,55], self-bending[13,14,17], self-healing[56,57], and the ability to carry orbital angular momentum (OAM)[42–44], which are associated with their specific spatial intensity distributions and phase structures within their two-dimensional (2D) transverse spatial profile, enabling precise control over light evolution dynamics. When accounting for the polarization characteristics of light, the spatial polarization of structured light can be precisely engineered into

*Address all correspondence to Qiwen Zhan, qwzhan@usst.edu.cn

various complex distributions[58–61], to alter the spin property of the photon[62,63]. Two notable examples of broad interest are the optical vortex carrying OAM[42–44,64–67] and cylindrical vector beams[58,59]. In addition, the spatial coherence of light, a second-order statistical optical parameter, offers an additional DoF that can be harnessed for light shaping[68–71]. By controlling these spatial DoFs, one can further refine the beam's properties, enabling more precise manipulation in applications ranging from optical imaging[72–76], microscopy[77,78], micro-particle trapping[79,80], optical computing[81–83], optical communication[84,85], and laser processing[86,87] to quantum information[88,89], leading to practical applications with economic impact. Meanwhile, advances in ultrafast lasers and pulse shaping techniques have enabled the generation of optical pulses with nearly arbitrary waveforms in their one-dimensional (1D) temporal profile[90–93]. Temporal shaping of light, particularly in the ultrafast domain—such as in chirped pulse amplification[94,95], optical frequency combs[96–98], and pulse train generation[99–101]—has already proven valuable across a wide range of applications. These advancements continue to push the boundaries of light manipulation for scientific and technological innovation.

Joint sculpting light in the three-dimensional (3D) spatiotemporal domain by accessing its temporal and spatial DoFs is termed spatiotemporally structured wavepackets. Research on spatiotemporal wavepackets (STWPs) has made significant progress in recent years, driven by advancements in temporal shaping and spatial structure light. Traditionally, STWPs are treated as spatiotemporally separable entities, with their spatial and temporal components considered independently in the space–time domain, with notable examples including the extended families of focus-wave modes[102,103], X-waves[104–108], O-waves[109–112], Airy–Bessel wavepackets[113], and other forms[114–116], all of which simultaneously resist both diffraction and dispersion effects. In recent experimental demonstrations (after 2017), STWPs have been synthesized with specific correlations among various DoFs. By leveraging these emerging techniques, temporal frequencies can be entangled with their corresponding spatial wavevectors, enabling the generation of diverse, localized spatiotemporal structures such as spatiotemporal optical vortices (STOVs)[117–122], space–time light sheet wavepackets[123–126], space–time helical wavepackets[127,128], and toroidal pulses[129,130]. These emerging STWPs exhibit unique physical properties, such as transverse OAM, diffraction-free propagation, tunable group velocity, and time-varying optical characteristics, due to the existence of space–time couplings where spatial and temporal effects become entangled. This leads to distinct behavior during propagation, focusing, and interaction with matter, offering new avenues for controlling light in advanced applications. In this review, we provide a comprehensive overview of the recent developments in spatiotemporally structured wavepackets, covering fundamental concepts, methods for their generation and manipulation, techniques for characterization, as well as their applications, challenges, and future opportunities (Fig. 1).

This review highlights the rapid advancements over the past 5 years in the generation, manipulation, characterization, and applications of spatiotemporally structured wavepackets, along with the novel physics emerging from these developments, as illustrated in Fig. 1. Unlike conventional wavepackets, where spatial and temporal degrees of freedom are treated separately, this review focuses on wavepackets modulated through coupled spatial-temporal interactions.

Section 2 covers the fundamentals of shaping STWPs and introduces cutting-edge techniques for synthesizing them, whether spatially, temporally, or in a spatiotemporally coupled manner. These methods combine ultrafast pulse manipulation with spatial beam shaping, leveraging Fourier optics principles. Key technologies include 2D pulse shapers, multi-plane light conversion (MPLC) devices, metasurfaces, and nanophotonics platforms, each offering precise control over the wavepacket's structure for novel applications across various domains.

Section 3 delves into recent breakthroughs in the generation and manipulation of novel STWPs, focusing on several key types. These include STOVs with transverse OAM, non-diffracting space–time light sheets, helical wavepackets with time-varying optical properties, and vectorial electric-magnetic toroidal pulses. This section also involves significant advancements in the nonlinear regime of STOVs and other intriguing wave phenomena that arise in these contexts. Additionally, it explores the realization of space–time optical topologies enabled by STWPs, examining how these complex wave structures have led to new opportunities in optical manipulation and control. These pioneering developments are shaping the future of optical science, providing insights into both fundamental physics and potential applications.

Section 4 is devoted to the characterization methods for STWPs, emphasizing the reliable retrieval of both intensity and phase information in the space–time domain. Accurate characterization of ultrafast wavepackets is essential for understanding and controlling their complex dynamics. This section outlines advanced techniques for capturing the full spatiotemporal profile of STWPs, including temporally sliced 3D reconstructions and single-shot 2D reconstructions using both linear and nonlinear approaches. By combining spatial and temporal diagnostics, these methods enable comprehensive insight into the behavior of STWPs and their underlying physics.

Section 5 presents some of the emerging applications of STWPs across various fields, including light–matter interaction, data encoding and transmission, optical information processing, and superintense fields. These novel applications demonstrate the versatility of STWPs in enabling new ways to control light and manipulate information, offering promising advances in both fundamental research and technological innovation.

Finally, Sec. 6 summarizes recent advancements in spatiotemporally structured wavepackets and discusses future trends, including ultracompact synthesis devices, modal sorting/detection/multiplexing/demultiplexing, quantum control and entanglement, more complex space–time topologies, and high-dimensional wavepackets, as well as the nonlinear microscope and laser processing. This section also explores emerging opportunities and challenges, proposing potential solutions to overcome technical barriers. Additionally, it provides a forward-looking perspective on the future of spatiotemporal light sculpting, envisioning its role in shaping next-generation optical technologies.

## 2 Fundamentals of Spatiotemporal Wavepackets

Due to their ultrafast time variation and ultrashort pulse duration, directly manipulating the time dimension of these wavepackets is challenging. Traditional pulse modulation typically occurs through the time Fourier spectrum. However, STWPs feature an inseparable 3D space–time structure. In the following

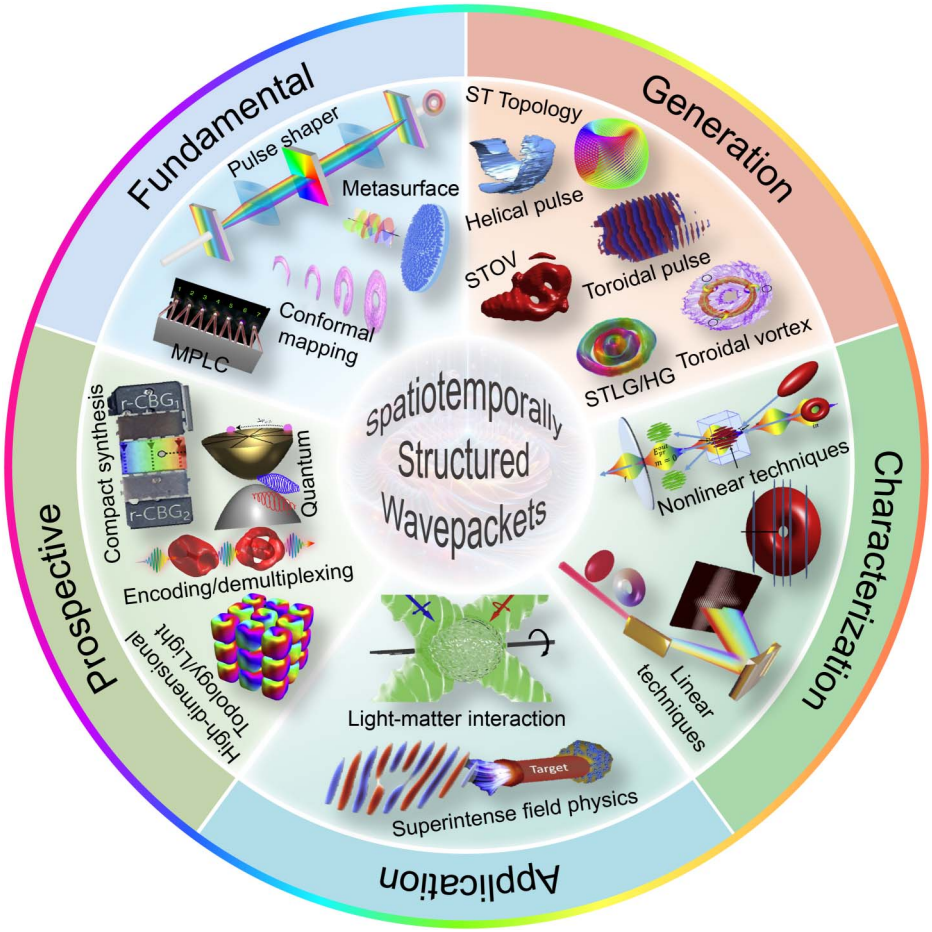


**Fig. 1** Schematic illustration of recent advances in spatiotemporally structured wavepackets.

sections, we review and summarize the principles, methods, and common configurations for manipulating STWPs.

### 2.1 Wave Equations and Space–Time Duality

From Maxwell's equations, the evolution dynamic of a scalar spatiotemporal electric field $U(x,y,z;t)$ in a homogeneous-permittivity and source-free medium is described by

$$\nabla^2 U(x,y,z;t) - \frac{1}{c^2}\frac{\partial^2 U(x,y,z;t)}{\partial t^2} = 0, \tag{1}$$

where $\nabla^2 = \frac{\partial^2}{\partial x^2} + \frac{\partial^2}{\partial y^2} + \frac{\partial^2}{\partial z^2}$. $c = c_0/n(\omega)$ represents the speed of light in a medium with refractive index $n(\omega)$ and $c_0$ is the light speed in vacuum. Equation (1) is the scalar wave equation. In this review, we adopt the common model of assigning $z$ to be the wave propagation axis. Under the slowly varying envelop approximation ($|\partial^2 U/\partial t^2| \ll |\omega \partial U/\partial t| \ll |\omega^2 U|$) and paraxial condition ($|\partial^2 U/\partial z^2| \ll |k\partial U/\partial z| \ll |k^2 U|$), the complex field of $U(x,y,z;t)$ can be rewritten as at a carrier frequency $\omega_0$:

$$U(x,y,z;t) = \Psi(x,y,z;t)\exp(i\omega_0 t - ik_0 z), \tag{2}$$

where $\Psi(x,y,z;t)$ stands for the envelope of a pulsed beam, also called wavepacket. If $\Psi(x,y,z;t) \neq \Psi_S(x,y,z) \times \Psi_T(t)$, such STWPs are considered entangled in both space and time, making them spatiotemporally non-separable—a property known as spatiotemporal coupling[122,125,134]. $k_0 = \omega_0/c_0 = 2\pi/\lambda_0$ is the propagation constant. Substituting Eq. (2) into Eq. (1) and considering the above assumptions, we can obtain the following equation:

$$\nabla_T^2 \Psi(x,y,z;t) + i2k_0\left(\frac{\partial}{\partial z} + \frac{1}{c}\frac{\partial}{\partial t}\right)\Psi(x,y,z;t) = 0, \tag{3}$$

where $\nabla_T^2 = \partial^2/\partial x^2 + \partial^2/\partial y^2$ denotes the transverse Laplacian operator. Based on the duality of space and time, the temporal evolution of a pulse in a dispersive medium can be described by

$$\frac{\partial^2}{\partial t^2}\Psi(z;t) + i\frac{2}{\beta_2}\left(\frac{\partial}{\partial z} + \frac{1}{v_g}\frac{\partial}{\partial t}\right)\Psi(z;t) = 0, \tag{4}$$

where $\beta_2$ and $v_g$ are the second-order dispersion coefficient and the group velocity, respectively. Equation (4) only takes into account the linear second-order dispersive effect. By making the change of variables $\zeta = z$, $\tau = t - z/v_g$, and $\partial/\partial t = \partial/\partial\tau$, $\partial/\partial z = \partial/\partial\zeta - c^{-1}\partial/\partial\tau$, Eq. (4) reduces to

$$\frac{\partial^2}{\partial\tau^2}\Psi(z;\tau)+i\frac{2}{\beta_2}\frac{\partial}{\partial z}\Psi(z;\tau)=0. \tag{5}$$

Thus combining Eqs. (3) and (5), the evolution dynamic of an STWP in a dispersive medium is described by

$$\frac{1}{k_0}\nabla_T^2\Psi(x,y,z;\tau)-\beta_2\frac{\partial^2}{\partial\tau^2}\Psi(x,y,z;\tau)+i2\frac{\partial}{\partial z}\Psi(x,y,z;\tau)=0, \tag{6}$$

where $\tau=t-z/v_g$ is the local time frame. When $\beta_2=-1/k_0$, i.e., in an anomalous dispersive medium, Eq. (6) can be reduced to the following symmetric form in both space and time:

$$\frac{\partial^2\Psi}{\partial x^2}+\frac{\partial^2\Psi}{\partial y^2}+\frac{\partial^2\Psi}{\partial\tau^2}+i2\chi^{-1}\frac{\partial\Psi}{\partial z}=0, \tag{7}$$

where $\chi=1/k_0=-\beta_2$. Equation (7) highlights the space–time duality, illustrating an analogy between the paraxial diffraction of spatially confined beams and the dispersion of narrow-band pulses in a medium[131], suggesting the potential to manipulate both within a linear system.

### 2.2 Diffraction Grating and Two-Dimensional Pulse Shaper

Since the oscillation frequency of ultrashort light fields is much higher than that of electro-optic modulators, it is impractical to directly control the timing of light pulses. Instead, the spectrum of the light pulse is typically manipulated using dispersive elements, which in turn allows for control over the temporal waveform of the pulse. The common dispersive elements in the laboratory include diffractive gratings and prisms; they provide an angular dispersion and spatially expand the spectrum of an ultrashort pulse to further modulation. Their cascading and combination can achieve resolved spectroscopy and dispersion control, with the most common approach being the use of grating parallel pairs to achieve pulse compression in the chirped pulse amplification techniques and 3D STWP diagnostic measurement techniques. The common parameters of a commercial grating include blazed wavelength, grooves per millimeter, nominal blaze angle and size, etc. The grating equation for order $m$ is

$$d(\sin\theta_i\pm\sin\theta_d)=m\lambda, \tag{8}$$

where $\theta_i$ and $\theta_d$ are the incident angle and diffractive angle, respectively. $d=1/N$ is the grating period and $N$ is the grooves number. The plus sign indicates that the incident and outgoing lights are on the same side of the grating normal, while the minus sign indicates they are on opposite sides. For a blaze grating, the blaze angle is defined as $\theta_b=(\theta_i+\theta_d)/2$. The real blaze wavelength can be calculated as $\lambda_b=2d\sin\theta_b\cos(\theta_b-\theta_i)/m$. As such, the nominal blaze wavelength $\lambda_{b,\mathrm{Nom}}=2d\sin\theta_b$ and has a relation with $\lambda_b$: $\lambda_b=\lambda_{b,\mathrm{Nom}}\cos(\theta_b-\theta_i)/m$. The angular dispersion of a grating is given by $D_A=d\theta_d/d\lambda=m/d\cos\theta_d$ and the chromatic resolving power at order $m$ is given by $RA=\lambda/\delta\lambda=mN$, where $\delta\lambda$ is the spectral resolution. Parallel placement of grating pairs can provide negative group delay dispersion (GDD) as follows[132]:

$$\mathrm{GDD}=-\frac{\lambda_0^3}{2\pi c^2d^2\cos^3\theta_d}, \tag{9}$$

where $D$ is the distance between gratings.

Given the time scale of the light field, modulation in the frequency domain is the natural choice. A $4f$ pulse shaper is an optical device used to manipulate the spectral characteristics of ultrafast laser pulses. It is called "$4f$" because the setup typically involves the integration of a pair of diffractive gratings, a pair of cylindrical lenses, and a modulator separated by a focus length $f$, as shown in Fig. 2. Figure 2(a) describes a conventional 1D pulse shaper, which involves a 1D array modulator or mask along temporal frequency direction[93]. By adjusting the phase or amplitude of different frequency components, the temporal shape of the pulse can be modified through Fourier transform[90,133]. In this arrangement, the spatial dispersion $D_x=|dx/d\omega|=m\lambda^2f/2\pi cd\cos\theta_d$ and the radius of each frequency beam is given by $w_f=2f\cos\theta_i/kw_i\cos\theta_d$, where $w_i$ is the input Gaussian beam spatial radius. This is useful in applications requiring precise control over pulse duration and shape. Such pulse shaper architecture is well-established, with commercial products available on the market.

In the conventional 4f pulse shaping apparatus, a 1D amplitude or phase mask is used as the frequency plane filter, modulating only the 1D frequency components while leaving the spatial dimension untouched. The successful development of two-dimensional optical modulators, such as liquid crystal spatial light modulators (LC-SLMs), metasurfaces, and diffractive optical elements (DOEs), has enabled arbitrary control over ultrafast pulse shaping in a space–time coupled manner. The spectrum of an input pulse beam is spatially spread along the $y$-axis by a grating and collimates onto a spatial light modulator (SLM) through a cylindrical lens so that each wavelength $\lambda$ is assigned to a position $y(\lambda)$ forming a 2D spatial-spectral domain. The spatial spectrum of a pulsed beam is modulated by a phase mask [usually imparts an added phase by a phase-only reflective SLM[118], as shown in Fig. 2(b)]. Recombining the spectrum via the cylindrical lens and grating reconstitutes the pulse (complete a time-frequency Fourier transformation), and the STWP is realized after free-space diffraction of a distance. Generally speaking, the light field at the spectral-space plane inside the pulse shaper and the light field in the far field or any other planes beyond the pulse shaper are connected through a linear transformation. Under the paraxial approximation and narrow bandwidth condition $|\Omega|=|\omega-\omega_0|\ll\omega$, the spatial light field after the pulse shaper at a distance of $L$ can be described by the Fresnel diffraction integral

$$\Psi(x,y,L;\Omega)=\frac{-i}{\lambda L}\iint\Psi_0(\xi,\eta,\Omega)e^{i\frac{k_0}{2L}[(x-\xi)^2+(y-\eta)^2]}\mathrm{d}\xi\mathrm{d}\eta, \tag{10}$$

where $(x,y)$ and $(\xi,\eta)$ are the spatial coordinates at the output and SLM plane, respectively. The temporal envelope can be calculated by the time-frequency Fourier transformation:

$$\Psi(x,y,L;\tau)=\frac{1}{2\pi}\int\Psi(x,y,L;\Omega)e^{i\alpha\Omega^2}e^{-i\Omega\tau}\mathrm{d}\Omega, \tag{11}$$

where $\exp(i\alpha\Omega^2)$ is a group delay dispersion (GDD), which can be adjusted by the SLM. Thus, the spatiotemporal envelope of this STWP at location $L$ can be described by the combination of

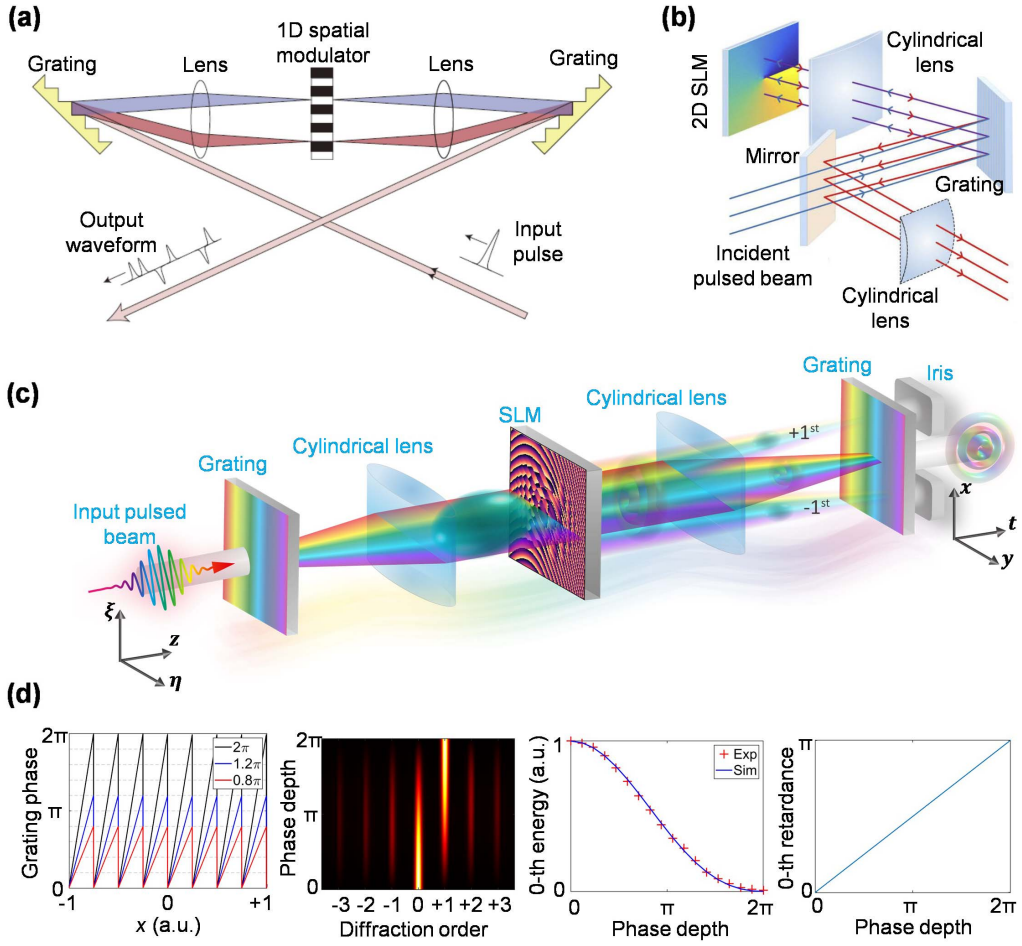


**Fig. 2** Schematic of 4*f* ultrafast pulse shaper. (a) 1D pulse shaper for temporal modulation[93]. (b) 2D pulse shaper for spatiotemporal phase-only modulation[118]. (c) 2D holographic pulse shaper for spatiotemporally sculpting STWPs via a complex-amplitude modulation[134]. (d) The intensity modulation and phase compensation analysis of a complex-amplitude modulated hologram[135].

Eqs. (10) and (11), which reads

$$\Psi(x,y,L;\tau) \propto \iiint \Psi_0(\xi,\eta,\Omega) e^{ik_0\frac{\xi^2+\eta^2}{2L}+i\alpha\Omega^2} e^{-ik_0\frac{x\xi+y\eta}{L}-i\Omega\tau} \mathrm{d}\xi\mathrm{d}\eta\mathrm{d}\Omega. \tag{12}$$

Equation (12) has an equivalent angular spectrum form in a dispersive medium as

$$\Psi(x,y,L;\tau) \propto \iiint \tilde{\Psi}_0(k_\xi,k_\eta,\Omega) e^{i\frac{k_\xi^2+k_\eta^2}{2k_0}L-i\frac{\beta_2}{2}\Omega^2 L} e^{-i(k_\xi x+k_\eta y)-i\Omega\tau} \mathrm{d}\Omega\mathrm{d}k_\xi\mathrm{d}k_\eta, \tag{13}$$

where $(\xi,\eta,\Omega)$ is the corresponding coordinate of $(x,t,\tau)$ in momentum space. $\tilde{\Psi}_0$ is a 2D transmission function on the frequency plane of a pulse shaper, typically phase modulation for STWP generation such as spatiotemporal optical vortices and space–time light sheets.

Beyond phase-only modulations, a 2D "holography" pulse shaper concept, analogous to spatial off-axis holography, has been established to enable complex-amplitude modulation, as shown in Fig. 2(c). This arrangement is similar to the aforementioned 2D pulse shaper but involves a specific hologram, which is given by[134–136]

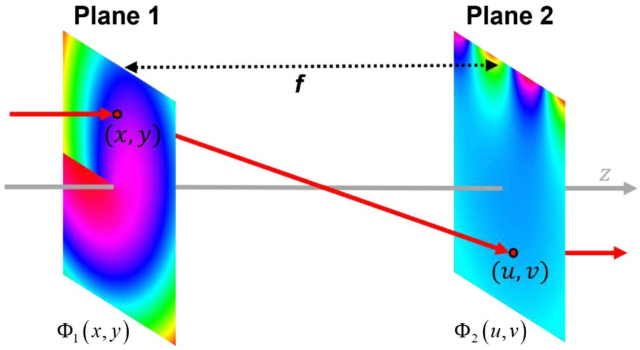


**Fig. 3** Schematic of an afocal optical system for conformal mapping.

$$\psi_{\mathrm{SLM}}(\Omega,\xi) = \mathrm{mod}[\mathrm{Arg}(\Psi_0) + \pi\cdot \mathrm{sinc}^{-1}(|\Psi_0|) + \mathrm{sinc}^{-1}(|\Psi_0|) \cdot \mathrm{mod}(2\pi g\xi, 2\pi) + \alpha\cdot\Omega^2, 2\pi], \tag{14}$$

where $g$ denotes the frequency of a linear phase ramp, the depth of which depends on the magnitude of the desired mode; $\mathrm{sinc}^{-1}(\cdot)$ stands for an inverse sine cardinal function. The encoding technique utilizes a one-dimensional blazed phase grating with different modulation depths in order to diffract light into the first order with different light intensities, as shown in Fig. 2(d). Additionally, to minimize residual modulation, the phase-only SLM must be calibrated to ensure a linear $2\pi$ phase response across all 256 gray levels at the operating wavelength. To generate high-quality STWPs, the spatial-spectral bandwidths of the pulsed beam should fully cover the hologram. In this scheme, the desired STWP with an arbitrary waveform is produced by filtering the zeroth-order diffraction light via a simple spatial filter. It should be noted that the spatial dimension of the light field can also be imaged onto the output plane using a 4f relay system, completely circumventing spatial diffraction. Recently, a spatiotemporal pulse shaping method, termed the dispersion magnifier, using conventional optical elements, has been proposed to generate STWPs in the nonparaxial regime[137].

### 2.3 Theory for Optical Conformal Mapping

Conformal mapping is a powerful tool in various fields of mathematics and engineering due to its angle-preserving properties, making it invaluable for transforming complex problems into simpler ones while retaining essential geometric features[138–148]. An afocal system for optical coordinate transformation between Cartesian $(x, y)$ and log-polar $(u, v)$ coordinates is a typical demonstration by utilizing phase-only computer-generated holograms, which usually involves a 1D line segment to 2D circle mapping operation. Figure 3 shows an afocal system consisting of two-phase elements separated by a distance of $f$. The phase profiles of the phase elements are denoted by $\Phi_1(x, y)$ and $\Phi_2(u, v)$. A collimated beam is mapped from plane 1 to plane 2 by the first phase element and collimated from plane 2 by the second phase element. Consider a plane wave $E(x, y)$ normally incident on the first plane 1; the electric field in plane 2 can be calculated by

$$E(u,v) = e^{ik(u^2+v^2)/2f}\iint E(x,y)e^{i\Phi_1(x,y)+ik(x^2+y^2)/2f}e^{-ik(ux+vy)/f}\mathrm{d}x\mathrm{d}y. \tag{15}$$

The deflection angle of the transmitted field right after plane 1 is given by[139]

$$\alpha = \frac{\partial\psi}{\partial x} = \frac{\partial\Phi_1(x,y)}{\partial x} - \frac{k}{f}(u-x), \tag{16}$$

and

$$\beta = \frac{\partial\psi}{\partial y} = \frac{\partial\Phi_1(x,y)}{\partial y} - \frac{k}{f}(v-y), \tag{17}$$

where $\psi(x,y) = \Phi_1(x,y) + k(x^2+y^2)/2f - k(ux+vy)/f$.

According to the stationary phase approximation, all contributions of Eq. (15) are vanished except about the saddle points of $\psi(x, y)$ at $(x_0, y_0)$, given by

$$\left.\frac{\partial\psi}{\partial x}\right|_{x_0} = 0, \qquad \left.\frac{\partial\psi}{\partial y}\right|_{y_0} = 0. \tag{18}$$

Combining Eqs. (16) and (17) with Eq. (18), we obtain a pair of partial differential equations as follows:

$$\frac{\partial\Phi_1(x,y)}{\partial x} = \frac{k}{f}(u-x), \tag{19}$$

and

$$\frac{\partial\Phi_1(x,y)}{\partial y} = \frac{k}{f}(v-y). \tag{20}$$

For the coordinate transformation of a Cartesian $(x, y)$ coordinate to a log-polar $(u, v)$ coordinate, the relation is given by

$$u = \theta_1 \quad \text{and} \quad v = \ln r_1, \tag{21}$$

where $\theta_1 = \tan^{-1}(y/x)$ and $r_1 = \sqrt{x^2+y^2}$. The reverse relation is

$$x = e^v\cos u \quad \text{and} \quad y = e^v \sin u, \tag{22}$$

Substituting Eq. (21) into Eqs. (19) and (20), it becomes

$$\frac{\partial\Phi_1(x,y)}{\partial x} = \frac{k}{f}\left[\tan^{-1}\left(\frac{y}{x}\right) - x\right], \tag{23}$$

$$\frac{\partial\Phi_1(x,y)}{\partial y} = \frac{k}{f}\left[\ln\sqrt{x^2+y^2} - y\right]. \tag{24}$$

Using the method of integration by parts, one can obtain

$$\Phi_1(x,y) = \frac{k}{f}\left[\frac{y}{2}\ln(x^2+y^2) + x\tan^{-1}\left(\frac{y}{x}\right) - y - \frac{1}{2}(x^2+y^2)\right]. \tag{25}$$

The second phase element is used to collimate the mapped beam. In the time-reversal direction, the second phase element is capable of performing a log-polar to Cartesian transformation from plane 2 to plane 1. Therefore, the gradient of $\Phi_2(u, v)$ and the mapping relation can be expressed as

$$\frac{\partial\Phi_2(u,v)}{\partial u} = \frac{k}{f}(x-u), \tag{26}$$

and

$$\frac{\partial\Phi_2(u,v)}{\partial v} = \frac{k}{f}(y-v). \tag{27}$$

Combined with Eq. (22), one can obtain the phase profile of the second phase element:

$$\Phi_2(u,v)=\frac{k}{f}\left[e^{v}\sin u-\frac{1}{2}(u^2+v^2)\right]. \tag{28}$$

Similarity, a log-polar to Cartesian inverse transformation requires the following coordinate relations:

$$u=e^{y}\cos\left[\tan^{-1}\frac{y}{x}\right]\quad\text{and}\quad v=e^{y}\sin\left[\tan^{-1}\frac{y}{x}\right]. \tag{29}$$

### 2.4 Multi-Plane Light Conversion

Multi-plane light conversion (MPLC) can be used to perform arbitrary spatial basis transformations using a cascade of phase planes separated by a unitary transformation, typically free-space propagation or a Fourier transform. An MPLC device consists of a series of phase masks separated by free-space propagation[149], as shown in Fig. 4(a). It can convert one orthogonal set of beams (including spatial positions) into another orthogonal set through unitary transformation. Different methods have been used to optimize the patterns of phase masks. Since the design of MPLC falls in the general category of inverse design, quite often, patterns of the optimized phase masks are not intuitive. Modified wavefront matching is the method commonly used to iteratively update phase masks. Wavefront matching propagates the input fields $[f_i(x,y,z)]$ forward through the $k$-th phase mask $[\Phi_k(x,y)]$ and the output fields $b_i(x,y,z)$ backward through the phase mask. The only way for an input to excite an output is if the phase fronts of the $N$ forward propagating inputs, $f_i$, and backward propagating outputs, $b_i$, match at every spatial coordinate. When the fields do not match, the phase error at each spatial coordinate can be computed and subtracted from that phase plane. In a multi-plane system, the algorithm moves all $f_i$ and $b_i$ forward together to the next plane or backward together to the previous plane and iterates until the error is minimized. To find the phase distribution $\Phi_k(x,y)$ for a given phase masks, the algorithm iteratively computes a corrective phase distribution given by[150]

$$\Delta\Phi_k(x,y)=-\mathrm{Arg}\left[\sum_i o_{kii}(x,y)e^{-i\phi_i}\right], \tag{30}$$

where $\phi_i$ is the average phase of $o_{kii}$. The field overlap matrix at the $k$-th plane $o_{kij}$ is given by

$$o_{kij}(x,y)=f_i(x,y,z)b_j^{*}(x,y,z)e^{i\Phi_k(x,y)}. \tag{31}$$

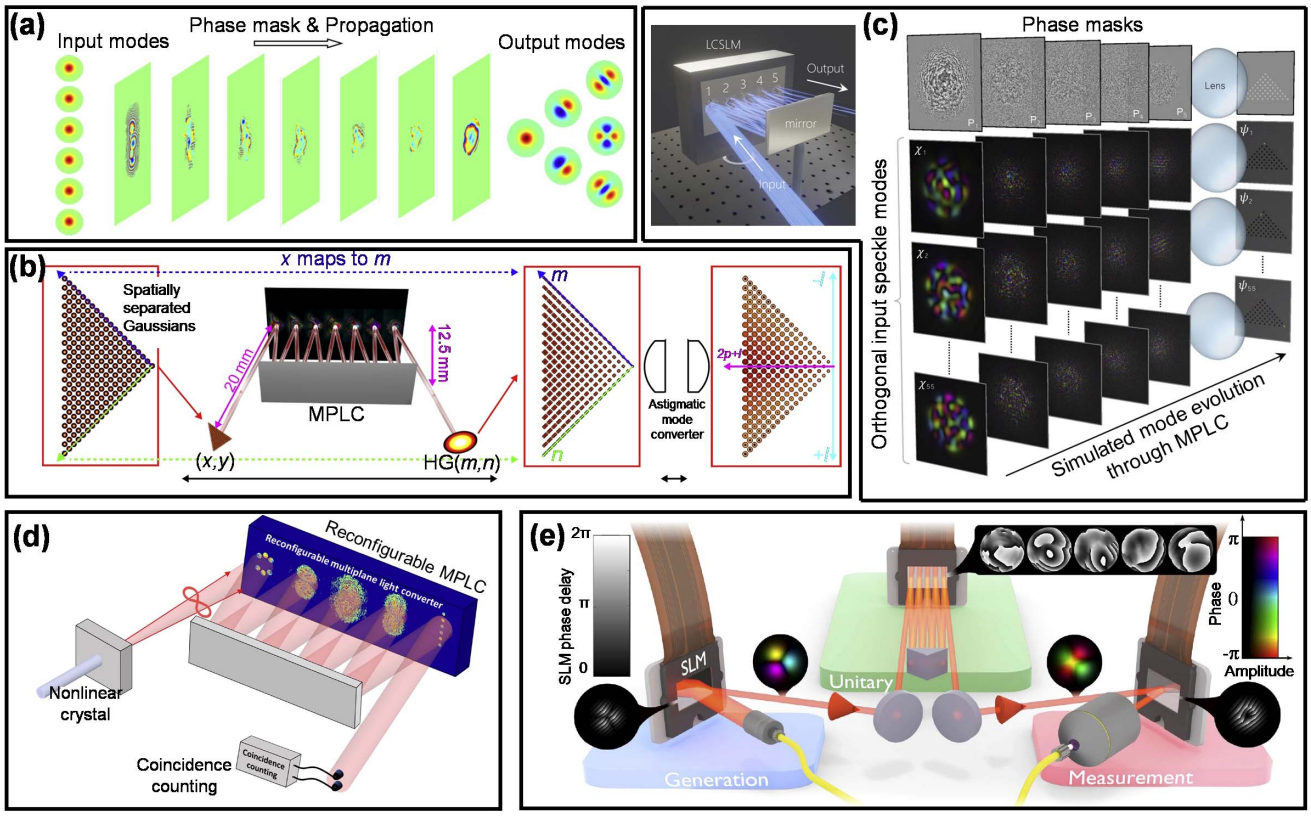


**Fig. 4** Multi-plane light conversion (MPLC) for spatially controlling light fields. (a) Schematic for MPLC[149]. (b) Laguerre/Hermite–Gaussian mode sorter based on MPLC[151]. (c) A high-dimensional MPLC-based mode sorter for arbitrarily randomized spatial mode basis sorting[152]. (d) Processing entangled photons in high dimensions with an MPLC[153]. A pixel-entangled two-photon state undergoes a general unitary transformation implemented using an MPLC. (e) Sensing quantum-state-based rotations with an MPLC[154].

The $i \times j$ dimensional coupling matrix $\boldsymbol{O}_k$ with entries

$$O_{kij} = \iint o_{kij}(x, y)\mathrm{d}x\mathrm{d}y \tag{32}$$

quantifies how well each input mode couples to each output mode. The phase distribution of the $k$-th element in the $n$-th iteration is calculated as follows:

$$\Phi_k^n = \sum_i f_i^n b_i^{n*} e^{-i\mathrm{Arg}[O_{kij}^n]}, \tag{33}$$

where $O_{kij}^n = \iint o_{kij}^n(x, y)\mathrm{d}x\mathrm{d}y$ and $o_{kij}^n(x,y) = f_i^n b_i^{n*} e^{i\mathrm{Arg}[\Phi_k^{n-1}]}$. The marker $n$ denotes the $n$-th iteration. As such, the $k$-th phase mask $\Phi_k$ can be calculated through a sufficient number of iterations $\Phi_k^n$ as described above. For a few specific modal bases, elegant MPLC designs have been found that are capable of efficiently sorting many spatial modes using a small number of planes. In 2019, Fontaine *et al.* realized a Laguerre–Gaussian mode sorter capable of decomposing a beam into a Cartesian grid of identical Gaussian spots each containing a single Laguerre–Gaussian component[151]. The input Gaussian array, represented as spatially orthogonal modes, undergoes an MPLC transform, which converts the Cartesian coordinates $(x, y)$ to the Cartesian indices $(m, n)$ corresponding to Hermite-Gaussian modes. Then the HG basis can easily be converted to LG modes through two cylindrical lenses. Besides, Kupianskyi *et al.* investigated high-mode-capacity MPLCs to create arbitrary spatial mode sorters and linear optical circuits, focusing on designs with a low number of phase planes for experimental feasibility[152], as shown in Fig. 4(c). They develop a new inverse-design algorithm based on gradient ascent, which achieves lower modal cross-talk and higher fidelity in the low-plane limit, and demonstrate prototype sorters capable of operating on up to 55 modes, sorting photons by various spatial mode bases. MPLCs have potential applications in both the classical and quantum optics domains, in fields ranging from optical communications to optical computing and imaging. For example, Lib *et al.* demonstrated the use of MPLC as a versatile and scalable platform for high-dimensional quantum information processing with entangled photons[153], as shown in Fig. 4(d). They perform four key tasks—high-dimensional entanglement certification, tailored two-photon interference, arbitrary random transformations, and spatial mode conversions for entanglement distribution—by simply changing the reconfigurable phase patterns of the MPLC without any hardware changes, showcasing its universality and applicability in quantum information processing. Eriksson *et al.* experimentally proposed a scheme to estimate the three parameters of a general rotation using quantum states that achieve the ultimate precision set by the quantum Cramér-Rao bound[154]. The states are realized through the orbital angular momentum of light and rotations are implemented with an MPLC setup, indicating potential for advanced rotation sensors, as shown in Fig. 4(e). The incorporation of an ultrafast pulse shaper with MPLC devices will also enable a certain level of reconfigurability in both space and time.

### *2.5 Metasurfaces and Nanophotonic Platform*

Conventional generation of structured light typically relies on multiple cascaded phases and wave plates in bulky form, imposing major challenges for their practical applications. Over the past decade, flat optics, also known as ultrathin metasurfaces, have become a new topic in the photonics community. Recently, such metasurfaces have been largely developed for the generation, manipulation, and detection of structured light[155–157]. In meta-optics, both plasmonic antennas and dielectric pillars have been used for the metasurface generation of different structured light fields in real space. Figure 5(a) shows dynamic phase metasurfaces with phase-only modulation with the use of a set of meta-atoms for helical phase imprinting[158–161]. Besides utilizing phase-only elements to generate phase vortices, plasmonic and dielectric nanostructures can be engineered to exhibit significant polarization birefringence, resulting in distinct phase accumulations along their long and short axes. Geometric metasurfaces, following the Pancharatnam-Berry phase principle, enable the creation of polarization-encoded phase vortices by rotating identical asymmetric nanostructures in-plane[162–164], as shown in Fig. 5(b). Furthermore, meta-atoms featuring varying orientations and sizes have been advanced to independently manipulate arbitrary orthogonal polarizations. Figure 5(c) exhibits the J-plate metasurfaces by exploiting the complete and independent phase and polarization control by single meta-atoms based on the Jones calculus[165,166].

Designing and optimizing a novel metasurface to fully and independently manipulate both the amplitude and phase of transmitted light is crucial for customizing structured light. Ren *et al.* proposed a geometric metasurface with complex-amplitude modulation using polymer-based rectangular nanopillars (refractive index $n = 1.52$) with an aspect ratio up to 15 as meta-atoms[167]. Such high-aspect-ratio nanopillars exhibit strong birefringence, altering the polarization states of transmitted light and forming the basis for a geometric phase response controlled by the in-plane rotation angle ($\theta$), depicted in Fig. 5(d). Numerical simulations, under periodic boundary conditions, analyzed the amplitude and initial phase retardation of cross-polarization in light beams transmitted through these nanopillars as functions of nanopillar height ($H$) and length ($L$), as illustrated in Fig. 5(e). By adjusting the out-of-plane height ($H$) and in-plane rotation angle ($\theta$) of these 3D meta-atoms, independent modulation of both amplitude and phase can be achieved, offering versatile control over structured light. As shown in Fig. 5(f), a dielectric metasurface is used in the 4f pulse shaper configuration to manipulate, simultaneously and independently, the amplitude and phase of the constituent frequency components of the pulse[168]. With modern nanofabrication capabilities, nanophotonic devices used as SLMs offer the advantage of higher spatiotemporal resolution due to their smaller pixel size. Additionally, these devices enable multidimensional modulation, including phase, polarization, and amplitude, within a single device, providing a significant advantage over traditional phase-only SLM- or amplitude-only digital micromirror device (DMD)-based pulse shaper configurations.

## 3 Generation and Manipulation of STWPs

The emergence of novel STWP synthesizers and advancements such as the 2D pulse shaper and STOVs have sparked a surge in research activity in this field. Recent innovations, including space–time light sheets, toroidal pulses, and hopfions, signal that this area is on the brink of significant breakthroughs. This section summarizes some of the latest developments in spatiotemporal light sculpting reported over the past few years.

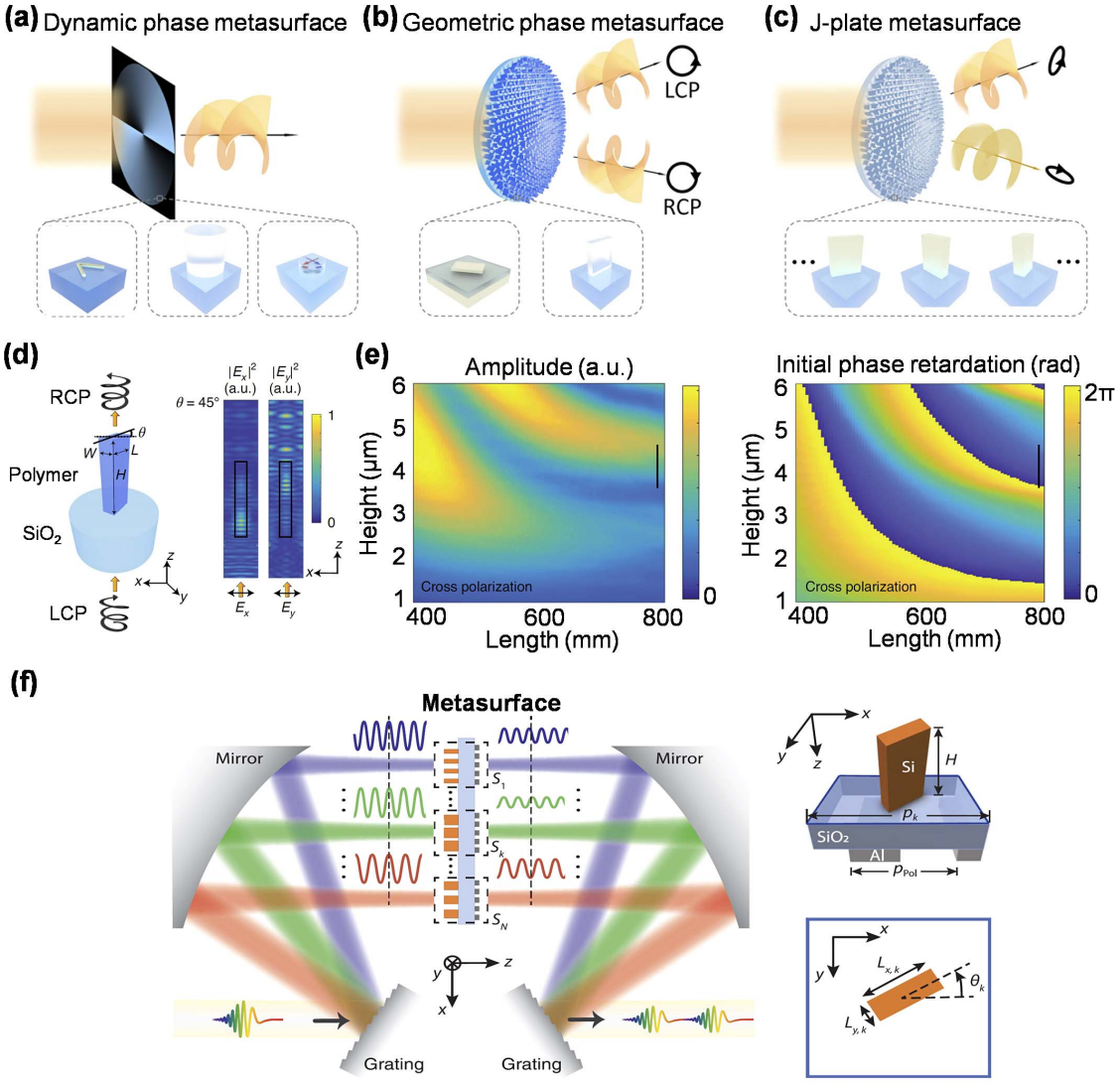


**Fig. 5** Illustration of some typical metasurfaces for the structured-light field generation. (a) Dynamic phase directly imprints a helical phase profile via phase-sensitive elements[156]. (b) Geometric phase metasurfaces encode the helical phase profile onto the cross-polarization component from the metasurface using birefringence[156]. (c) J-plate metasurfaces exploit the complete and independent phase and polarization control, capable of creating different OAM modes at arbitrary orthogonal polarization outputs[156]. (d) Design and optimization of a 3D metasurface for the complete and independent manipulation of both amplitude and phase responses of transmitted light[167]. (e) Numerical characterization of the amplitude and initial phase retardation of cross-polarization transmitted from a nanopillar with different heights ($H$) and lengths ($L$)[167]. (f) Ultrafast optical pulse shaping using dielectric metasurfaces[168]. In a 4$f$ configuration, a metasurface device is used to perform the 2D complex-amplitude modulation at the frequency plane.

### *3.1 Spatiotemporal Vortices with Transverse OAM*

Light fields with twisted wavefronts of the form $\exp(-il\theta)$, known as optical vortices, exhibit a symmetric hollow intensity profile due to on-axis phase singularities. The integer $l$ is an azimuthal quantum number referred to as the topological charge. In 1992, Allen *et al.* discovered that spatial optical vortices possess a longitudinal OAM proportional to the topological charge $l$[42]. This OAM is parallel to the wavevector and the propagation direction of the beam[63]. Until very recently, optical vortices carrying intrinsic transverse OAM perpendicular to the wavevector (see Refs. [118,134]) had remained elusive. STOV is a typical space–time coupled wavepacket, which has a screw phase dislocation and a zero-intensity center raised by the phase singularities on the space–time plane. The spatiotemporal vortices were first proposed in Ref. [169]. Such wavepackets carry transverse orbital angular momentum perpendicular to the wavevector and the propagation direction of the beam[170,171]. The first experimental observation of STOVs occurred during

filamentation processes in air but the desired STOVs only accounted for a very small fraction of the total energy[172].

Recently, the STOV wavepacket has been successfully generated in the linear regime with the help of a 2D pulse shaper[118], as shown in Fig. 6(a). Since the OAM is a conserved physical property, such singularities in the frequency domain are then transformed into singularities in the space–time domain, creating an STOV wavepacket with controllable transverse OAMs. To vividly visualize such wavepackets, a Mach-Zehnder-like scanning interferometer is utilized to measure their 3D spatiotemporal complex amplitude information. A Fourier-transform-limited ultrashort reference pulse spatially interferes with the target wavepacket at a small angle, varying the time delays to create a series of time-dependent fringe patterns, like the off-axis holography, as shown in Fig. 6(b). The contrast and relative displacement of the interference fringes contain the intensity and phase information of each time slice, respectively. Figure 6(c) exhibits the reconstructed 3D STOV wavepackets by stitching all temporal slices, demonstrating a phase singularity and null-intensity center in the space–time domain. Figure 6(d) shows the process of STOV formation in free space after the pulse shaper[117]. A space–time symmetry donut is formed only at a specific location where the spatial diffraction and temporal dispersion are matched.

Since the STOV wavepacket is defined on the space–time plane in a coupled manner, it experiences dispersion and diffraction effects during propagation in free space or a dispersive medium. If the accumulated dispersion phase during propagation does not match the diffraction phase, the wavepacket gradually loses the integrity for its spatiotemporal field and splits into multiple separated lobes. Furthermore, even if an STOV wavepacket maintains a balanced dispersion and diffraction

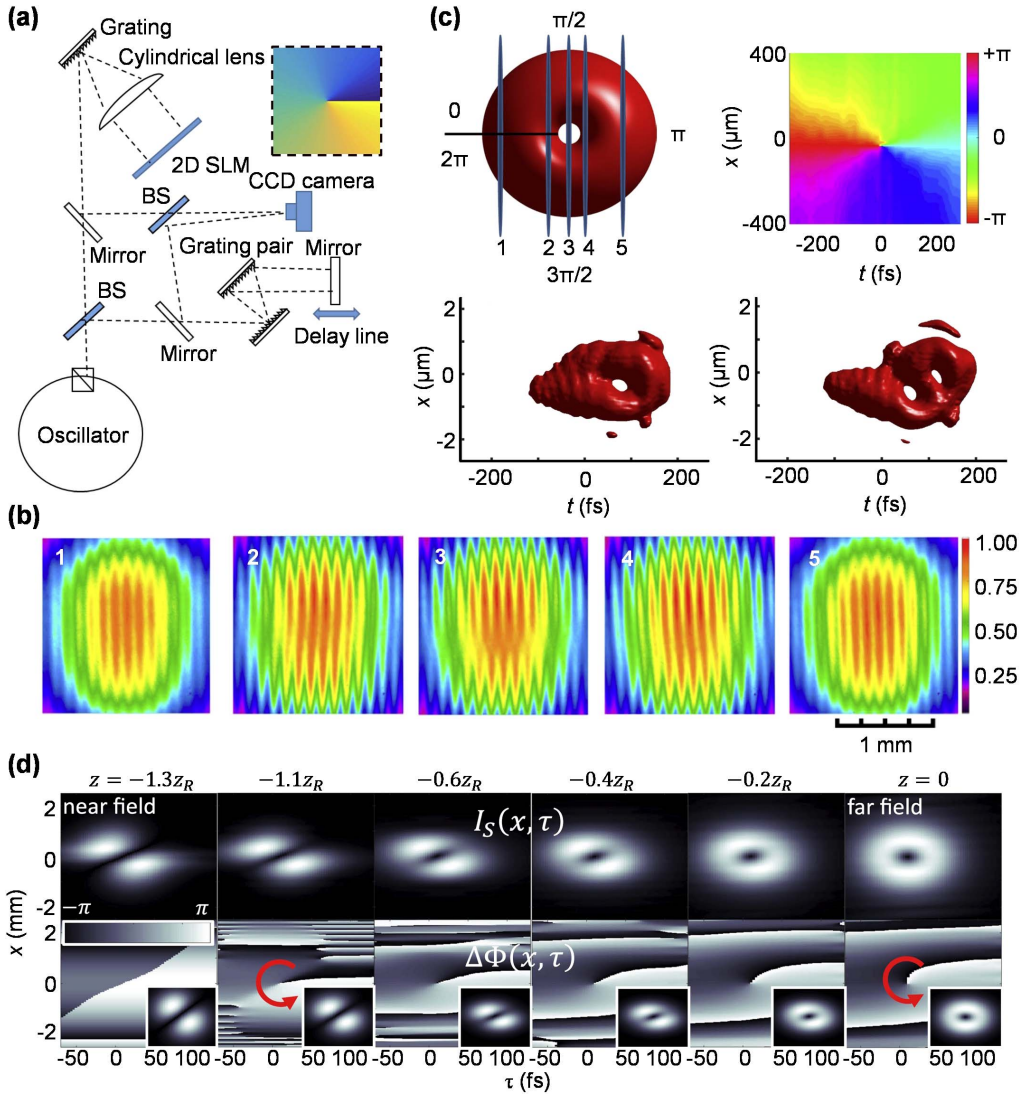


**Fig. 6** Experimental generation and characterization of STOV wavepackets. (a) A 2D pulse shaper with a helicoidal phase is used for STOV generation, and a Mach-Zehnder-like scanning interferometer is utilized for STOV measurement[118]. (b) Time-dependent interference fringes measured at different time delays[118], as indicated in (c). (c) Theoretical and reconstructed 3D iso-surface and phase of an STOV[118] based on (b). (d) Forming process of an STOV wavepacket in free space after a pulse shaper[117].

to preserve its donut-shaped spatiotemporal field distribution, it still spreads in both space and time due to these effects. Spatial Bessel-type optical vortices featured by infinite concentric rings carry infinite energy and exhibit a diffraction-free property during propagation. A Bessel beam can be simply generated in space via the Fourier transform of a conical phase or Dirac-ring. Cao. *et al.* first generated Bessel-type STOVs (BeSTOVs) by adding a conical phase into a helical phase inside the pulse shaper[173]. Figure 7(a) shows the corresponding phase for the BeSTOV wavepacket generation, in which the GDD phase and focus or defocus phase is used to manage dispersion and diffraction phase in a "virtual" dispersive medium. An experimentally generated BeSTOV wavepacket is exhibited in Fig. 7(b), showing a multi-ring structure. Figure 7(c) shows that such BeSTOV holds a non-spreading nature and is prevented from breaking up into multiple elemental vortices during propagation.

Most of the aforementioned STOVs are generated at a specific plane (far field) after the pulse shaper, as free-space propagation is required to implement the spatial Fourier transform. This method is challenging for generating STOVs with large topological charges due to the significant mode degradation of high-order modes during transmission. To circumvent this issue, Chen *et al.* proposed an inverse design using a helical phase multiplied by a Dirac-ring to generate diffraction-free

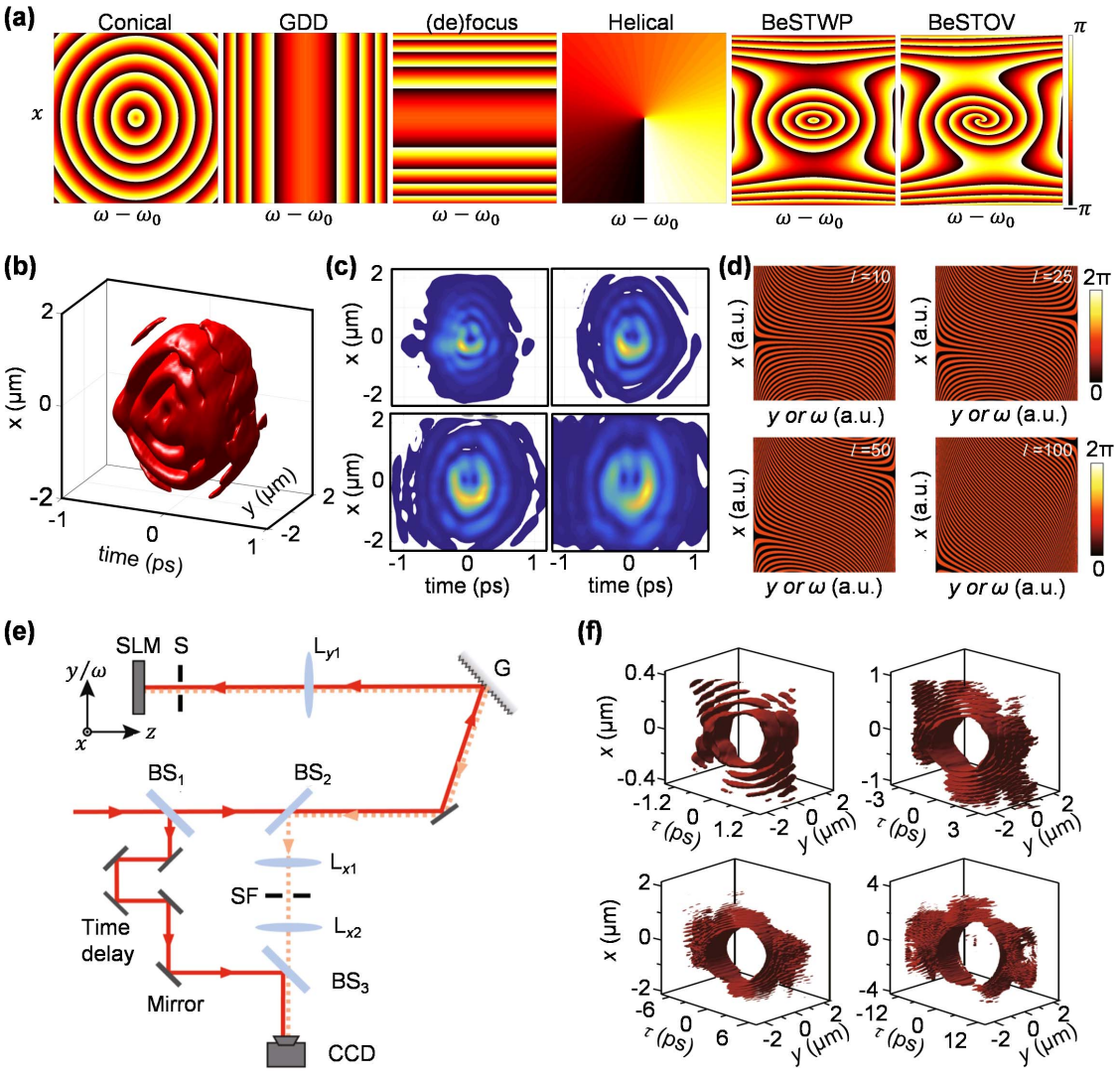


**Fig. 7** Generation of Bessel STOV (BeSTOV) wavepackets. (a) Phase-only hologram for generating BeSTOV wavepackets. Top row, from left to right: conical phase, second-order phase (GDD phase), focus/defocus phase, and helical phase. Bottom row: total phase of the above phases without topological charge (left) and with topological charge 2 (right)[173]. (b) Experimentally reconstructed 3D iso-surface of a BeSTOV wavepacket with topological charge 1[173]. (c) Spatiotemporal non-diffraction property of the generated BeSTOV wavepackets with topological charge 2[173]. (d) Generation of BeSTOV wavepackets carrying extremely high topological charges[174]. SLM phase patterns for generating BeSTOVs with topological charges of 10, 25, 50, and 100. (e) Experimental setup for generating and measuring BeSTOV wavepackets[174]. (f) Experimentally reconstructed ultrahigh-order BeSTOVs[174] from holograms in (d).

BeSTOVs with ultrahigh-order topological charges exceeding 100[174]. Figure 7(d) shows the phase patterns, where the 1D spatial Fourier transform from $k_x$ to $x$ is pre-calculated, allowing these phases to be located on the $x-\omega$ plane instead of the $k_x-\omega$ plane, thus eliminating the need for spatial Fourier transform. Figure 7(e) illustrates the experimental setup for the generation and characterization of high-order BeSTOVs. In this setup, the target BeSTOV wavepacket is generated immediately behind the grating and then imaged onto the camera using a 4*f*-imaging system ($L_{x1}$ and $L_{x2}$). Figure 7(f) displays the generated BeSTOVs with high-order topological charges of 10, 25, 50, and 100. These STOV wavepackets exhibit an asymmetric profile in space due to the absence of energy redistributions caused by the space–time coupling effects.

Beyond the phase-only modulation, a complex-amplitude modulation technique has recently been developed, significantly broadening the range of sophisticated STWPs with specially designed structures tailored to specific applications[135], as shown in Fig. 8(a). Figure 8(b) illustrates the generation of a fundamental Bessel wavepacket using only a ring mask. This holographic technique allows for the realization of spatiotemporal optical lattices by selecting appropriate pinhole masks in the spatial-spectral domain. Figure 8(c) demonstrates several configurations for generating ST crystal-like and quasi-crystal-like structures experimentally. Additionally, Fig. 8(d) presents the 3D intensity map and projection views of the reconstructed spatiotemporal flat-top pulses. This innovative spatiotemporal hologram technique, which controls both the amplitude and phase of optical spatiotemporal wavepackets, leads to enhanced space–time coupling and more flexible manipulation of light fields.

Recent years have witnessed a breakthrough in the realm of STOVs. However, the predominant emphasis in current initiatives has been on STOV wavepackets rooted in Gaussian-type (described by a Hankel transform) and Bessel-type (described by a Bessel function) with one controllable degree of freedom of azimuthal quantum numbers in the space–time domain. Laguerre–Gaussian and Hermite–Gaussian modes offer dual controllable degrees of freedom in cylindrical and Cartesian coordinate systems, respectively. Both modes define complete and orthonormal bases for the spatial structure of light, providing an infinite set of functions to describe the light field's spatial properties. Liu *et al.* first demonstrate the synthesis of STOVs with controllable radial and azimuthal quantum numbers, referred to as spatiotemporal Laguerre–Gaussian (STLG) wavepackets, by imprinting 2D complex modulation onto the spectrum of ultrashort laser pulses, opening new possibilities for spatiotemporally sculpturing of light[134]. The STLG wavepacket is given by

$$\Psi_{\mathrm{STLG}}=\left(\frac{\sqrt{2}\rho}{w_2}\right)^{|l|}\exp\left(-\frac{\rho^2}{w_2^2}\right)L_p^{|l|}\left(\frac{2\rho^2}{w_2^2}\right)\exp(-il\theta), \tag{34}$$

where $\rho=\sqrt{\tau^2+x^2}$ and $\theta=\tan^{-1}(x/\tau)$. $L_p^{|l|}(\cdot)$ denotes associated Laguerre polynomials of the orders $p$ and $l$. Figure 9(a) shows the experimental setup for STLG wavepacket generation and characterization. This nested spatiotemporal topology within the wavepacket's profile can be precisely measured by temporal slice interference, as illustrated in Fig. 9(b). Figure 9(c) presents the 3D reconstructed iso-surface and retrieved phase of an STLG wavepacket, highlighting its intrinsic transverse orbital angular momentum (OAM) and cylindrical phase dislocations within the spatiotemporal profile. By properly adjusting dispersion and diffraction, STLG wavepackets with large mode indices can also be successfully generated, as shown in Fig. 9(d). In addition, the spatiotemporal Hermite–Gaussian wavepacket with various orders is given by[134]

$$\Psi_{\mathrm{STHG}}=H_m\left(\frac{\tau}{w_2}\right)H_n\left(\frac{x}{w_2}\right)\exp\left(-\frac{\tau^2+x^2}{2w_2^2}\right), \tag{35}$$

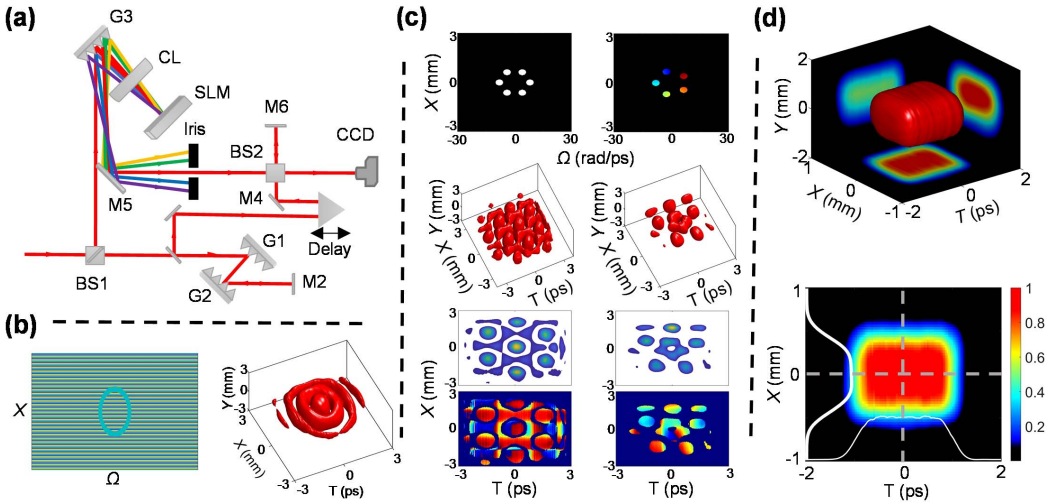


**Fig. 8** Complicated STWP generation based on complex-amplitude modulation[135]. (a) Realization of spatiotemporal complex amplitude modulation with redistribution of energy into other diffraction orders. (b) Demonstration of spatiotemporal complex modulation with the generation of a spatiotemporal Bessel wavepacket via complex-amplitude modulation. (c) Experimental results of spatiotemporal optical time crystals and spatiotemporal optical time quasi-crystals via complex-amplitude modulation; top row: SLM phase patterns. (d) 3D iso-surface of the generated spatiotemporal flat-top wavepacket via complex-amplitude modulation.

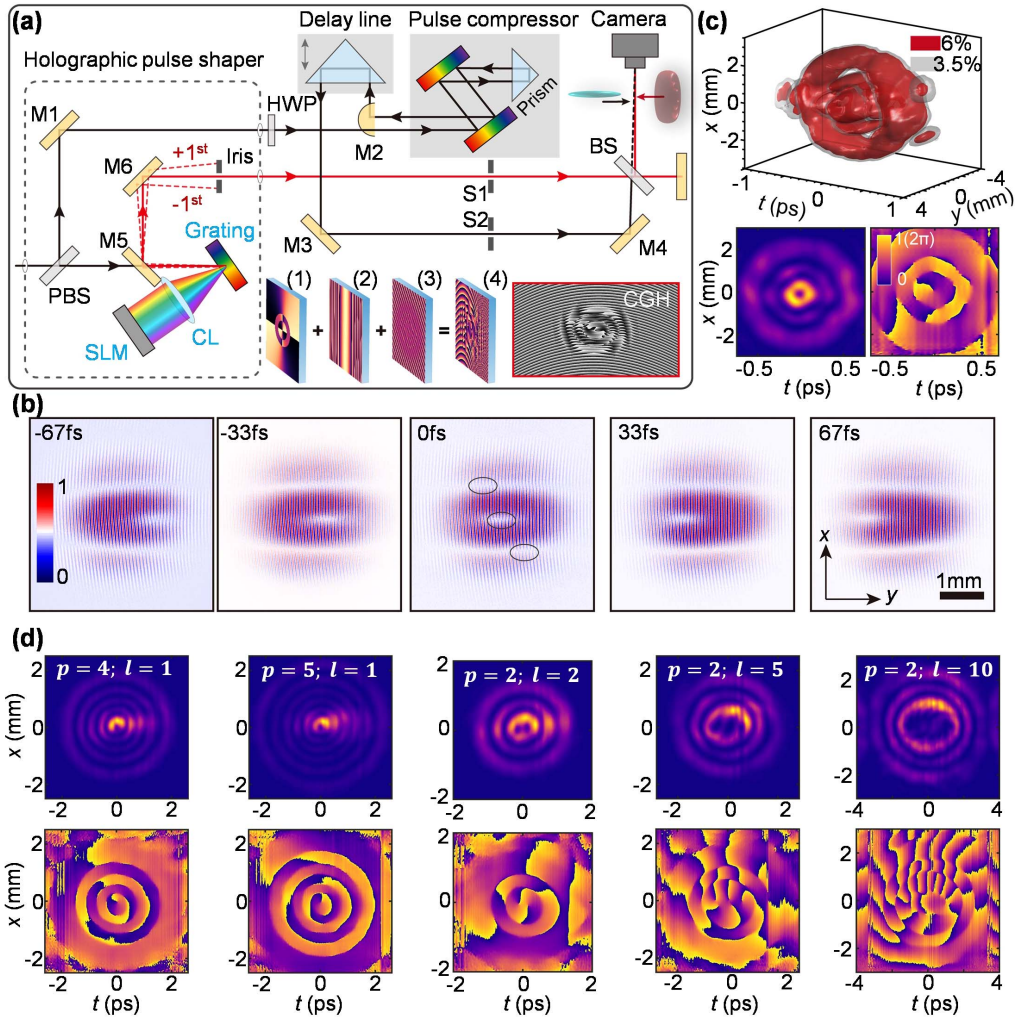


**Fig. 9** Synthesis and characterization of STOV wavepackets with controllable radial and azimuthal quantum numbers[134]. (a) Optical setup for synthesizing and characterizing STLG wavepackets. The apparatus comprises three sections: (i) 2D ultrafast holographic pulse shaper consisting of a diffraction grating, a cylindrical lens, and an SLM; (ii) a pulse compressor system consisting of a parallel grating pair; (iii) a time delay line system for fully reconstructing 3D profile of generated ST wavepacket. (b) Time-dependent interference fringes of STLG wavepacket of $p = 2, l = 1$ at several time delays. (c) Experimentally reconstructed 3D iso-surface, intensity, and phase of an STLG wavepacket with $p = 2, l = 1$. (d) Generation of STLG wavepackets with high-order radial and azimuthal quantum numbers of $p = 4, l = 1$; $p = 5, l = 1$; $p = 2, l = 2$; $p = 2, l = 5$; and $p = 2, l = 10$.

where $H_m(\cdot)$ denotes Hermite polynomials of the order $m$. Mode conversion between an STLG wavepacket and an STHG wavepacket can be achieved by applying controlled spatiotemporal astigmatism. Both STLG and STHG sets as the laser modes of space–time form complete bases in the space–time domain, laying a crucial foundation for future advancements in spatiotemporally structured light engineering. Recently, Ponomarenke *et al.* theoretically introduced the concept of perfect STOV (PSTOV) wavepackets through the spatiotemporal Fourier transform of Bessel–Gauss STOVs[175]. These PSTOVs feature a bright ring with an invariant radius that remains independent of their transverse OAM.

Partially coherent beams have gained significant interest over the past decade due to their unique properties in beam propagation, robustness against turbulence, and self-healing capabilities. A key feature of partially coherent vortices is the transformation of their phase singularity into coherence singularity due to random phase fluctuations[176,177]. Similar to partially coherent vortices in the spatial domain, partially coherent spatiotemporal coupling wavepackets with transverse OAM have also been theoretically studied by Hyde, including spatiotemporal twisted wavepackets [Fig. 10(a)] and their propagation in dispersive media and atmospheric turbulence[178–180]. Mirando *et al.* expanded STOVs to temporal partial coherence STOVs by applying random phases to the spectrum of an amplified spontaneous emission source, as shown in Fig. 10(b)[181]. Due to the high spatial coherence and temporal incoherence of the ASE source, the shape of the STOV is severely distorted from the ring-shaped profile, with multiple singularities occurring at various temporal locations as phase randomness increases.

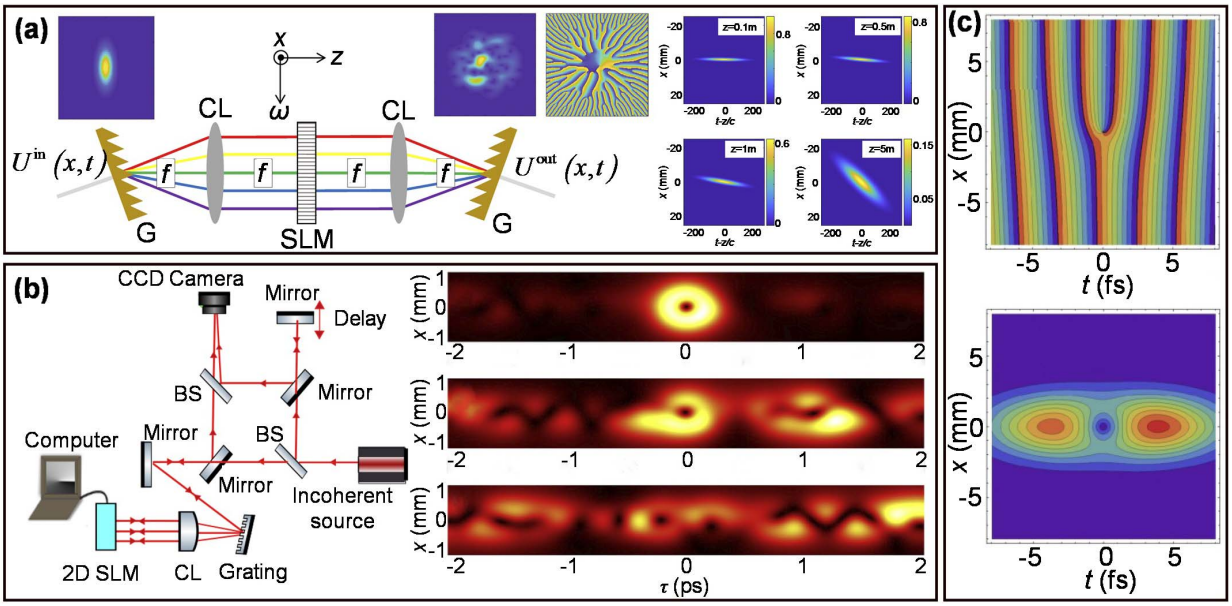


**Fig. 10** Partially coherent STOVs and spatiotemporal coherence vortices. (a) Schematic for spatiotemporal twisted wavepacket generation[178]. (b) Generation of STOVs with temporally partial coherence[181]. (c) Spatiotemporal coherence vortices[182,183].

Ding *et al.* have also proposed spatiotemporal coherence vortices through coherent-mode representation and Fourier transforms. Unlike partially coherent STOVs, which have phase singularity and null intensity, spatiotemporal coherence vortices exhibit singularities in their spatiotemporal degree of coherence, termed spatiotemporal coherence singularities, shown in Fig. 10(c)[182,183].

Despite the remarkable progress in generating STOV wavepackets using 2D ultrafast pulse shaping techniques, existing methods typically require bulky and sophisticated optical systems. Recently, nonlocal metasurfaces and nanophotonic structures much more compact than pulse shapers were proposed to create phase singularities in the spatiotemporal domain by breaking spatial mirror symmetry. Wang *et al.* theoretically generated a set of STOVs by engineering transmission functions in the momentum-frequency space based on the transmission modal lines model[184]. This transmission function can be achieved using a nanograting structure that is periodic in the $x$ direction and asymmetric in the $x$–$z$ plane, as shown on the left of Fig. 11(a). An incident pulse normally transmits this geometric structure, forming a nodal line surrounded by null-intensity and phase winding in the momentum-frequency domain, as marked on the right of Fig. 11(a), ultimately generating an STOV in the space–time domain. Figure 11(b) shows a spatiotemporal differentiator with a spatial mirror symmetric breaking structure designed to generate STOVs[185,186]. The Si-$SiO_2$ slanted grating was fabricated to excite STOV wavepackets. When a pulse passes normally through the nanograting, the wavefront of the incident pulse is partly sculptured by the dispersion relation of the optical resonance, resulting in a helical phase in the $k_x - \omega$ domain at a specific slant angle[187], as shown on the bottom of Figs. 11(c) and 11(d). The STOV wavepacket is eventually synthesized in the far field. Topological darkness, where intensity vanishes due to topological principles, is marked by optical phase singularities. Figure 11(e) shows that this phenomenon in a photonic crystal slab can be used for STOV generation[188]. In addition, a simple diffractive grating has been demonstrated to generate an STOV wavepacket by utilizing symmetry, resonance, and diffraction [Fig. 11(f)]. This process constructs a helical phase in frequency-momentum space, resulting in the formation of transverse OAM in both time and space[189]. However, traditional nanophotonic devices lack reconfigurability, hindering the dynamic switching and optimization of optical singularities. Ni *et al.* proposed tunable bilayer photonic crystals for spatiotemporal phase and polarization singularities generation and manipulation[190], as shown in Fig. 11(g). By adjusting the interlayer gap $h$ and misalignment vector $d$, these photonic crystals allow adjusting various optical singularities in momentum and frequency space and exciting STOVs in the spatiotemporal domain.

Understanding the physical properties of STOVs, including diffraction, propagation, reflection, and refraction, is significant not only for theoretical studies but also for the practical application of STOVs. As previously mentioned, an STOV wavepacket exhibits a symmetric and perfect helical phase when the diffraction phase and dispersion phase are balanced. If this balance is disrupted, the spatiotemporal distributions and structures change and eventually stabilize into a spatiotemporal profile that may differ significantly from the initial distributions. Generally, under paraxial and SVE approximations as described by Eqs. (6) and (7), the STOVs can be assumed to be stable within the Rayleigh range $z_R = \pi w_0^2/\lambda$ and dispersion length $z_D = \tau_0^2/|\beta_2|$. Figure 12(a) illustrates the optical setup for investigating the diffraction properties of STOV wavepackets using a grating[191]. In this setup, the final grating performs a temporal Fourier transform without a spatial Fourier transform. Due to this mismatch, the STOV degrades into a multiple-lobe structure along the diagonal caused by singularity splitting on the space-spectrum plane. The tilt direction and number of lobes are related to the sign and magnitude of the OAM, respectively. Only when diffraction and dispersion match can the STOV maintain a regular vortex morphology. The mismatch caused

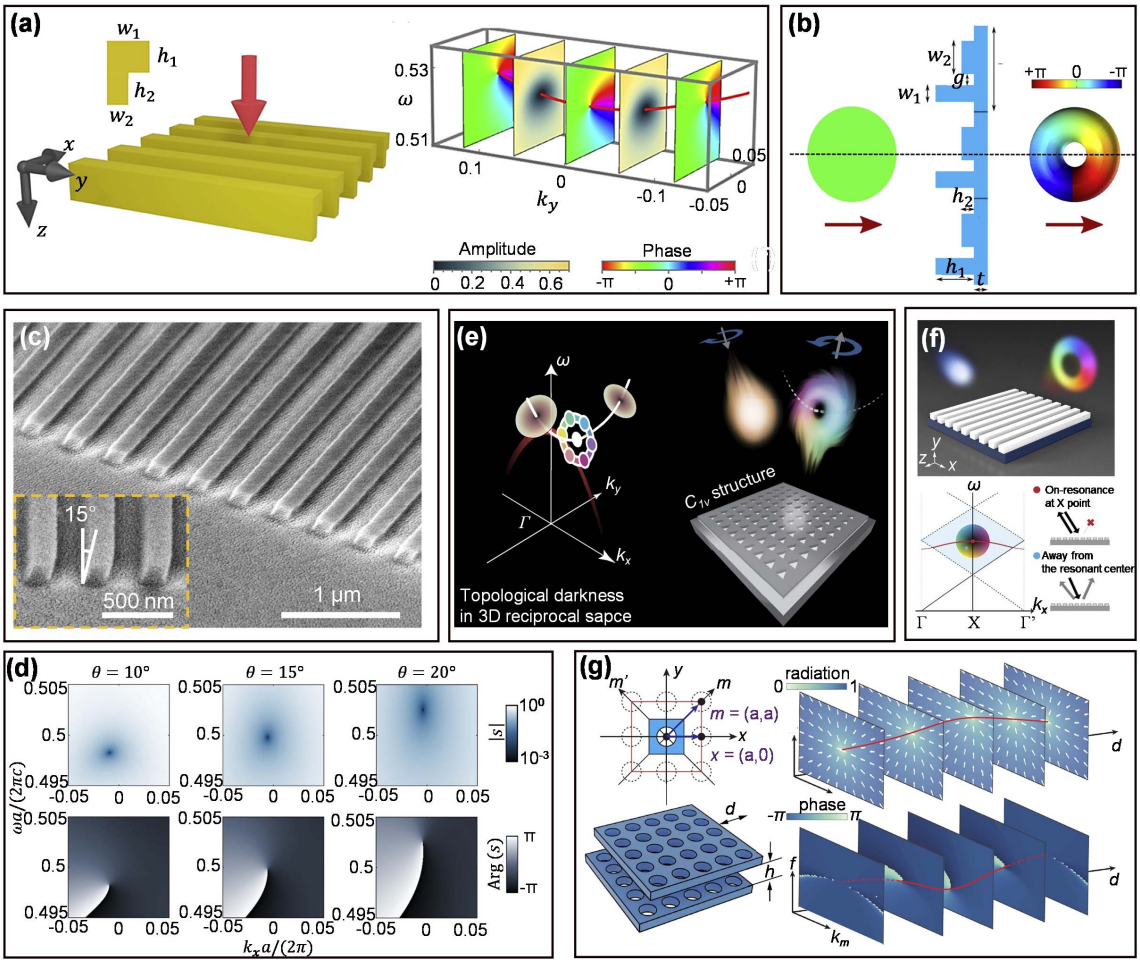


**Fig. 11** Metasurface and nanophotonic structure for STOV wavepacket generation. (a) Photonic crystal slab design for generating pulses with transverse OAM[184]. Left: the geometry of non-symmetric nanograting, with incident pulse indicated by the red arrow. The grating cross section in the $x$–$z$ plane is shown on the top left inset. Right: transmission function in the momentum space; the red line represents the transmission nodal line. (b) Spatiotemporal differentiator with spatial mirror symmetry breaking for STOV generation[185]. (c) STOV generation in a microscale platform composed of a slanted nanograting. A tilted-view and a side-view scanning electron microscope image of this slanted nanograting[187]. (d) The corresponding complex transmission coefficient distributions in the frequency-momentum space for slant angles of 10°, 15°, and 20°[187]. (e) Basic principle of STOV generation utilizing topological darkness of a photonic crystal slab[188]. A Gaussian pulse strikes a reflective photonic crystal slab with a periodic pattern on a dielectric membrane generating an STOV structure with a curved vortex line. (f) An STOV centered at a specific frequency can be generated from Gaussian pulses by a simple mirror-based resonant grating[189]. A phase singularity in specular reflection is formed at the X point in momentum space due to resonance-induced total retroreflection. (g) Concept of 3D optical singularities in bilayer photonic crystals[190].

by the lack of dispersion for free-space propagation makes the STOV wavepackets split[192], as shown in Fig. 12(b). Propagation dynamics of STOVs in the dispersive medium were theoretically studied by Porras and Hyde *et al.*[193], as shown in Fig. 12(c). Furthermore, Mazanov *et al.* recently investigated the OAM-dependent transverse and longitudinal pulse shifts of the reflection and refraction of an STOV at a planar isotropic interface [Fig. 12(d)][194]. The reflection/refraction of STOVs can be categorized into two cases: (A) when the OAM is orthogonal to the plane of incidence; and (B) when the OAM lies within this plane [Fig. 12(d)]. These cases reveal the spatial orbital-Hall-effect shift $\langle y \rangle$, the OAM-amplified angular Goos–Hänchen and Hall-effect shifts $\langle k_x \rangle$, $\langle k_y \rangle$, and the longitudinal shifts $\langle \zeta \rangle$. Recently, Tang *et al.* theoretically investigated the spatial and angular shifts of a 3D STOV with an arbitrarily oriented OAM at planar reflection and refraction. The spatial and angular shifts induced by the topological charge can be attributed to two topologically distinct tangent vector fields on the spheres[195]. Additionally, the dynamics of STOV pulses undergoing tight focusing and self-focusing propagation in nonlinear media

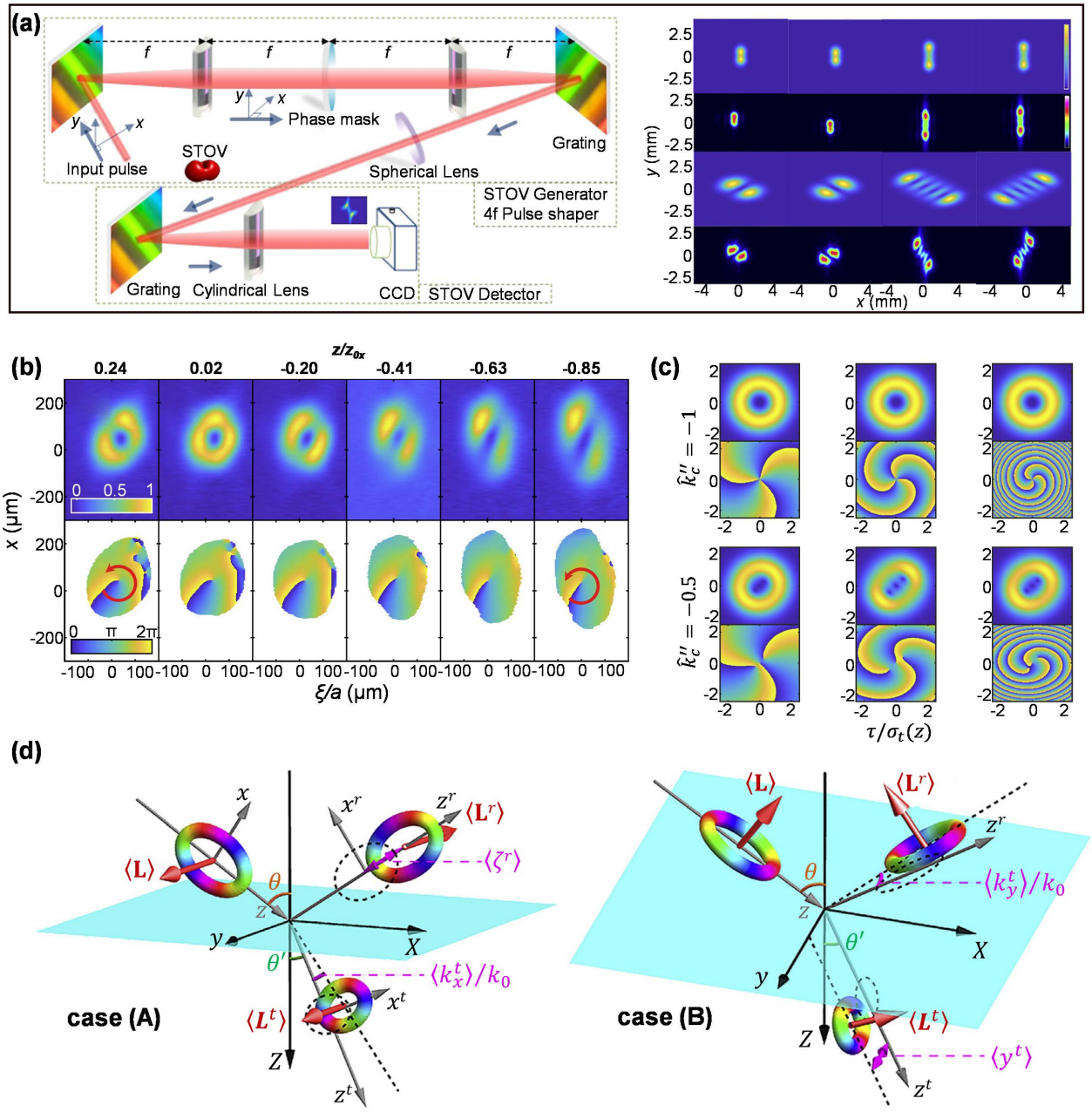


**Fig. 12** Diffraction and propagation properties of STOV wavepackets in free space and dispersive medium. (a) Left: experimental setup for investigating the diffraction property of STOV wavepackets by a grating. Right: diffraction pattern of STOVs with various topological charges[191]. (b) Experimental propagation dynamics of an STOV wavepacket in free space demonstrate that the absence of dispersion leads to wavepacket splitting[192]. (c) Calculated propagation dynamic of an STOV wavepacket in a dispersive medium with different dispersion coefficients[193]. When dispersion and diffraction are balanced, the wavepacket remains stable; otherwise, the singularity splits. (d) Schematics of the reflection and refraction of STOV at the planar isotropic interface[194]. STOVs carrying intrinsic transverse OAM exhibit peculiar properties of beam shifts and time delays depending on the value and orientation of the OAM.

and evolution in free space have been theoretically demonstrated, revealing complex spatiotemporal properties[196–200]. Recently, the propagation dynamics of an STOV pulse in the spatial fractional system were theoretically investigated in Ref. [201]. The study reveals that the propagation of a Bessel-type STOV in the fractional wave equation can be understood as the coherent superposition of two linearly shifted half-BSTVPs, which can exhibit orbital angular momentum backflow.

The STOV wavepacket has a helical phase on the space–time plane and carries intrinsic pure transverse OAM in the direction of propagation. A natural next step is to develop a wavepacket

that carries OAM in arbitrary directions, as the tilted angle of the OAM offers a new degree of freedom that could potentially be utilized in optical tweezing, spin-orbit angular momentum coupling, and quantum communications. Wan *et al.* studied, both analytically and experimentally, an STOV wavepacket with its phase singularity located in the $x$–$z$ plane intersecting with another phase singularity in the $x$–$y$ plane[202]. Such wavepacket has two perpendicularly crossed vortex lines resulting in a controllable magnitude and direction of OAM, as shown in Fig. 13(a). A theoretical proposal for a photonic crystal slab structure capable of generating STOV with arbitrary OAM direction has been introduced [see Fig. 13(b)]. This design achieves flexibility by strategically managing the structural symmetry of the device, thereby controlling the position and dispersion characteristics of the transmission nodal lines. This enables the creation of STOV oriented along any desired direction of the nodal line and OAM[203]. Subsequently, Zang *et al.* experimentally demonstrated tilted STOVs using astigmatic mode converters comprising a pair of counter-rotating cylindrical lenses [Fig. 13(c)]. By adjusting the rotation angle, these lenses introduce a longitudinal torque component to the initial transverse OAM, enabling STOVs with arbitrary OAM tilt[204]. Recently, Porras *et al.* theoretically proposed a method for controlling the vortex orientation of ultrashort optical pulses using spatial chirp, as shown in Fig. 13(d). This method allows tuning the purely longitudinal OAM of a pulsed vortex into a mixed state with both longitudinal and transverse components[205].

Combination and interaction of various types of optical singularity (spatiotemporal phase singularities, spatial phase singularities, polarization singularities, etc.) may lead to the

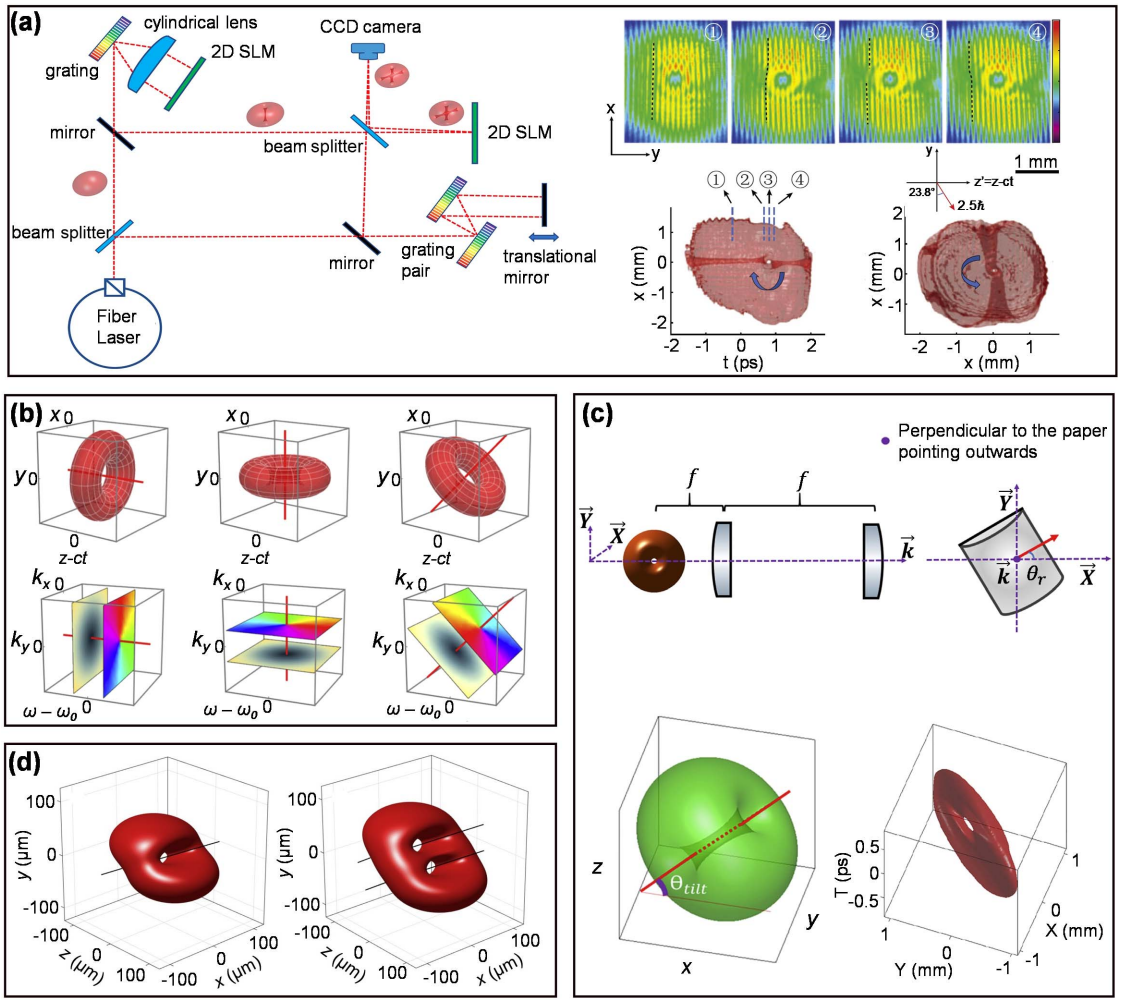


**Fig. 13** STOV wavepackets with tilted transverse OAM. (a) The intersection of spatiotemporal vortices and spatial vortices within a wavepacket leads to a tilted OAM due to the interaction of these two types of optical vortices[202]. (b) A photonic crystal slab structure can generate STOVs with arbitrary OAM direction based on the design of transmission nodal lines[203]. (c) Manipulating the transverse OAM direction can be achieved using a cylindrical lens system with a relative rotational angle. The additional longitudinal torque introduced by the cylindrical lenses couples with the original transverse OAM, adjusting its direction[204]. (d) The orientation of vortices in ultrashort optical pulses can be controlled using spatial chirp[205]. Introducing spatial chirp into a spatial vortex pulse results in an arbitrary orientation of the line phase singularity.

emergence of novel physical phenomena, such as intricate wavefront deformations, unique interference patterns, and complex energy transfer dynamics. By leveraging the chirping properties of ultrashort pulses, one can implement temporal manipulations of transverse OAM within an STOV wavepacket. It is well known that a chirped pulse exhibits a tilted wavefront in space–time, causing different spectral components within the pulse to reach the modulator at different times. This observation allows for the derivation and utilization of a linear mapping relationship between the spectral-space modulation on the SLM and the spatiotemporal distribution after the pulse shaper, facilitating spatiotemporal structuring. For example, applying an additional quadratic phase $\varphi(x,\omega) = \mathrm{GDD}\cdot(\omega-\omega_0)^2$ on the SLM can arbitrarily alter the pulse chirp. As illustrated on the left side of Fig. 14(a), a spatiotemporal optical vortex (STOV) with varying chirp levels presents different distributions in space–time[206]. By placing phase singularities separately on the $x-\omega$ plane, lattices of STOVs within the same wavepacket can be generated on the space-time plane [Fig. 14(a) middle]. These STOV lattices can be further manipulated by applying a linear phase $\varphi(\omega) = \alpha\cdot|\omega-\omega_0|$ to achieve spatiotemporal collisions of two STOVs in space-time, as shown on the right side of Fig. 14(a). The STOV wavepackets with phase singularities embedded in multiple space-time domains have also been theoretically studied in Ref. [207]. Both types of STOV wavepackets have the capability of tuning the magnitude and the orientation of the transverse OAM by changing the parameters $\theta$ and the domains of the phase singularities definition [Fig. 14(b)]. When STOVs are combined with simple spatial vortices in an optical wavepacket as perpendicular lines, vortex reconnections appear with propagation[208]. Figure 14(c) shows the experimental setup for realizing two perpendicular vortices and therefore vortex reconnections, in which just a cylindrical $\pi$-phase shift is loaded in a pulse shaper, and a 45° rotated cylindrical lens turns this into a spatiotemporally oriented loop reconnection at the focus. The experimental result clearly shows a loop structure with two vortex connections for connected vortices, as shown at the bottom of Fig. 14(c). Chen *et al.* experimentally created a new type of wavepacket with both spatiotemporal phase singularities and spatially polarized singularities by combining a 2D pulse shaper and a vectorial vortex plate[209], demonstrating that these two types of singularities can exist together, as shown in Fig. 14(d). Recently, they also theoretically studied a novel type of orbit-orbit coupling between the longitudinal and transverse OAMs carried by an STOV during the process of tight focusing[210].

The transverse OAM of the above-mentioned STOV wavepackets is temporally static, i.e., the OAM does not vary in time. Wan *et al.* first proposed the concept of time-varying transverse OAM and experimentally achieved the generation of STWPs with temporally separated phase singularities by imprinting a phase hologram[211] [Fig. 15(a)] on a chirped pulse via the 2D pulse shaper. Such STWP shows the temporally separated singularity with specific topological charges that demonstrates a time-varying transverse OAM, as shown in Fig. 15(a). Hancock *et al.* demonstrate that the transverse OAM of a light pulse can be changed only for transient phase perturbations well overlapped with the pulse in space-time, or by removing energy from a pulse already containing nonzero transverse OAM density[212]. As such, they successfully observed the subtle changes in the quantity of T-OAM over time by imparting a transient phase perturbation into an STOV pulse in the experiment, as shown in Fig. 15(b). Figure 15(c) shows the measured perturbed intensity and phase difference at various transient wire onset times $\tau_0$. The change in intrinsic transverse OAM per photon $\Delta\langle L_y\rangle = \langle L_y\rangle_{\mathrm{sp}} - \langle L_y\rangle_{\mathrm{s}}$, where $\langle L_y\rangle_{\mathrm{sp}}$ and $\langle L_y\rangle_{\mathrm{s}}$ denote the expectation values of transverse OAM for the pre- and post-perturbation optical fields, was calculated in Fig. 15(c) as a function of $\tau_0$. These results demonstrate the spatiotemporal torquing of light. Huang *et al.* recently demonstrated a wavepacket carrying numerous STOVs with a customizable topological charge arrangement[213]. These STWPs are generated in the far-field by a 2D pulse shaper, which imprints a multi-singularity phase pattern onto a non-chirped pulse beam, as shown in Fig. 15(d). Although the resultant STWP has an irregular intensity distribution and phase [Fig. 15(e)], it can still be identified from the corresponding temporal diffraction pattern by a grating, as shown in Fig. 15(f). The diffraction patterns of these strings exhibit more energetic lobes, with the number of dark bands between each lobe corresponding to the topological charge. This demonstrates the time-dependent transverse OAM within the same STWP.

Despite these notable advances in time-varying transverse OAM, practical applications remain challenging. The distorted STOV profiles not only degrade the purity of the time-varying OAM but also exacerbate cross-talk between singularities after transmission. As a result, generating a set of isolated spatiotemporal wavepackets with time-varying OAM remains an elusive goal. Inspired by the concept of optical frequency combs[96,98] and pulse bursts[99–101], recently, Liu *et al.* demonstrated an innovative approach by creating an ultrafast pulse comb of independent STLG modes with variable quantum numbers[214]. They achieved this by using a spatiotemporally multiplexed hologram to construct "spatiotemporal vortex bursts", as illustrated in Fig. 16. Unlike traditional spatial modes, each pulse in the burst is positioned on the space-time plane in a coupled manner. The radial and azimuthal quantum numbers of each pulse can be tailored on demand. The resulting spatiotemporal vortex bursts, akin to a series of flying toroids with ultrafast switchable quantum numbers, facilitate terahertz-rate conversion between high-purity mode indices[214].

Recently, the research on transverse OAM wavepackets has been extended to the nonlinear domain. In nonlinear frequency conversion, the conventional OAM of light with a topological charge $l_s$ follows a simple scaling rule, where the $N$th harmonic has a topological charge $N\ell_s$, reflecting OAM conservation. This rule has been validated for second-harmonic generation (SHG) and high-order harmonic generation (HHG). As depicted in Fig. 17(a), Gui *et al.* investigated SHG by cascading a nonlinear barium borate (BBO) crystal at the output of the STOV generator and confirmed the conversion of transverse OAM of STOV[215]. Figure 17(b) displays the experimentally measured fundamental STOV and its SHG after passing through a thin BBO crystal, illustrating the conservation of transverse OAM in the SHG process. Hancock *et al.* simultaneously reported similar experimental results[216] and provided a physical explanation for the principle of OAM conservation. The conservation of photon number implied by the Manley-Rowe relation[217] for SHG implies photons at the second harmonic averagely carry twice the OAM of photons at the fundamental. SHG is a quantum process involving light-matter interactions in the quantized electromagnetic field, and all photons in the STOV pulse from the pulse shaper have the same bandwidth, polarization, and spatiotemporal phase; energy and angular momentum are

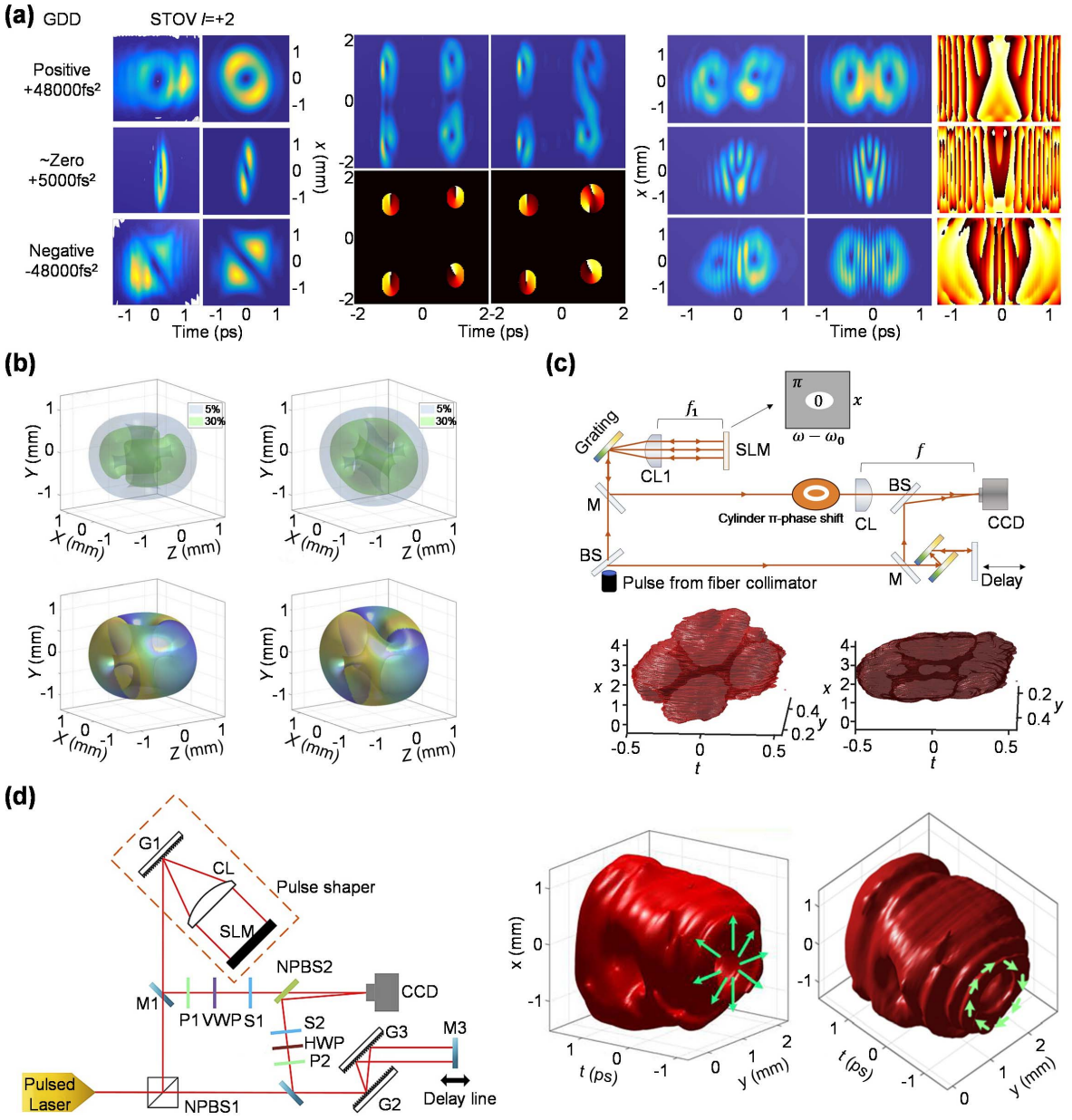


**Fig. 14** Manipulation and interaction of multi-singularities within an STOV wavepacket. (a) Sculpturing spatiotemporal wavepackets with chirped pulses[206]. Left: intensity distributions of STOV wavepackets with different amounts of GDD. Middle: STOV lattice with multiple STOVs multiplexed in space and time. Right: collision of two STOVs. Linear phases with opposite signs are applied on the left/right side of the input light field to advance/delay input wavepackets in the corresponding time domain. (b) Spatiotemporal intensity and phase profile of STOV wavepackets with phase singularities embedded in different space–time domains[207]. By tuning different parameters, the magnitude and orientation of the photonic OAM in space–time can be tuned. (c) Observation of vortex reconnections within an STWP[208]. The transverse crossing of two vortices with a topological charge of one can produce unique vortex loop reconnection patterns. Higher topological charges result in arrays of vortex loops and connection points. (d) Generation of cylindrically polarized STWP with both phase and polarization singularities by cascading a vectorial vortex plate after a pulse shaper[209].

conserved at the individual photon level. As such, the transverse OAM in STOV pulse is conserved in SHG. Mathematically, the second-harmonic STOV pulse generated using a thin BBO crystal can be described by a simple theory. In this straightforward scenario, with perfect phase matching, an undepleted pump approximation, and a lossless medium, the second-harmonic field is proportional to the square of the complex input fundamental field:

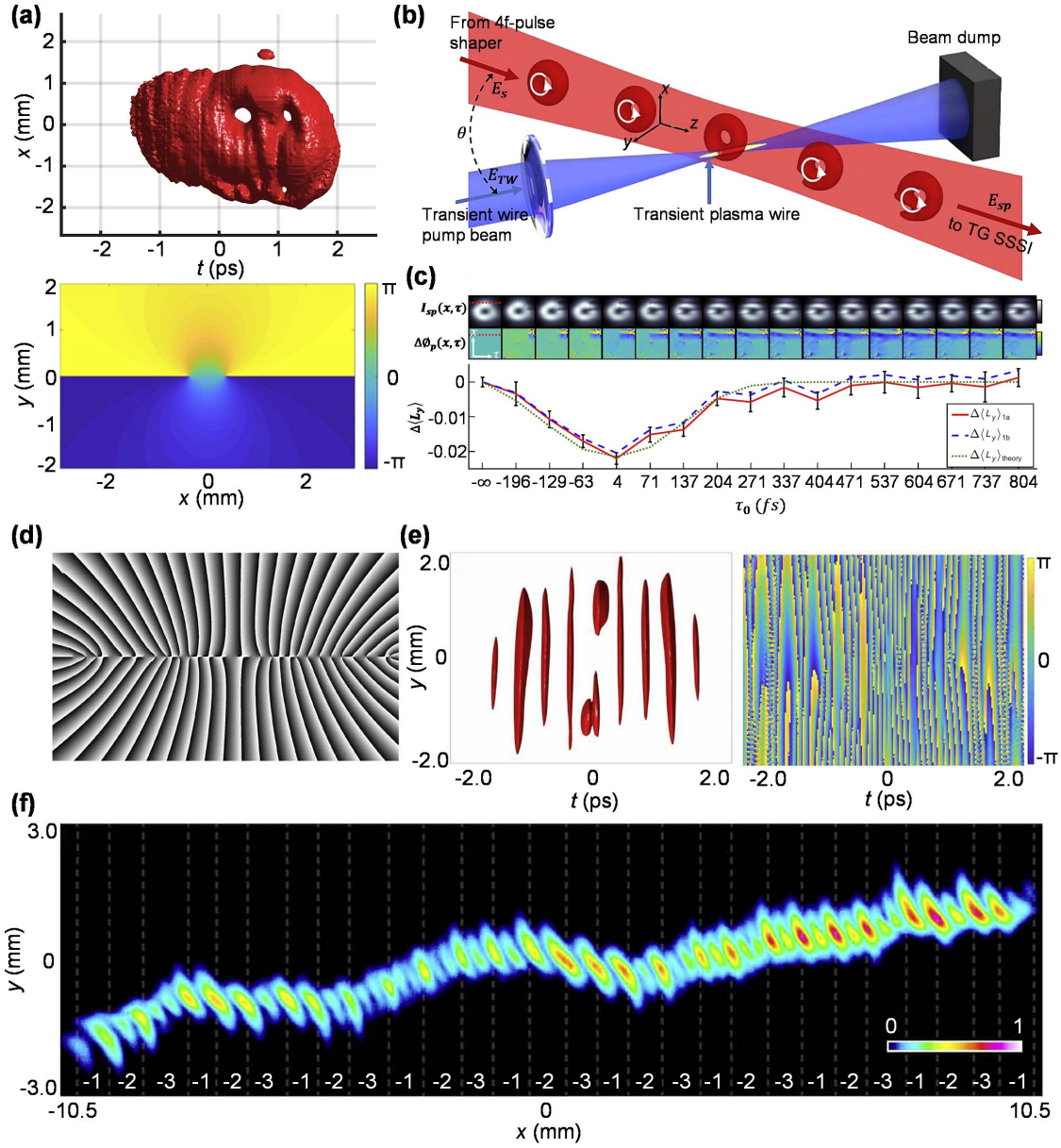


**Fig. 15** STOV wavepackets with time-varying transverse OAM. (a) Generation of rapidly changing transverse OAM within an STOV wavepacket[211]. Top: 3D intensity reconstruction of a wavepacket of two spatiotemporal vortices with dynamic transverse OAM and temporal separation of 0.74 ps. Bottom: corresponding phase pattern loaded onto the SLM inside a 2D pulse shaper. (b) Configuration for measuring the effect of a transient phase perturbation on the ultrafast field imposed by the ultrafast optical field ionization plasma[212]. (c) Effect of transient wire onset time $\tau_0$ on changing the transverse OAM of STOV[212]. (d) A phase pattern loaded on the SLM for generating STPV string with time-dependent transverse OAM[213]. (e) Complex field of generated STOV string[213]. (f) The temporal diffraction pattern of STOV string by a grating[213].

$$E^{2\omega}(x,y,\tau) = A_0 e^{il^{(2\omega)}\Phi(x,y,\tau)} \propto [E^{(\omega)}(x,y,\tau)]^2 \propto (e^{il^{(\omega)}})^2 \propto e^{i2l^{(\omega)}}. \quad (36)$$

Fang *et al.* theoretically studied the HHG of transverse OAM of STOVs[218]. Figure 17(c) shows a spatially resolved HHG spectrum driven by the fundamental STOV with hydrogen atoms and indicates that the $N$th harmonic carries a phase singularity with a topological charge of $Nl_s$, thus verifying the above-mentioned scaling rule. Recently, attosecond pulse trains featuring an STOV structure have been theoretically proposed, generated by a two-color femtosecond light field, with each color carrying transverse OAM and a properly truncated HHG spectrum[219].

### 3.2 STOV in High Dimension and Other Waves

The STOV wavepackets mentioned above are typically generated in optics and localized within the 2D space-time domain. However, in recent years, the generation and control of STOV

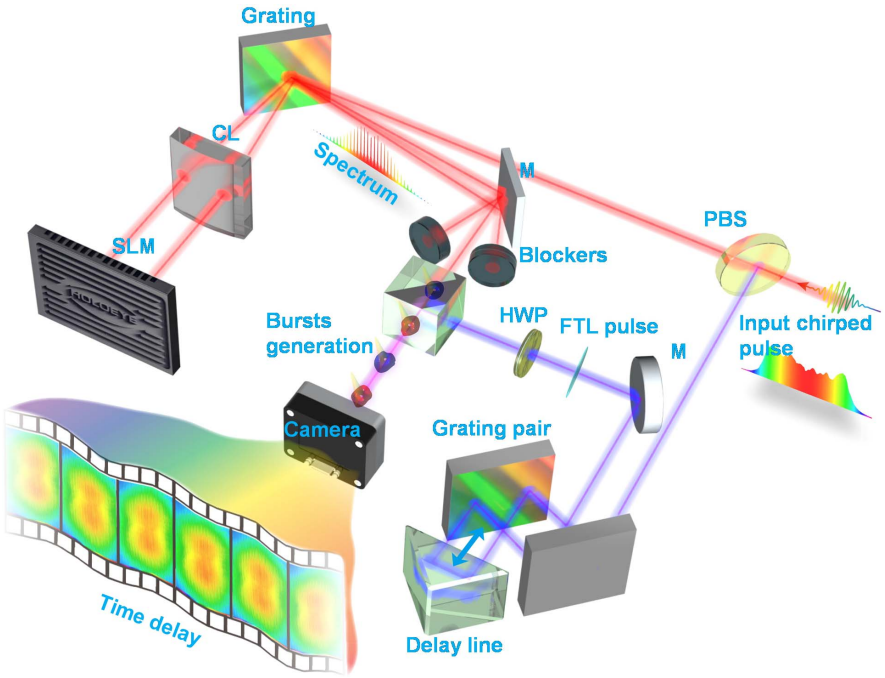


**Fig. 16** Synthesizing spatiotemporal vortex pulse burst with time-varying transverse OAM[214].

wavepackets in other waves' 3D space-time have become a growing area of research, particularly in the study of interactions with acoustic waves and a cascade of further spatial optical transformation systems. By extending to 3D space-time, the potential applications of STOV wavepackets are significantly enhanced, allowing for more precise control in complex physical systems. For instance, 3D STOVs not only offer stronger spatial and temporal structure but also provide a novel experimental platform for investigating many-body effects and nonlinear interactions.

STOVs are essentially 2D spatiotemporal wavepackets in the space-time domain ($x$–$t$ plane) and typically have a uniform distribution or Gaussian profile along the $y$ direction, which is often neglected in some calculations for simplicity. As a

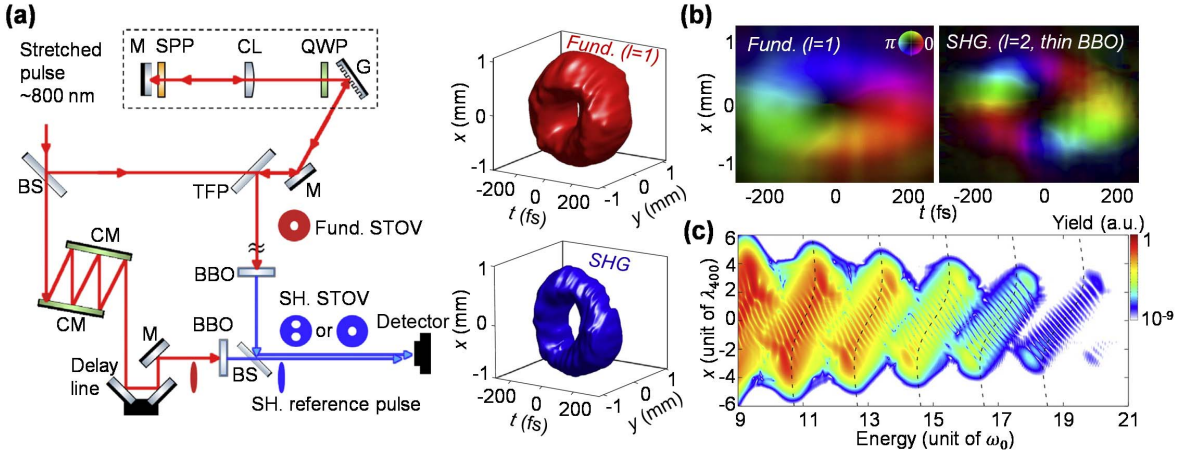


**Fig. 17** Harmonic generation of STOV wavepackets. (a) Second-harmonic spatiotemporal OAM pulse generation and characterization[215]. Left: experimental setup; fundamental STOV of topological charge $\ell = 1$ is generated by a 2D pulse shaper. Second-harmonic STOV is generated in BBO crystals and characterized by interference with reference pulses. Right: experimentally reconstructed 3D intensity iso-surface profile of the fundamental STOV (top) and its second harmonic (bottom). (b) Complex field of fundamental STOV (left) and its second harmonic (right)[215]. The second-harmonic fields with $\ell = 2$ demonstrate the conservation of OAM in an SHG process. (c) Controlling photon transverse OAM in HHG[218]. Spatially resolved HHG spectrum driven by the fundamental STOV with hydrogen atoms.

result, the intrinsic 3D nature of the STWP is reduced to a 2D space due to the one-step reshaping by a 2D pulse shaper. Transformation optics can be utilized to take a leap forward to the customization of 3D spatiotemporal wavepackets. One interesting example is the demonstration of a photon toroidal vortex[129,220]. A toroidal vortex of light is a ring-shaped wavepacket with a poloidal spatiotemporal helical phase. A typical 2D pulse shaper is used to generate an STOV wavepacket with a Gaussian profile along $y$-axis; then this STOV wavepacket is elongated to an STOV tube $(x, y)$ through a pair of cylindrical lenses with a large magnification along $y$-axis and then conformally mapped to a toroidal vortex $(u, v)$ using transformation optics that complete log-polar to Cartesian mapping, as shown in Figs. 18(a) and 18(b). The log-polar to Cartesian coordinate transformation requires $u = b\exp(-x/b)\cos(y/a)$ and $v = b\exp(-x/a)\sin(y/a)$. The first phase mask performs the mapping from a tube to a toroid, and is given by

$$\varphi_1(x,y) = \frac{k_0}{d}\left[-ab\exp\left(-\frac{x}{b}\right)\cos\left(\frac{y}{a}\right) - \frac{x^2+y^2}{2}\right], \tag{37}$$

where $d$ is the distance between the two phase masks, and $a$ and $b$ are used to adjust the beam size and position in the $(u, v)$ plane. To suppress the residual phase, the second phase mask is used to recollimates the light. In the time-reversal direction, the second phase mask performs a Cartesian to log-polar coordinate transformation, which is given by

$$\phi_1(x,y) = \frac{k_0}{d}\left[-au\ln\frac{\sqrt{u^2+v^2}}{b} + av\tan^{-1}\left(\frac{v}{u}\right) + \frac{u^2+v^2}{2}\right]. \tag{38}$$

After travelling through the two-phase masks, the spatiotemporal vortex tube will be mapped into a photonic toroidal vortex.

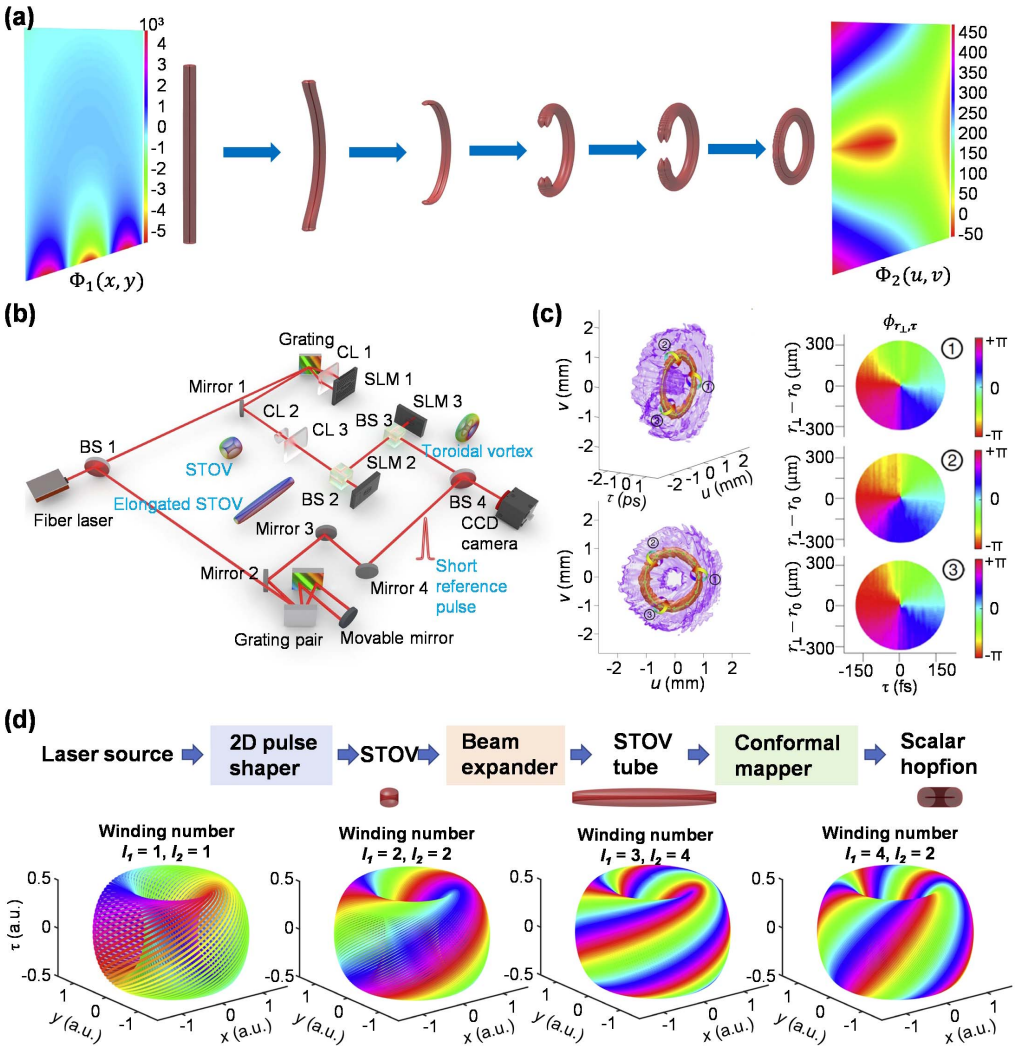


**Fig. 18** High-dimensional manipulations of STWP. (a) Simulation of the conformal mapping from a spatiotemporal vortex tube to a vortex ring through log-polar to Cartesian coordinate transformation[129]. (b) Schematic of the experimental apparatus for STOV wavepacket generation and implementation of the conformal mapping. (c) Experimental reconstruction of the photonic toroidal vortex from different views. (d) Generation of scalar optical hopfions by further applying a spatial helical phase to the $x$–$y$ domain of the generated photonic toroidal vortex[221].

The photonic toroidal vortex possesses a 3D phase structure that rotates around a closed loop, forming a ring-shaped vortex line while advancing in the direction perpendicular to the ring orifice at the speed of light, as shown in Fig. 18(c).

The realization of optical toroidal vortices and toroidal pulses opens new avenues for topological photonics. The techniques used to create toroidal vortices can generate much more complex optical topologies. A recent example is the optical hopfion, a 3D topological state discovered in field theory, magnetics, and hydrodynamics, which resembles particle-like objects in physical space. Building upon the optical toroidal vortex, dynamic scalar optical hopfions in the shape of a toroidal vortex can be created simply by adding a spatial vortex phase, which can be shown as a solution to Maxwell's equations under the paraxial approximation[221]. This spatiotemporally varied optical hopfion is proposed through an analytical expression as an approximate solution to Maxwell's equations. Numerical simulations and experimental data demonstrate that the equiphase lines form disjoint and linked closed loops, manifesting as links and knots with a linking number determined by the Hopf invariant. As shown in Fig. 18(d), each closed loop, painted in a specific color, corresponds to a point in the parameter space and to a circle on the unit sphere in 4D space. These closed loops are equiphase lines, and all equiphase loops collectively form complete tori that fill the entire 3D space.

The above toroidal vortex generated from the conformal mapping of an STOV has a ring-shaped symmetric 3D structure, which is a solution of the scalar wave equation in a uniform medium with anomalous group velocity dispersion, and can be approximately expressed as

$$\Psi(x,y,\tau)=\left[\frac{\sqrt{(r_\perp-r_0)^2}}{\sqrt{z_0}}\right]^l\exp\left[-\frac{(r_\perp-r_0)^2+\tau^2}{2z_0}\right]\times\exp\left[-il\tan^{-1}\left(\frac{\tau}{r_\perp-r_0}\right)\right],\tag{39}$$

where $r_\perp=\sqrt{u^2+v^2}$, $r_0$ is the spatial radius of the circular vortex line. Recently, Chen *et al.* introduced "photonic conchs" theoretically as a new type of toroidal-like state exhibiting geometrical chirality, and experimentally observed these wavepackets with controllable topological charges. The BeSTOV wavepacket is used to generate a vortex tube, and then the tube is conformally mapped into a photon conch through Cartesian to log-polar transformation. Instead of a symmetric form, the chiral symmetry breaking log-polar to Cartesian coordinate transformation is $u=r_0\exp[-(ay+x)/b]\cos[(y-ax)/b]$ and $v=r_0\exp[-(ay+x)/b]\sin[(y-ax)/b]$. The generated photon conch has a spiral intensity 3D distribution, as shown in Fig. 19(a). Notable, the photon conch exhibits space–time varying OAM density due to its changing integral OAM value during evolution[222]. Lin *et al.* produced a spatiotemporal coupling wavepacket, light spring pulse, by means of spatial dispersion and conformal mapper, in which a tilted pulse front of an ultrafast light field is introduced, thereby producing a space-dependent time delay, then performing a geometrical transformation to spatially shape the pulse front tilted laser, as shown in Fig. 19(b). The pulse front tilted pulse, created through angular dispersion, exhibits continuous spatiotemporal variation, resulting in a high-quality beam for the targeted STC of a light field. The generated STWPs show a single-coil light spring and

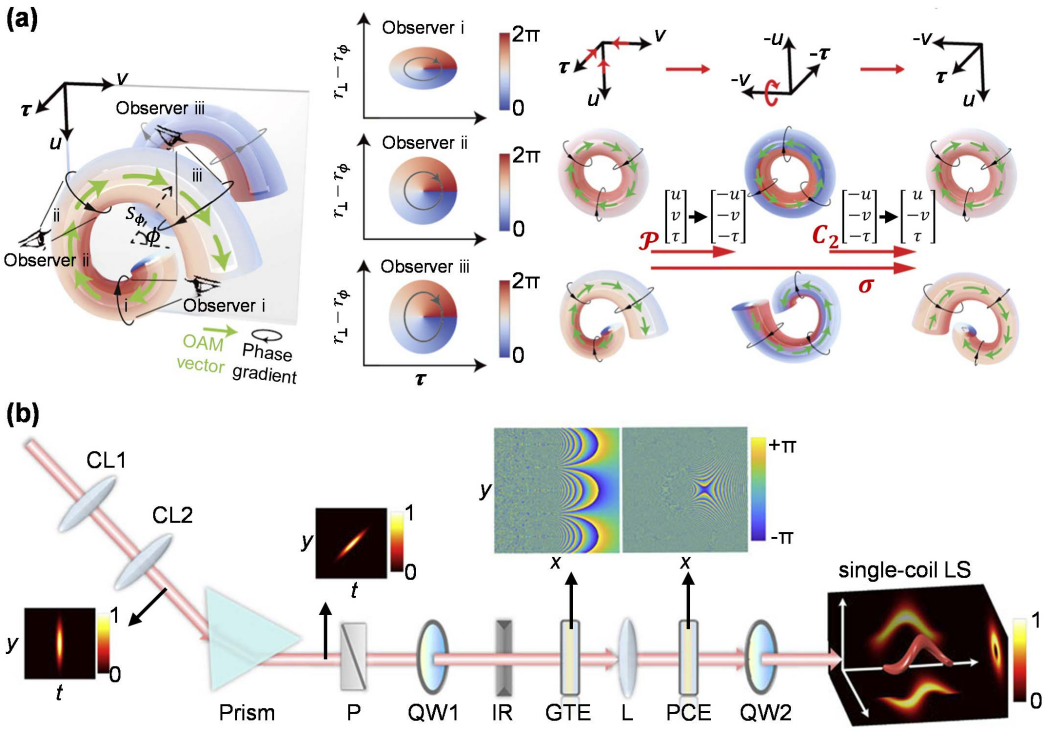


**Fig. 19** Generation of high-dimensional STWP based on conformal mapper. (a) Photonic conch with symmetry breaking[222]. (b) Generation of a light spring with time-varying OAM through the conformal mapping of a spatially azimuthal dispersive pulsed beam[223].

possess a tunable topological charge with a broad topological charge bandwidth[223].

The STOV wavepackets are also applicable to other physical fields that involve wave phenomena. Bliokh[224] was the first to describe the transverse OAM properties of STOV wavepackets in acoustic and quantum-relativistic contexts, with different spins and masses. The transverse intrinsic OAM has a universal form across these cases. The OAM of acoustic pulses is determined by the mechanical angular momentum of the medium particles moving due to wave-induced Stokes drift. In 2023, Ge *et al.* developed the STOV concept in the field of acoustics and reported the generation of acoustic Bessel-type STOVs[225]. Figure 20(a) shows the basic experimental setup for generating and measuring acoustic STOV wavepackets. An acoustic phased array, controlled by a multichannel sound card, represents 10 modes with their spatial frequencies distributed equally on the Dirac-circle. The emitter has a center spatial frequency of $k_0 = 119\,(\mathrm{rad/m})$ and a bandwidth of $\Delta k = 0.15k_0$,

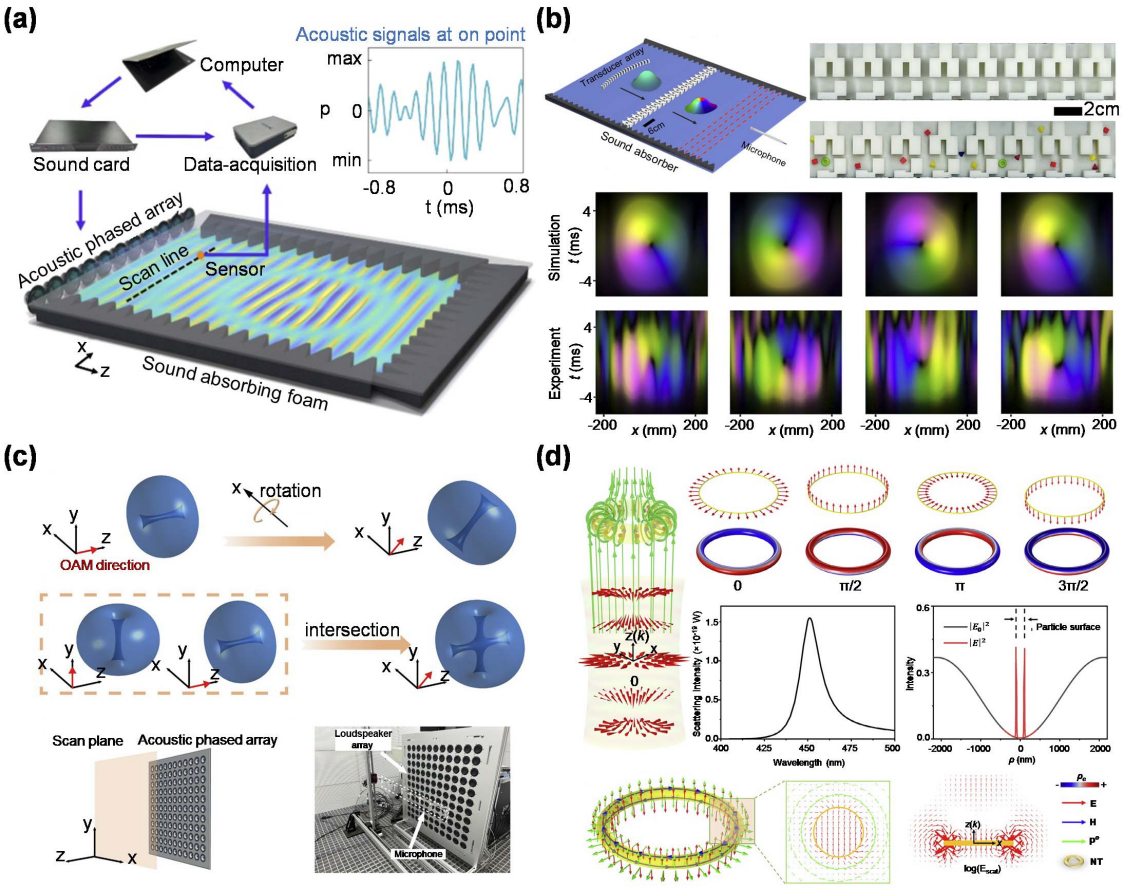


**Fig. 20** STOV generated in other wave phenomena. (a) Schematic of the experimental setup for acoustic STOV wavepacket generation and measurement. The acoustic STOV wavepacket is generated by an acoustic phased array and measured along a scan line. A separate pulse signal from the sound card synchronously triggers each recording. The inset shows a time sequence of acoustic signals acquired at one point[225]. (b) A meta-grating with broken spatial mirror symmetry for the generation of acoustic STOV wavepackets. The meta-grating exhibits vortices in the transmission spectrum function in the momentum–frequency domain, which appear in pairs at the critical value of the asymmetry parameter[226]. (c) Synthesizing 3D acoustic STOVs with OAM oriented in arbitrary directions[227]. There are two methods for manipulating OAM orientation: the first approach involves the direct rotation of wavepackets carrying longitudinal or transverse OAM in 3D space (top left); the second approach is achieved through the intersection of vortices carrying longitudinal and transverse OAM. By modifying the topological charges of these vortices, the orientation of the tilted OAM can be adjusted (top right). (d) Plasmonic toroidal vortex generation under radially polarized beam illumination[228]. Left: configuration of a plasmonic nanotorus under a radially polarized beam. Top: electric field evolution and surface charge distribution on a gold nanotorus at four resonance phases. Middle: simulated scattering intensity and field enhancement; comparison of light intensity with and without the nanotorus. Bottom: simulated electric and magnetic fields, and orbital momentum density of scattered light; detailed view of the electric field and orbital momentum density; broader $x$–$z$ plane electric field distribution with the nanotorus marked in yellow.

corresponding to an acoustic frequency range of 5525–7475 Hz. The acoustic phased array consists of 20 speakers spaced 3.3 cm apart. The acoustic STOV wavepackets can be characterized either in the $x$–$z$ plane by a time snapshot or in the $x$–$t$ spatial-temporal domain at a fixed $z$ position. A typical time sequence of acoustic signals at each point along a scan line is shown in the inset of Fig. 20(a). Zhang *et al.* utilized an acoustic meta-grating to robustly generate acoustic STOV wavepackets, as shown in Fig. 20(b). This meta-grating, which has broken mirror symmetry and is controlled by a synthetic asymmetry parameter, exhibits a pair of singularities in the transmission spectrum function within the frequency-momentum domain[226]. This method provides topological protection against structural disorder of the meta-grating, ensuring the generation of high-quality acoustic STOV wavepackets even under random distortion, as shown at the bottom of Fig. 20(b). The above-mentioned acoustic STOVs exist in 2D space and carry purely transverse OAM. Recently, the 3D acoustic STOV wavepackets with arbitrary orientated OAM have also been reported by Liu *et al.*[227]. The authors introduced two approaches to manipulate the orientation of OAM: through the direct rotation of vortices in 3D space and the intersection of vortices carrying distinct types of OAM, as shown in Fig. 20(c). The orientation of OAM can be regarded as a new degree of freedom, offering potential advantages in the field of acoustic communications. In addition, Yang *et al.* have theoretically presented the generation of a plasmonic toroidal vortex, which is a novel manifestation of the toroidal vortex within the realm of nano-plasmonics[228]. The plasmonic toroidal vortex is created by directing a radially polarized beam onto a plasmonic nanotorus positioned strategically where the longitudinal and radial fields of the incident wave achieve equal strength, as shown in Fig. 20(d). Besides, 2D van der Waals materials can confine light to subwavelength scales and support hyperbolic polaritons, a unique light-matter interaction mode where light is guided along conical rays. Hence, Zhang *et al.* recently introduced a time-domain near-field interferometry approach to characterize the spatiotemporal beating of hyperbolic polaritons as they undergo total internal reflections within the van der Waals material. These reflections generate STOVs on the nanometer (60 nm) and femtosecond (40 fs) scales along the propagation trajectory[229]. This result presents opportunities for chiral spatiotemporal control of light-matter interactions.

### 3.3 Diffraction-Free Space–Time Light Sheet Wavepackets

Another typical example of the spatiotemporal coupling wavepackets is the space-time light sheet wavepacket, which features a 2D pattern in space-time that can remain nearly nondiffracting during propagation[123,124]. The evolution of light beams can be described by a superposition of plane waves with different spectral-space frequencies:

$$E(x,z,t)=\iint \tilde{E}_0(k_x,\omega)e^{i(k_x x+k_z z-\omega t)}\mathrm{d}k_x\mathrm{d}\omega, \tag{40}$$

where $\tilde{E}_0(k_x,\omega)$ is the Fourier transform of $E(x,z=0,t)$ at $z=0$. $k_x$ and $k_z$ are the transverse and longitudinal wavenumbers, respectively, having a relationship with $\omega$, given by

$$k_x^2+k_z^2=\frac{\omega^2}{c^2}, \tag{41}$$

where the $y$-component is neglected, i.e., $k_y=0$. Equation (41) denotes a light-cone[126], as shown in Figs. 21(a)–21(d). For a monochromatic continuous wave light beam, the spatial spectra lie on circles at the intersection of the light-cone [described by Eq. (39)] with an iso-frequency plane $\omega=\omega_0$ [Fig. 21(a)], whose plane wave expansion is $E(x,z,t)=\iint \tilde{E}_0(k_x,\omega)\delta(\omega-\omega_0)e^{i(k_x x+k_z z-\omega t)}\mathrm{d}k_x\mathrm{d}\omega=\iint \tilde{E}_0(k_x)e^{i(k_x x+k_z z)}\mathrm{d}k_x$, such that all the spatial frequencies are assigned to the same temporal frequency, resulting in diffractive spreading during propagation, as shown in Fig. 21(a). For a pulsed light beam, the spatial spectra corresponds in general to a "patch" on the light-cone, as shown in Fig. 21(b), such that each $k_x$ is assigned to multiple frequencies. The multi-point mapping between $k_x$ and $\omega$ leads to the different $k_z$ associated with each $k_x$ or $\omega$ and further results in diffractive and dispersive spreading. Instead, the space-time light sheet wavepackets have 1D spectral trajectories on the light-cone, as shown in Figs. 21(c) and 21(d), where $|k_x|$ and $\omega$ have a one-to-one correspondence, like the intersection line of the light-cone with spatiotemporal spectral planes at a tilted angle $\phi$. As such, the 2D spectrum $\tilde{E}_0(k_x,\omega)$ is now reduced to the 1D form $\tilde{E}_0(k_x)\delta[\omega-\omega(k_x)]$ and $k_z$ becomes a function of $k_x$ only. The integral now simplifies to

$$E(x,z,t)=\int \tilde{E}_0(k_x)e^{i[k_x x+k_z(k_x)z-\omega(k_x)t]}\mathrm{d}k_x. \tag{42}$$

The tilted spatiotemporal spectral planes can be expressed as

$$\frac{\omega}{c}-k_0=(k_z-k_0)\cot\phi, \tag{43}$$

where $\phi$ is the spectral tilt angle with respect to the $\omega$ axis. Such a constraint results in transforming a wavepacket $E(x,z,t)=\Psi(x,z,t)e^{i(k_0 z-\omega_0 t)}$ into the reduced form $E(x,z,t)=\Psi(x,z-ct\tan\phi)e^{i(k_0 z-\omega_0 t)}$. Therefore, such space-time light sheets are indeed all pseudo-diffraction-free through rigid transport of the envelope $\Psi(x,z)$ with a group velocity $v_g=c\tan\phi$. To synthesize such a wavepacket, the authors utilized a 2D pulse shaper to efficiently synthesize pulsed light beams with the above spatial-spectral correlations, as shown in Fig. 21(e). The initial pulsed beam is a pulsed plane wave $E(x,0,t)=E(t)$, whose separable space-spectrum is $\tilde{E}(k_x,\lambda)=\tilde{E}(\lambda)\delta(k_x)$ and spatially spreads the spectrum along the $y$-axis with a grating. As such, for each temporal frequency, spatial frequencies can be imprinted through a 2D phase mask, given by

$$\Phi(x,y)=\mathrm{mod}\left\{\mathrm{sign}[\alpha]\cdot|x|\cdot\sqrt{2\alpha|y|},2\pi\right\}, \tag{44}$$

where $\alpha=1/c-1/v_g=c\cot\phi$. Some typical phase holograms and resultant space-time spectrum are shown in Fig. 21(f). After the phase mask, each wavelength is assigned a linearly varying phase, where the slope corresponds to a specific $k_x=\sqrt{2\alpha k_0(\omega-\omega_0)}$. Figure 21(g) shows the experimentally measured space-spectrum of the output pulse, demonstrating a tight relationship between $k_x$ and $\omega$, resulting in a spatiotemporally non-separable wavepacket. Such STWPs maintain peak integral intensity with a narrow spatial size and can preserve their profile unchanged over several Rayleigh lengths, as shown in Fig. 21(g). The theoretical model assumes infinite spectral resolution, which is not feasible in practice due to the limited dispersive power of optical devices, the spectral content of the source, and the pixel of the SLM. Consequently,

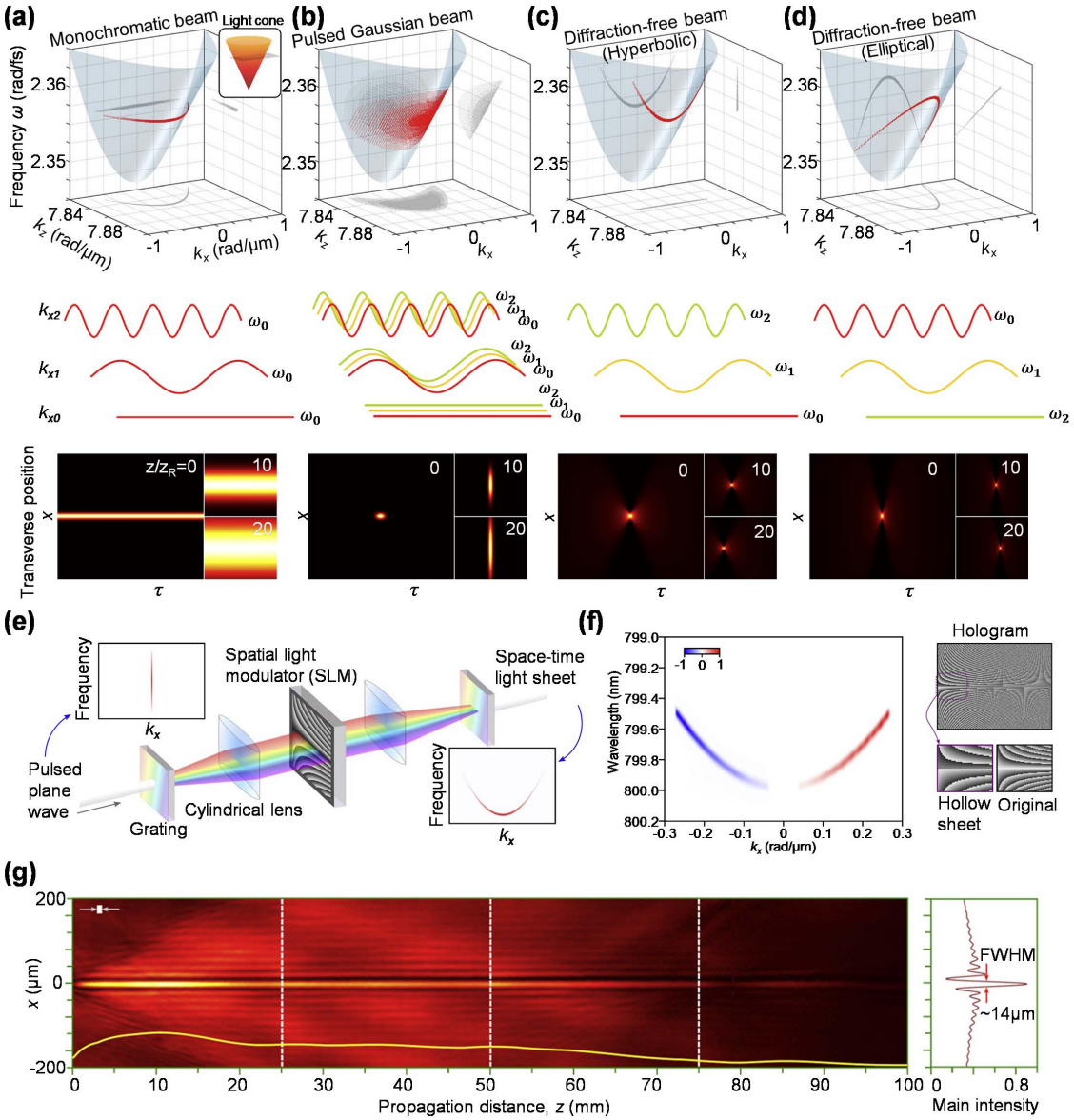


**Fig. 21** Diffraction-free STWPs: space–time light sheet[126]. Top: (a)–(d) Light fields explained with the superposition of plane waves lie on the surface of a $k_x - \omega$ light-cone. (a) A continuous monochromatic beam lies on the intersection of the light-cone with an iso-frequency plane, featured by a narrow temporal frequency range ($\Delta\omega$) and a wide spatial frequency range ($\Delta k_x$). These optical fields exhibit diffractive spreading during propagation. (b) A pulsed Gaussian beam corresponding to a patch on the light-cone has a wide range in both spatial and temporal frequencies. These optical fields exhibit diffractive and dispersive spreading during propagation in a dispersive medium. (c), (d) Diffraction-free space–time light sheet lies on the intersection of the light-cone with a tilted frequency plane (parallel to $k_x$ axis), and has a tight relationship between spatial frequency and temporal frequency (each $k_x$ is associated with a unique $\omega$). Such STWPs exhibit diffraction-free property and controllable group velocity during propagation. (e) Synthesis and analysis of diffraction-free space–time light sheets. The spatiotemporal frequency relationship is created by a phase-only mask via the 2D pulse shaper. The input pulsed beam is a pulsed plane wave. (f) Measured space–time spectral intensity $|\tilde{\Psi}(k_x, \lambda)|^2$ of a hollow light sheet, with the $\pi$-step implemented along $k_x$ superimposed. (g) Measured temporal integral intensity $I(x, z) = \int_{-T}^{+T} |\Psi(x, z, t)|^2 \mathrm{d}t$ of the space–time light sheet at various propagation distances. The insert denotes the Rayleigh length. The results verify the propagation-free property of the generated space–time light sheet wavepacket.

there is always a finite spectral uncertainty associated with these STWP synthesizers. This spectral uncertainty influences the characteristics and quality of the generated propagation-invariant STWPs by affecting their group velocities and diffraction-free propagation distance. Based on this scheme, STWPs with unique properties have also been structured, such as space-time Airy wavepackets with non-acceleration[230], space-time veiled Talbot effect[231], etc.; for details, please refer to the recent review on space-time light sheet wavepackets[125].

### 3.4 Time-Varying Helical Wavepackets

The conventional OAM carried by a pulsed beam typically remains static and does not vary over time. A significant hurdle in efficiently managing the temporal characteristics of light for practical applications lies in the slow modulation speeds of current technologies. STWPs with correlations between transverse spatial fields and temporal frequency spectra can lead to unique spatiotemporal dynamics, enabling control of instantaneous light properties. A particularly interesting type of spatiotemporal coupling wavepacket is the helical beam, or light spring, with temporally varied properties—essentially an STWP containing time-varying OAM. Such self-torque pulses have been demonstrated in a high harmonic generation driven by two collinear and linearly polarized infrared pulses with different OAMs and a time delay between them[127] [Fig. 22(a)]. However, this setup is bulky, expensive, and complex to synthesize and characterize. In contrast, this type of STWP can be easily synthesized using OAM pulses with different center frequencies and topological charges in linear optics[232,233], as shown in Figs. 22(b) and 22(c). Multiple optical-frequency-comb lines with superposition of Laguerre–Gaussian modes for each line have been proposed and numerically studied to produce spatiotemporal beams with dynamic rotation (OAM) along a spring-like trajectory[128] [Fig. 22(d)]. However, the spatiotemporal dynamics generated by previous approaches manifest at a specific propagation distance and are not arbitrarily tailorable along the longitudinal path. Recently, based on Frozen Wave theory, Su *et al.* demonstrated a new class of versatile, judiciously synthesized STWPs, whose spatiotemporal evolution can be engineered to occur at various predesigned distances along the longitudinal propagation path [Fig. 22(e)][234].

In addition, the compact footprint and ease of fabrication make nanophotonic devices ideal candidates for developing flat optical components integrated into on-chip devices. In this context, a time-modulated metasurface with an azimuthal frequency gradient has been theoretically proposed to generate vortex pulses with time-varying topological charges[235] [Fig. 22(f)]. In addition, nanophotonic devices also provide multidimensional modulation (phase, polarization, and amplitude) capability within the same device, representing another advantage over the traditional phase-only SLM-based pulse shaper configurations. Chen *et al.* demonstrated a versatile photonic platform capable of controlling the complete 4D spatiotemporal evolution of ultrafast pulses over an ultrawide bandwidth by leveraging the multidimensional control of light at the nanoscale offered by metasurfaces[236]. This platform enables the synthesis of wavepackets with time-varying polarization and temporally encoded spatial-wavefront evolution, as shown in Fig. 22(g). Recently, Chen[237] and Liu *et al.*[238] nearly simultaneously achieved an integrated optical vortex microcomb by merging optical vortices with whispering gallery mode microresonators. This integrated nonlinear ring microresonator can emit spatiotemporal light springs comprising 50 OAM modes. Each frequency of the microcomb carries a unique OAM value, as illustrated in Figs. 22(h) and 22(i).

Most methods for space-time beam shaping typically involve a multi-step process. Briefly, in a standard 2D pulse shaper, the frequencies of the incoming laser pulse are first angularly dispersed by a grating, and then a holographic device positioned at the Fourier plane of the grating modulates the spatially separated spectral components of the input pulse. When applying these methods to establish a relationship between the frequencies and topological charges of pulsed beams, it becomes evident that the linear geometry of conventional pulse shapers does not align well with the circular symmetry of OAM-carrying beams. This inherent mismatch limits the demonstrations of topological-spectral correlations to pulses with a restricted OAM bandwidth, typically around unity. Therefore, most demonstrations also operate within a relatively narrow band of optical frequencies, corresponding to pulse durations in the picosecond range. A relatively compact setup using diffractive axicons with circular geometry was employed by Piccardo *et al.* recently to create broadband topological correlations in space-time beams and produce light coils[239]. The diffractive axicon enables radial separation of laser pulse frequencies on an SLM, enabling independent addressing and shaping, as shown in Figs. 23(a)–23(d). This capability extends to handling ultrashort, highly broadband laser pulses, facilitating the precise shaping of 7 fs pulses from a noncollinear optical parametric amplifier, as shown in Fig. 23(e). The results extend the ability to encode orbital angular momentum in ultrashort pulses, with correlations between frequency and topological charges being produced and tailored over a bandwidth of 200 nm in the visible range and helicity values up to 80, as shown in Figs. 23(a), 23(b), and 23(f). Recently, Oliveira *et al.*[240] proposed a method to introduce femtosecond-scale modulation of light's orbital angular momentum (OAM) through engineered space-time coupling in ultrashort pulses, dynamically altering spatial distribution via azimuthally varying wavefront transformations and demonstrating self-torqued wavepackets with rapid temporal OAM changes and angular self-acceleration capabilities, as shown in Fig. 23(g). In this setup, the time-varying wavepackets with self-torque at a femtosecond timescale [Fig. 23(h)] and angular self-acceleration [Fig. 23(i)] are successfully generated.

Since one spatial dimension is used to map the pulse spectrum in a 2D pulse shaper, spatial shaping cannot be applied along this dimension, limiting the setup to 2D STWP manipulation. Consequently, achieving comprehensive three-dimensional space-time control with this method is likely unattainable. Although conventional spatial modulation elements (such as SLMs and vortex plates) can be cascaded, the resulting wavepackets remain spatiotemporally separable. To address this issue, Cruz-Delgado *et al.* report on the production of fully three-dimensional STWPs, marking a significant advance in manipulating space-time electromagnetic wavepackets in all dimensions[241], in which they combine a 2D pulse shaper with a spatial mode multiplexer borrowed from telecommunication systems and based on an MPLC device, as shown in Figs. 24(a) and 24(b). The MPLC can convert a linear array of Gaussian beams into a set of co-propagating two-dimensional spatial modes. The first module is a typical 2D pulse shaper that imprints a linear spectral phase profile along the direction in which the pulse spectrum is spread. Simultaneously, it

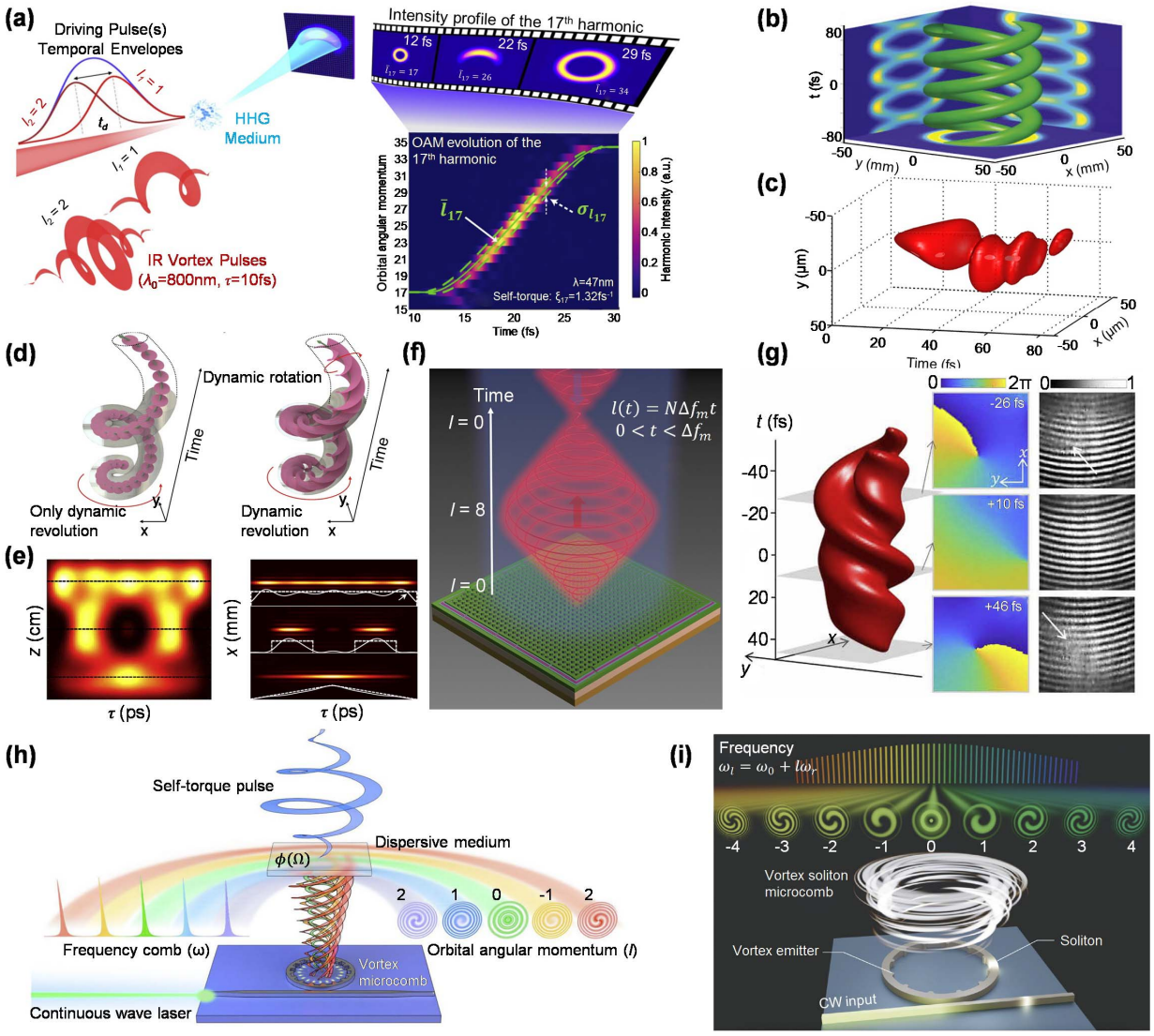


**Fig. 22** Light spring wavepackets with time-varying properties. (a) Generation of EUV beams with self-torque. Two time-delayed, collinear IR pulses with the same wavelength (800 nm) but different OAM values are focused on an argon gas target, serving as the HHG medium[127]. This setup produces harmonic beams with self-torque. The intensity profile varies at different radii over time during the emission process, resulting in a pulsed beam with temporally varying OAM. (b) A spatiotemporal light spring is achieved by imprinting spatially azimuthal mode indices of a Laguerre–Gauss beam onto the pulsed frequency[232]. (c) Propagation-invariant spatiotemporal helical wavepackets carrying OAM that evolve on spiraling trajectories in both time and space in bulk media or multimode fibers[233]. (d) Generation of spatiotemporal coupling wavepackets exhibiting both dynamic rotation and revolution is achieved by coherently adding multiple frequency comb lines[128]. (e) Synthesizing spatiotemporal coupling wavepackets with temporally and longitudinally varying dynamics involves introducing a spectrum that includes both temporal and longitudinal wavenumbers[234]. This spectrum is associated with specific transverse Bessel-Gaussian fields. (f) The schematic demonstrates a time-varying optical vortex generated by reflecting a laser beam off a time-modulated metasurface with an azimuthal frequency gradient[235]. The beam exhibits a ring-shaped intensity pattern whose radius continuously and periodically oscillates due to variations in the topological charge. (g) Generating a spatiotemporal coupling wavepacket that carries time-dependent OAM and exhibits polarization-swept using a pulse shaper in conjunction with a metasurface[236]. (h), (i) An integrated optical vortex microcomb capable of simultaneously emitting spatiotemporal light springs comprising 50 OAM modes, with each frequency of the microcomb carrying a unique OAM value[237,238].

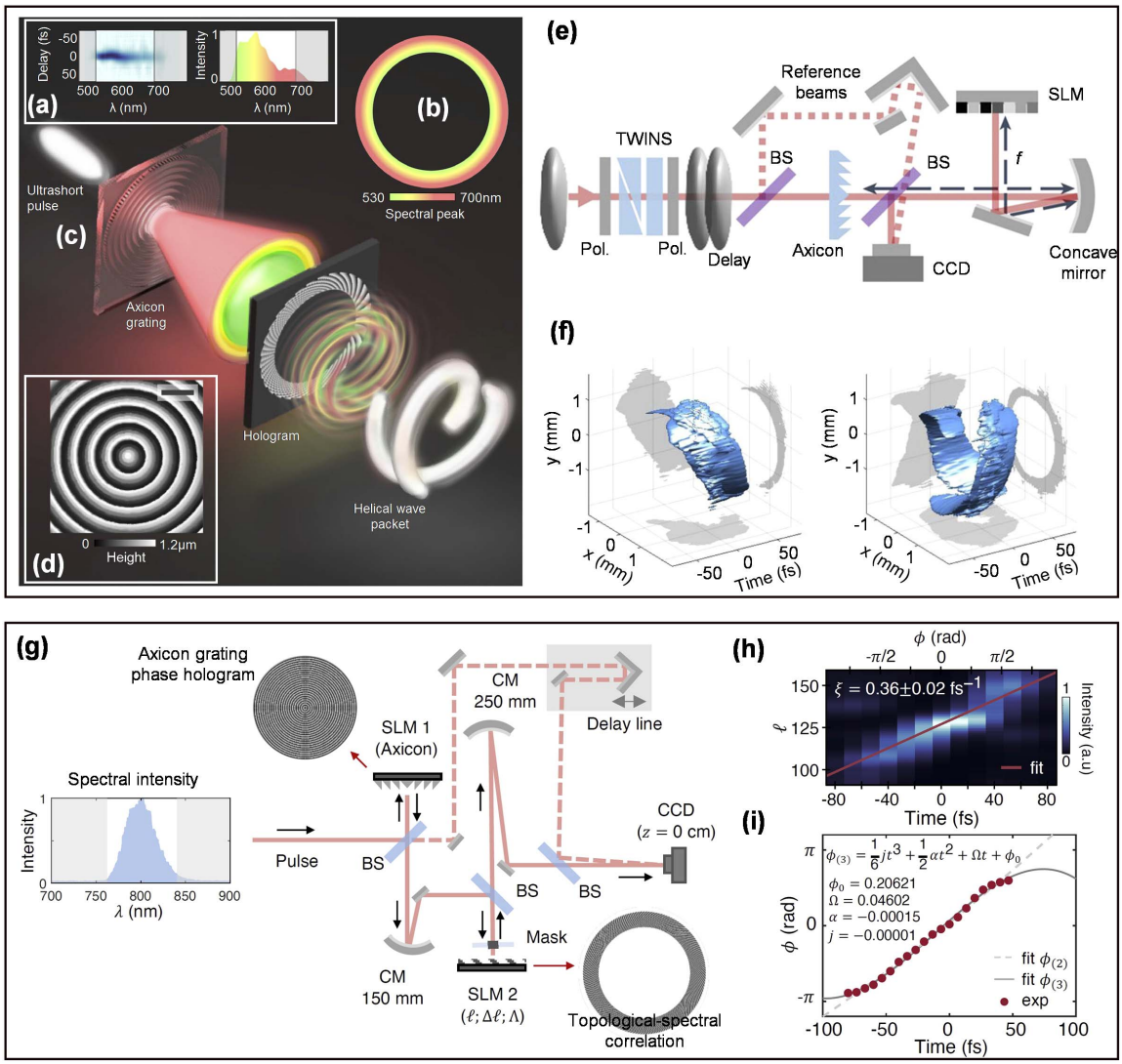


**Fig. 23** Light coils with broadband topological-spectral correlations. (a) Characterization trace of the femtosecond pulses from the NOPA measured by polarization-gated frequency-resolved optical gating (left). The intensity spectrum covers a broad portion of the visible range (right). (b) Spectral peak distribution in the far field of the axicon characterized by a hyperspectral camera[239]. (c) Conceptual scheme for space–time beam shaping involves an axicon grating that maps the spectral content of the input ultrashort pulse into concentric rings. A hologram displayed on an SLM in the far field of the axicon customizes a topological-spectral correlation, yielding helical wavepackets. (d) Optical profilometry image of the fabricated gray-scale axicon. Scale bar: 50 μm. (e) Diagram of the spatially resolved spectral setup designed for space-time beam characterization. This setup integrates a spatial interferometer utilizing off-axis digital holography with a temporal interferometer employing Fourier transform spectroscopy. Both are unified within a common-path birefringent interferometer. (f) Iso-intensity surfaces of synthesized helical wavepacket with specific correlations. (g) Digital Fourier space–time beam shaper for helical wavepackets with time-varying OAM at femtosecond timescale[240]. The ultrashort pulse is incident normal an axicon grating, which is encoded as a phase hologram on the first SLM, which maps the spectral content into concentric rings in the far field. A metallic disk mask placed is used to block the zero order of the first SLM. A hologram displayed on a second SLM in the far field imparts a topological-spectral correlation. The helical wavepackets are generated at the imaging plane of the first SLM. The characterization setup combines a delay line and spatial interferometer based on off-axis digital holography. The interference images are recorded by the charge-coupled device camera located at the imaging plane of the first SLM. CM, concave mirror; BS, beam splitter; CCD; charge-coupled device. (h) Modal decomposition analysis of the synthesized helical wavepacket confirming a continuous increase in topological charges, signifying a dynamically evolving OAM and a measured self-torque of 0.36 $fs^{-1}$. (i) Analysis of the wavepacket's angular position over time of a generated angular self-acceleration wavepacket, fitted with a third-degree polynomial.

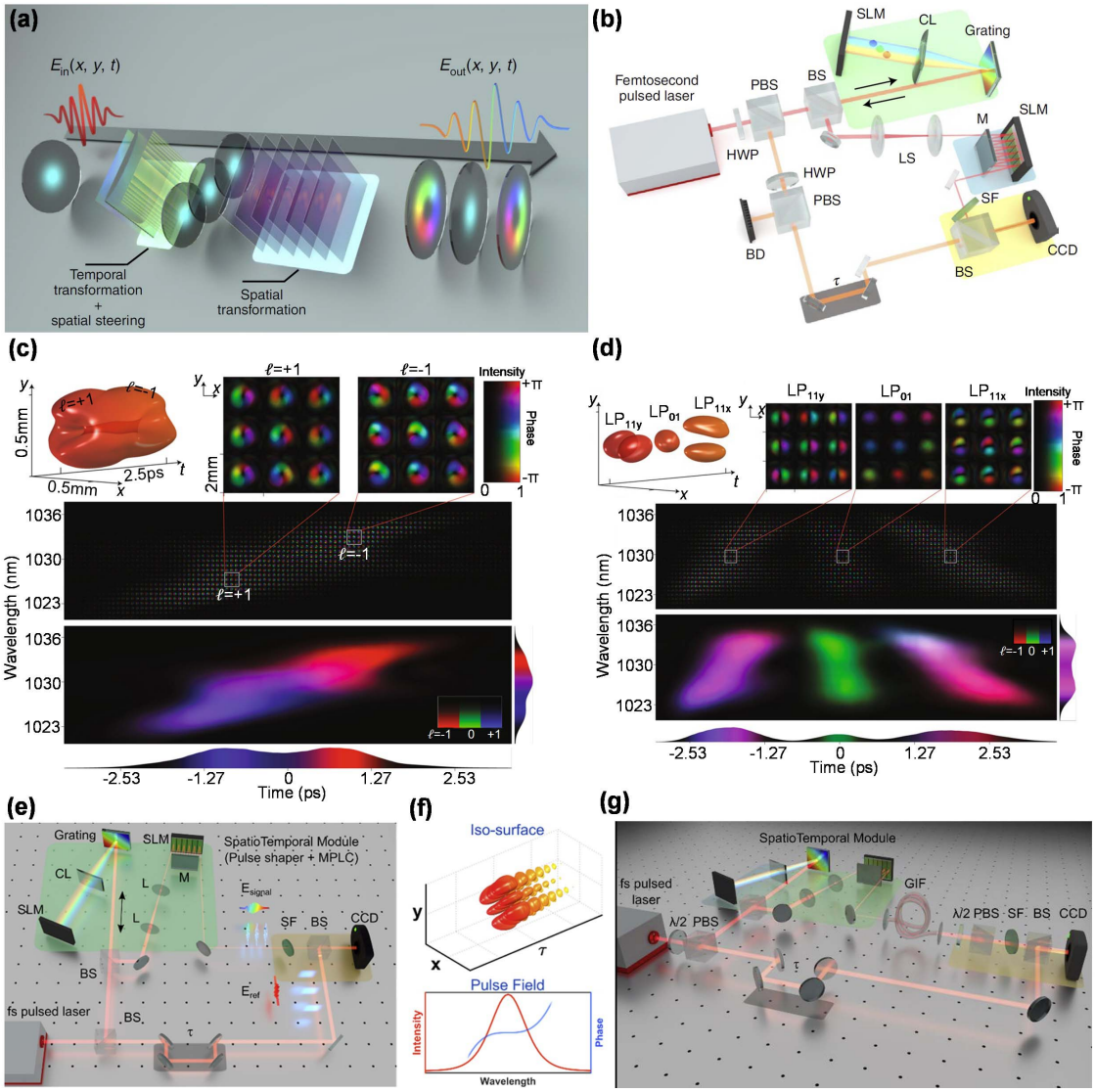


**Fig. 24** Synthesis of STWPs with tailored spatiotemporal properties. (a), (b) Generation of spatially and temporally correlated wavepackets using the combination of 2D pulse shaper and MPLC. The MPLC cascaded after the 2D pulse shaper enabling the precise engineering of the space–time correlation[241]. The 2D pulse shaper is used to steer the spectrally modulated pulse to different spatial positions with distinct time delays before entering an MPLC system. The MPLC comprising an SLM and a mirror is used to modulate the spatial phase and intensity profiles of each pulse spot at different spatial positions. (c) Synthesized STWP with spectral and time-dependent OAM. (d) Synthesized STWP with an intricate spatiotemporal texture comprised of HG basis. (e) Synthesis and analysis of multidimensional ultrashort pulses[242]. (f) Reconstructed iso-intensity profile (top) and retrieved pulse field attributes (bottom) of the optical field. (g) Transport of spatiotemporal light pulses in multimode waveguides[243].

differentially steers the frequencies along a set of vertical positions. Thus, at the output of the pulse shaper, the field comprises a set of $N$ temporally shaped pulses centered at different frequencies, with Gaussian spatial distributions evenly spread along a vertical array of positions. After passing through relay lenses, the field is sent to the second module to engineer the spatial phases and amplitudes of the $N$ sub-pulses. When entering the second MPLC system, the light bounces back and forth between an SLM and a mirror that faces each other. At each reflection on the SLM, a spatial phase is imparted, gradually morphing the 2D field. After six bounces, a careful design of the six holograms on the SLM enables a Gaussian beam at any given vertical coordinates to be adiabatically transformed into a specific spatial basis (LG and HG modes) at the output of the MPLC. The resultant wavepackets show time-dependent and spectra-dependent longitudinal OAM properties by allocating different LG bases at different parts of the spectrum, as shown in Fig. 24(c). This setup can be readily reconfigured on demand to produce even more elaborate optical-field structures. Figure 24(d) exhibits the generation of a wavepacket involving a

temporal train of three pulses, each assigned to a different spatial HG mode with a distinct prescribed frequency chirp, resulting in a non-separable wavepacket. After successfully synthesizing 3D STWPs, discerning their complete physical properties is crucial for effectively harnessing these spatiotemporal light structures. To address this, Cruz-Delgado *et al.* developed a ptychography technique to characterize optical fields with dynamic spatial and spectral structures[242], as shown in Fig. 24(e). Using a frequency-resolved holographic technique, which provides the complex (amplitude/phase) spatial composition of each spectral component at different time locations, the iso-surface and pulse attributes of 3D STWPs can be reconstructed, as depicted in Fig. 24(f). Recently, Cruz-Delgado *et al.* tailored the spatiotemporal structure of ultrashort light pulses to overcome the physical limitations imposed by chromatic and modal dispersion in multimode optical fibers[243]. By applying a sequence of transformations via a pulse shaper and MPLC device, they synthesized light states with predefined spatial and chromatic dynamics, effectively shaping the optical field in all its dimensions [Fig. 24(g)]. This approach not only addresses dispersion issues in multimode optical fibers but can also be applied to other physical settings such as acoustics and electron optics.

### 3.5 Electric-Magnetic Toroidal Pulses

Flying donuts (FDs) are single-cycle pulses, distinguished by a donutlike configuration of electric and magnetic fields, which feature strong longitudinal field components parallel to the pulse propagation direction. Concurrently, toroidal light pulses with a vectorial structure of the electric-magnetic field were reported[130]. In 1996, Hellwarth and Nouchi theoretically identified a fundamentally different, non-transverse electromagnetic pulse with a toroidal topology. These pulses are propagating analogs of localized toroidal dipole excitations in the matter, exhibiting unique properties such as non-transversal, vectorial, space-time non-separability, and single-cycle nature. A numerical model has shown that conventional pulses can be transformed into FD using a specialized metamaterial converter designed to control both the spatial and spectral characteristics of the input pulse[244]. However, these same characteristics make them extremely challenging to realize and characterize experimentally. Consequently, the generation and observation of toroidal pulses remained elusive until the recent experimental observation of toroidal pulses in the optical and terahertz regions using metasurfaces with spatially tailored dispersion.

In 2022, Zdagkas *et al.* created such toroidal light pulses in the optical and terahertz regions using tailored nanostructured metasurfaces[130], as shown in Figs. 25(a) and 25(b). The electric field lines of TM components form deformed small circles of the torus, while the magnetic field circulates along the orthogonal large-circle coordinate, with the electric field decreasing inside the torus and vanishing at the central singularity; but in TE configuration, the electric and magnetic field structures are swapped. The generation scheme for optical toroidal light pulses, depicted in Fig. 25(c), involves a linear-to-radial polarization converter and a nanostructured metasurface. Figure 25(d) illustrates the generation of terahertz TM and TE toroidal light pulses using plasmonic metasurfaces. Figures 25(e) and 25(f) show iso-surfaces of the electric field of the generated toroidal light pulse at 60% of its maximum level, with red and blue colors representing the two half-cycles of the pulse. As expected, the electric field shows vanishing transverse components at the center of the pulse [Fig. 25(f)] but exhibits substantial longitudinal components [Fig. 25(g)].

Supertoroidal light pulses, as space-time nonseparable electromagnetic waves, exhibit unique topological properties such as skyrmionic configurations, fractal-like singularities, and energy backflow in free space. However, these properties do not survive during long propagation. Therefore, Shen *et al.* recently introduced non-diffracting supertoroidal pulses[245] [Figs. 25(h) and 25(i)], which feature propagation-robust skyrmionic and vortex field configurations that remain stable over arbitrary distances. Intriguingly, the energy flow structures of such a field resemble the von Kármán vortex street, a pattern of swirling vortices with staggered singularities found in fluid and gas dynamics, which can stably propagate forward [Figs. 25(j) and 25(k)]. In addition, a strongly longitudinally polarized toroidal pulse with a longitudinal component over 10 times greater than the transverse component was also proposed, offering robust, nondiffracting propagation, and potential for advanced light-matter interactions, far-field superresolution microscopy, and high-capacity wireless communication[246].

Despite advances in ultrafast optics and beam shaping, generating spatiotemporal light modes remains challenging due to the complex beam structures and the difficulty in shaping the entire pulse bandwidth. Although nanostructured metasurfaces have been used to create tailored THz pulses, conventional metasurfaces are static, with fixed functionalities, and cannot handle high pump intensities beyond their thermal damage threshold. This limits the potential for significantly improving THz conversion efficiencies. Recently, Jana *et al.* demonstrated THz toroidal pulse emission using quantum interference control[247], as illustrated in Fig. 26(a). In this setup, quantum control with two azimuthally polarized vector laser pulses induces a local ring current in GaAs, depicted in Fig. 26(b). This dynamic ring current density acts as a source for radiating an FD THz pulse, producing a pulse with a toroidal spatiotemporal structure shown in Figs. 26(c) and 26(d).

Extending prior methods for generating toroidal pulses to the microwave domain is challenging due to the need for larger apertures, collimating laser sources, and the scarcity of third-order nonlinear materials at microwave frequencies. Recently, a transient finite-aperture horn antenna emitter was designed to generate free-space microwave electromagnetic toroidal pulses[248]. The experimental configuration of a microwave toroidal pulse is illustrated in Fig. 27. Following this approach, the electromagnetic toroidal pulses evolve to closely resemble the Hellwarth-Nouchi pulse during propagation. Vectorial spatiotemporal mapping showed stable topological configurations over long distances. The emitter's high quality and efficiency also allowed for the experimental observation of free-space electromagnetic skyrmions. To date, electromagnetic toroidal vortices have primarily been classified into scalar photonic toroidal vortices[129] and vector toroidal pulse light[130]. Recently, Wang *et al.* introduced a novel electromagnetic toroidal vortex solution called hybrid toroidal vortex pulses (HTVPs), which uniquely combine both scalar and vector characteristics[249]. HTVPs exhibit the coexistence of transverse orbital angular momentum, electromagnetic vortex streets, and topological skyrmion textures.

### 3.6 Typical Topological Structures with STWPs

With advancements in beam shaping techniques, precise control over both temporal and spatial components of STWPs enables

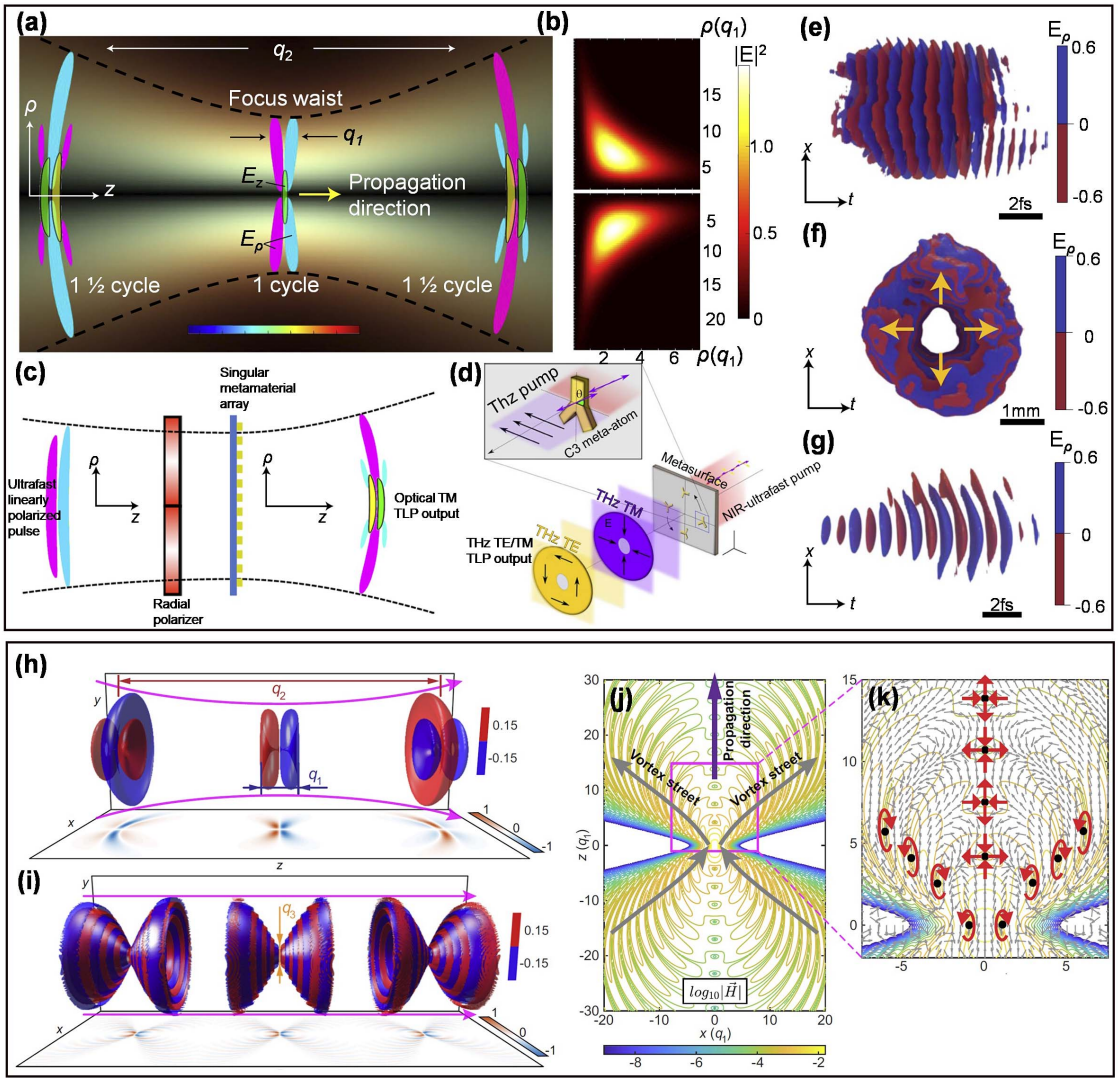


**Fig. 25** Electric-magnetic toroidal pulses. (a), (b) Spatiotemporal and spatio-spectral structure of the toroidal pulse[130]. (c) Schematic of the generation of an optical toroidal pulse. (d) Schematic of the generation of terahertz TM and TE toroidal pulses using plasmonic metasurfaces. (e) Side and (f) front views of the transverse electric field component of generated optical toroidal pulses. (g) Corresponding side view of the longitudinal component. (h) Propagation evolution of an elementary optical toroidal pulse[245]. (i) Propagation evolution of nondiffracting supertoroidal pulses. (j) Topological electromagnetic and energy flow structures of nondiffracting supertoroidal pulses with parameters $q_2 = 100$ and $q_3 = 1$ at $t = 0$. (k) A zoom-in of the magnetic field with the arrow plot showing the vector distribution, the black dots referring to the singularities, and surrounding red arrows marking the type of the vector singularities (vortex and saddle).

the realization of intricate optical topologies. These topologically complex transient electromagnetic fields facilitate novel light–matter interactions and offer enhanced degrees of freedom for information transmission. A notable example of such electromagnetic excitations is the space-time non-separable single-cycle pulses exhibiting toroidal topology, which represents exact solutions to Maxwell's equations first described by Hellwarth and Nouchi in 1996 and subsequently verified experimentally. Shen *et al.* expanded upon this concept by introducing a broader family of electromagnetic excitations termed supertoroidal electromagnetic pulses, where the Hellwarth-Nouchi pulse serves as the simplest member[250]. Supertoroidal pulses exhibit a skyrmionic structure in their electromagnetic fields, multiple singularities in Poynting vector mappings, and fractal-like energy backflow distributions. Figures 28(a) and 28(b) depict the propagation characteristics of toroidal and supertoroidal pulses in free space, respectively. Compared to fundamental toroidal pulses, supertoroidal pulses feature a more intricate singular vector field configuration. A particularly intriguing aspect of supertoroidal pulse topology involves the presence of skyrmionic quasiparticle configurations, observable in the magnetic field topology of these pulses.

Twisted strips, exemplified by Möbius strips, are 3D topological structures that illustrate how a surface can twist in space.

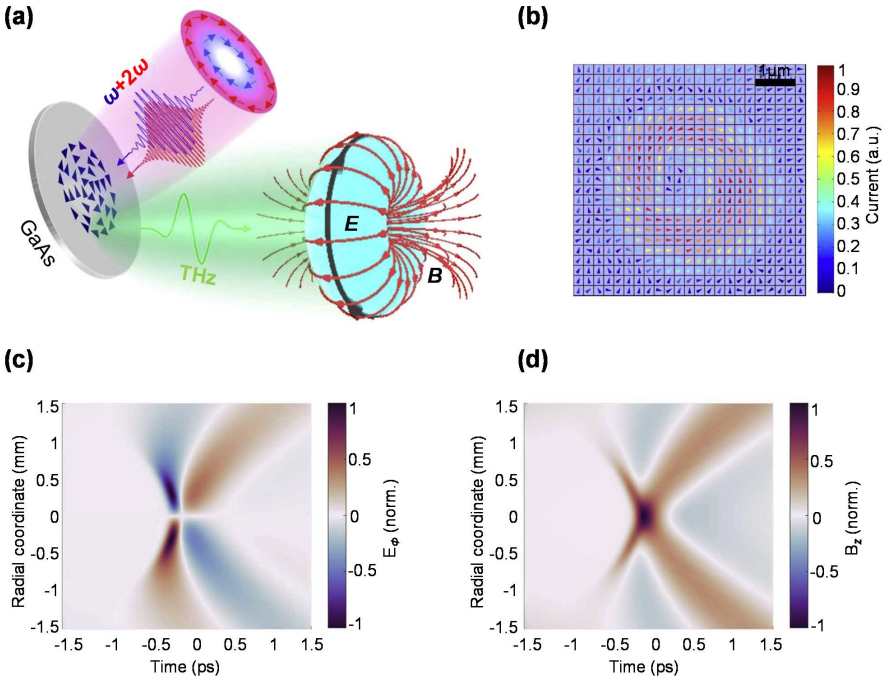


**Fig. 26** Dynamic ring current radiates FD terahertz pulse[247]. (a) Illustration of FD pulse generation: two azimuthally polarized vector pulses induce transient ring currents in GaAs. The radiation from these rapidly oscillating ring currents results in a single-cycle THz pulse with a toroidal topology and an FD pulse. (b) Spatial-vectorial distribution of ring current in GaAs. (c) Spatiotemporal structure of the radiated electric field from a dynamic ring current density source. (d) Magnetic field map of the emitted THz pulse.

This spatial configuration can be easily demonstrated using a rectangular strip of paper and finds practical applications in structures like liquid crystal defects and optical microcavities. Recently, Zhong *et al.* employed a spatiotemporal light field based on toroidal vortex structures to theoretically demonstrate how dynamic phase configurations can give rise to topological objects with controllable twist numbers[251]. This structured light field effectively utilizes the degrees of freedom within a high-dimensional parameter space, establishing connections between optical strips, optical knots, and optical hopfions, as shown in Figs. 28(c) and 28(d).

## 4 Characterization Techniques for STWPs

The characterization of ultrashort laser pulses has significantly advanced beyond the standard spatial and temporal diagnostics

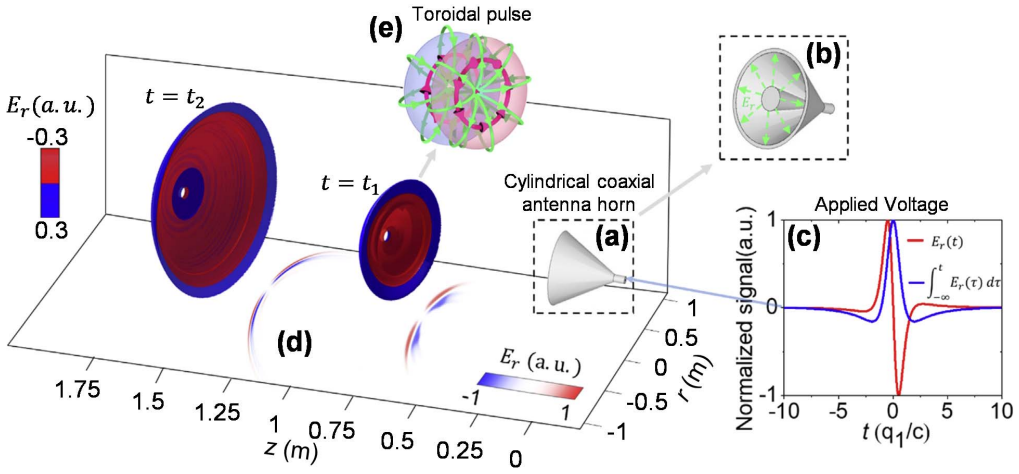


**Fig. 27** Experimental configuration for the generation of microwave toroidal pulses[248]. (a), (b) Cylindrical coaxial antenna horn. (c) Driving voltage applied to the antenna feed (blue line) and transient antenna output (red line). (d) Spatiotemporal evolution of the generated toroidal pulse. (e) A schematic of the electromagnetic configuration of such toroidal pulse.

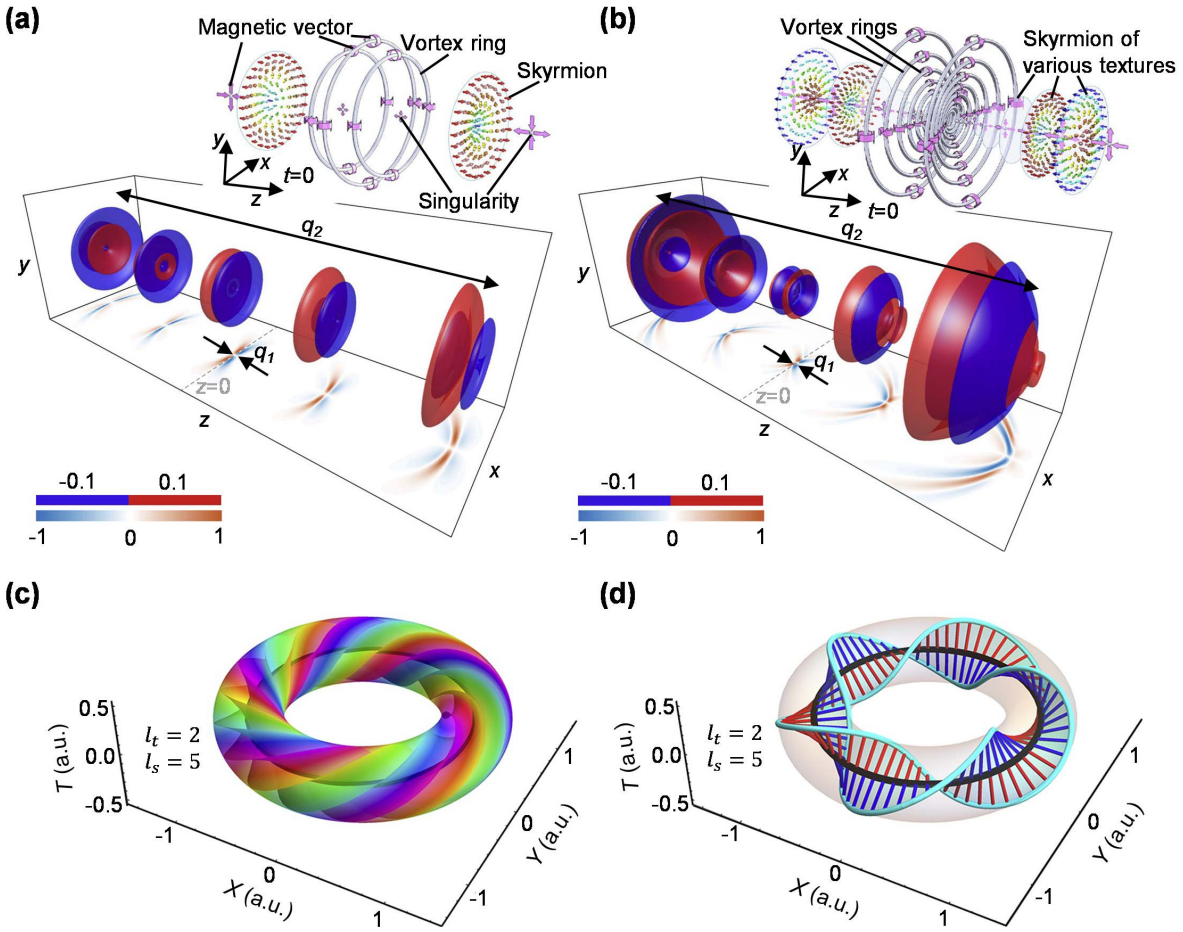


**Fig. 28** (a), (b) Electromagnetic skyrmionic structure embedded as the vectorial features of toroidal and supertoroidal pulses[250]. (c), (d) Hopfion structure established with the phase of a photonic toroidal vortex[251].

to now include sophisticated spatiotemporal measurement techniques. Accurately characterizing three-dimensional spatiotemporally coupled wavepackets (amplitude, phase, polarization, frequency chirp, etc.) is essential for understanding their dynamic behavior in space and time. The measurement method provides insights into complex wave interactions, aids in the development of advanced optical technologies, and supports the manipulation of light fields. In this section, we discuss common methods employed in recent studies for characterizing STWPs within the three-dimensional space-time domain.

### *4.1 Temporally Sliced Off-Axis Interference*

Given that STWPs are defined by their spatial distribution and temporal dynamics simultaneously, understanding their behavior requires a comprehensive analysis that captures how they propagate and interact in all three spatial dimensions and over time. Without precise 3D characterization, it is challenging to fully grasp their intricate properties, such as their shape evolution, movement, and interactions with other wavepackets or media. This detailed analysis is crucial for applications in advanced optics, quantum information processing, and material science, where accurate descriptions of wavepacket behavior are necessary for both theoretical studies and practical implementations. Recent advancements in ultrashort laser pulse characterization have been thoroughly reviewed in the excellent Refs. [252,253]. A common method in recent demonstrations is temporally sliced off-axis interferometry, also known as self-referenced interferometry, which relies solely on linear optics[254]. As illustrated in Fig. 29(a), the pulse being investigated (the object pulse) is divided into two beams to create a probe pulse. Ideally, the probe pulse is the transform-limited version of the original pulse. These two pulses are then combined at a slight angle $\varepsilon$ and detected by a CCD camera, forming a Mach-Zehnder-like scanning interferometry. The angle $\varepsilon$ is chosen to ensure that the interference fringes have a spatial period that is small but still resolvable by the CCD. The time delay between the probe and object pulses is adjusted using an optical delay line, and the CCD captures the time-integrated intensity $I_{\text{inter}}(\tau, x, y)$ as a function of the time delay $\tau$. When the duration of the probe pulse is shorter than that of the object pulse, the probe pulse can resolve finer details of the object pulse's temporal structure. This condition allows for higher temporal resolution in the measurement, enabling a more detailed investigation of the object pulse's dynamics. In this case, the interference pattern recorded by a camera is given by

$$I_{\text{inter}}(\tau,x,y) = I_o(x,y) + I_p(x,y) + 2\sqrt{\Delta t_p |u_o(\tau,x,y)|^2 I_p(x,y)} \times \cos[\delta(\tau,x,y) + k_0 y \sin\varepsilon], \quad (45)$$

where $I_o(x,y)$ and $I_p(x,y)$ are the time-integrated intensity distributions of the object and the probe pulse beam, respectively. $\tau$ is the time delay of the probe pulse with respect to the object pulse. $\varepsilon$ is the tilted angle between the object and the probe pulse beam. $\Delta t_p$ is the duration of the probe pulse. $\delta(\tau,x,y)$ is the transverse space-variant phase difference between the object pulse and the probe pulse at the temporal slice $\tau$. $u_o(\tau,x,y)$ is the complex field information of the wavepacket at each temporal slice, which reads

$$u_o(\tau,x,y) = A_c(\tau,x,y)/\sqrt{I_p(x,y)}, \tag{46}$$

where $A_c(\tau,x,y)$ is the coupling term in Eq. (45), which can be obtained by low-pass filtering out the positive first order of $I_{\text{inter}}(\tau,x,y) - I_o(x,y) - I_p(x,y)$ in the spatial frequency domain, as depicted in Figs. 29(b)–29(e). The time-dependent 2D amplitude and phase information can be obtained, as shown in Figs. 29(f) and 29(g). Finally, we can reconstruct the three-dimensional spatiotemporal wavepacket by stitching all temporal slices of $\tau_n$.

This method requires that the reference pulse width is significantly smaller than the measured pulse and that its spatiotemporal phase remains uniform and stable. To characterize the wavepacket, it is necessary to continuously scan across the time dimension, capturing a series of time-dependent interference patterns. To this end, an automated closed-loop characterization system was built to reconstruct the three-dimensional intensity and phase structures of STWP[255], as illustrated in Fig. 30. This closed-loop control program automates the data collection and reconstruction process using a LabVIEW script to simultaneously control the SLM, camera, and time delay, ensuring efficient and precise data acquisition.

### 4.2 Single-Frame Spatial-Spectral Interference

Despite its ability to fully reconstruct the 3D profile of STWPs, the temporally sliced interference method is limited to chirped, long-duration pulses due to its restricted temporal resolution. This is because scanning interferometry needs a much shorter sampling pulse than the STWP for high resolution, and a delay line is required, making it impractical for fast feedback characterization. Additionally, scanning interferometry does not measure the global temporal phase of the pulses, although it can still extract relative spatiotemporal phase singularities. In this context, Gui *et al.* demonstrated a single-shot characterization of STWP using a spatially resolved spectral interferometer (SRSI)[256], as illustrated in Fig. 31(a). The SRSI was created by aligning a time-delayed Gaussian, collimated reference pulsed beam collinearly with the object beam. This setup generates temporal interference, resulting in spectral interference fringes in the spatial-spectral domain through a grating and a cylindrical lens. Figure 31(b) displays a typically measured spatial-spectral fringe pattern. The spatial-spectral information of the object STOV pulse can be extracted via Fourier filtering, as shown in Figs. 31(c) and 31(d). Finally, the complex-amplitude information of the STWP can be recovered in the spatiotemporal domain through a 1D Fourier transformation from the temporal frequency to the time domain, as depicted in Figs. 31(e) and 31(f).

### 4.3 Nonlinear Transient Refractive Index Grating

In addition to the linear characterization methods mentioned, ultrashort laser pulses have also been extensively characterized through nonlinear effects. These nonlinear techniques leverage phenomena such as self-phase modulation, spectral broadening,

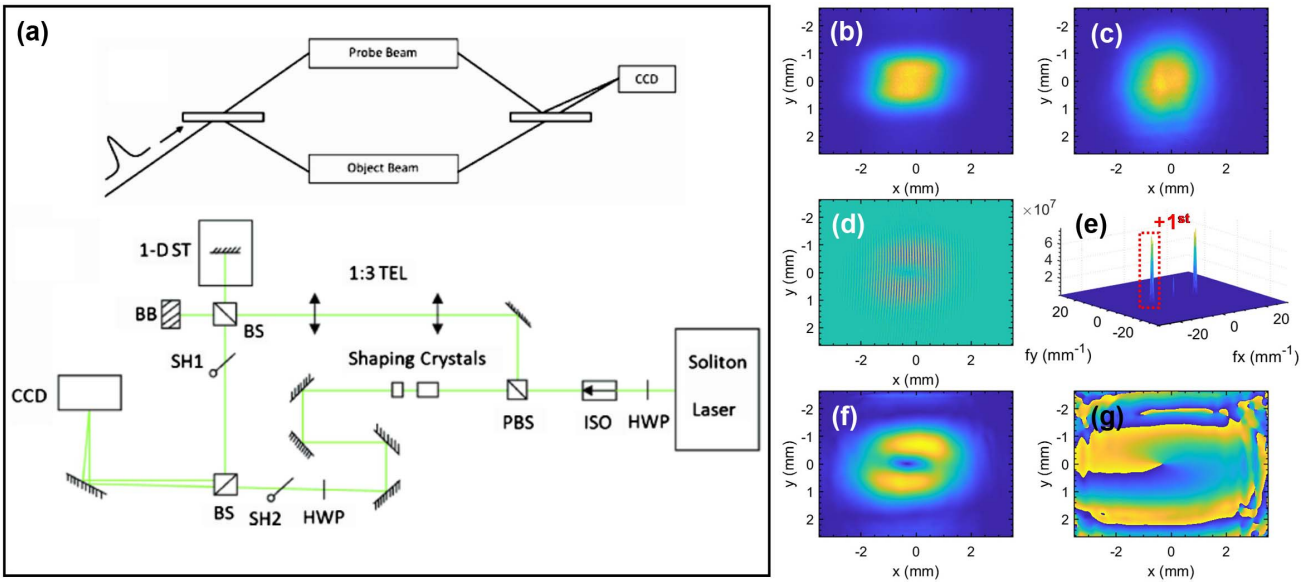


**Fig. 29** 3D laser pulse intensity diagnostic with temporally sliced off-axis interferometry[254]. (a) Concept and schematic implementation of the diagnostic method. (b) Experimental captured "object" beam $I_o(x,y)$ (take an STOV of $l = +1$ as an example). (c) Experimental captured "probe" beam $I_p(x,y)$, which has a Fourier transform limited duration of ~122 fs. (d) The interference fringe pattern of $I_{\text{inter}}(x,y) - I_p(x,y) - I_o(x,y)$. (e) The Fourier transformation of (d). (f), (g) Retrieved amplitude (f) and phase (g) distributions from the inverse Fourier transformation of the positive first order of (e).

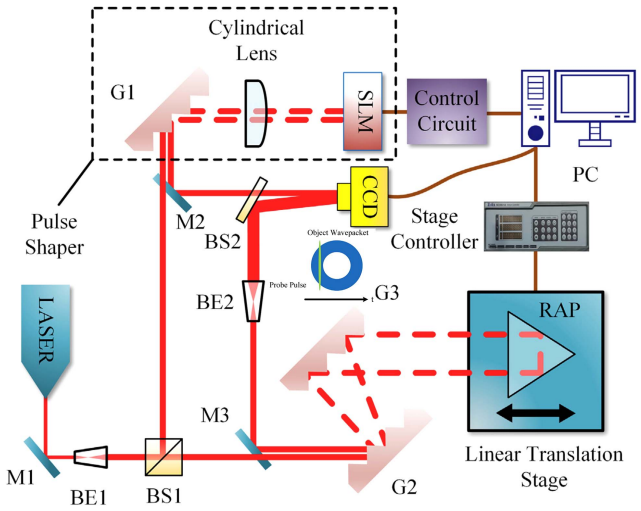


**Fig. 30** Automated closed-loop system for 3D characterization of STWPs (STOV as an example)[255].

and multiphoton absorption to extract detailed information about pulse properties. Prominent among these are autocorrelation[257], various forms of frequency-resolved optical gating (FROG)[258–262], and spectral phase interferometry for direct electric field reconstruction (SPIDER) and related methods[263–268]. Techniques such as STRIPEDFISH[269], d-scan[270], and single-shot supercontinuum spectral interferometry (SSSI)[271–273], as well as other spectral interferometry methods[274,275], have expanded the range of capabilities in pulse characterization.

Basic FROG and SPIDER methods are designed to extract space-independent temporal amplitude and phase information. However, more advanced techniques[268–270] have achieved the single-shot recovery of spatiotemporal phase and amplitude, though typically only for simpler pulse characteristics like pulse front tilt. STRIPED-FISH[269] and d-scan[270] rely on iterative algorithms to reconstruct pulse characteristics, but these algorithms have not yet been demonstrated to converge for pulses with complex structures or singularities. Similarly, SEA-SPIDER requires additional assumptions for determining the timing of spatial slices[268]. While SSSI does not provide the spatiotemporal phase information, it does recover the spatiotemporal pulse envelope.

In 2021, Hancock *et al.* introduced transient grating single-shot supercontinuum spectral interferometry (TG-SSSI), an enhanced version of single-shot supercontinuum spectral interferometry (SSSI) with additional phase measurement capabilities[276]. The schematic of this method is illustrated in Fig. 32. TG-SSSI employs four pulsed beams: the object pulse

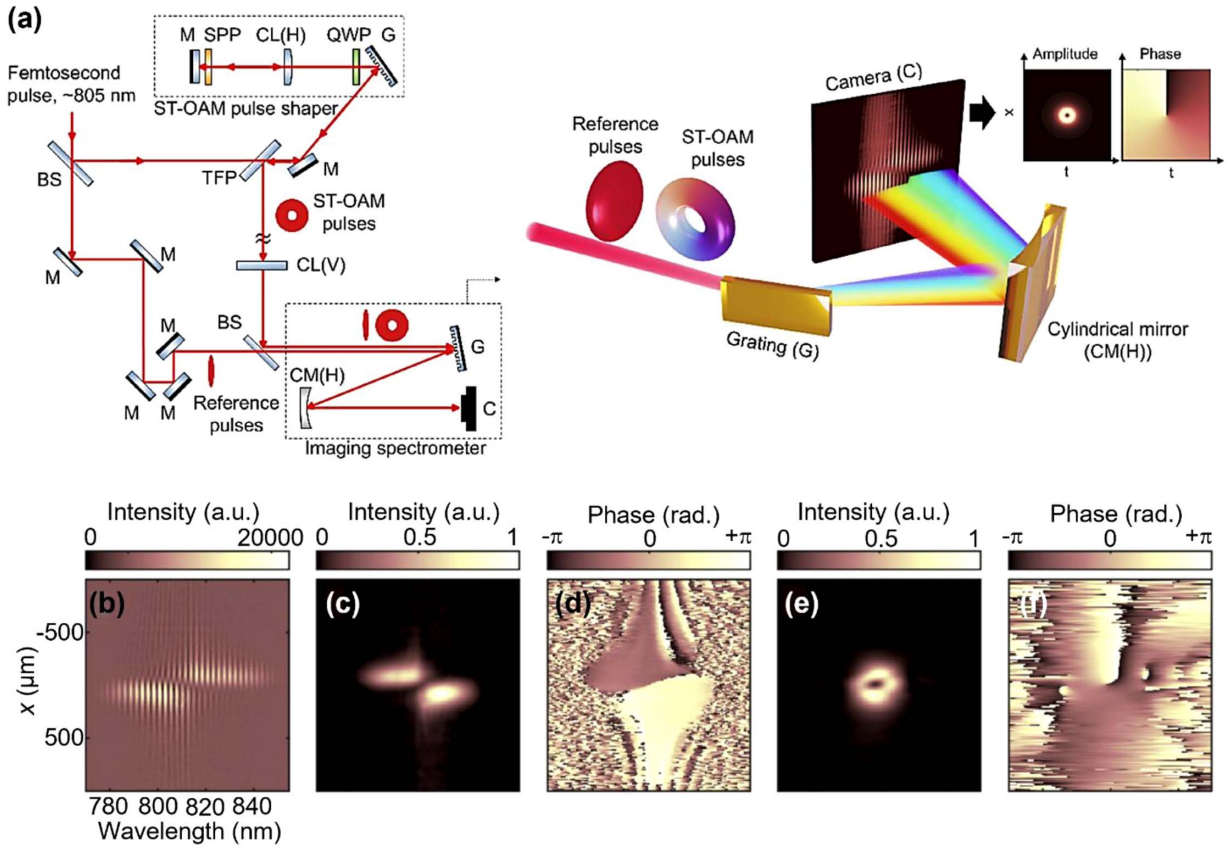


**Fig. 31** SRSI for STOV characterization[256]. (a) Experimental setup for the generation and characterization of ST-OAM light. STOV wavepackets are characterized by an SRSI, which includes collimated reference pulses and an imaging spectrometer. (b) Spectral interference fringe by SRSI. (c), (d) Reconstructed spatial-spectral amplitude and phase information by filtering fringe pattern of (b). (e), (f) Retrieved intensity and phase of an STOV by implementing 1D Fourier transformation (temporal frequency to time domain) of (c) and (d).

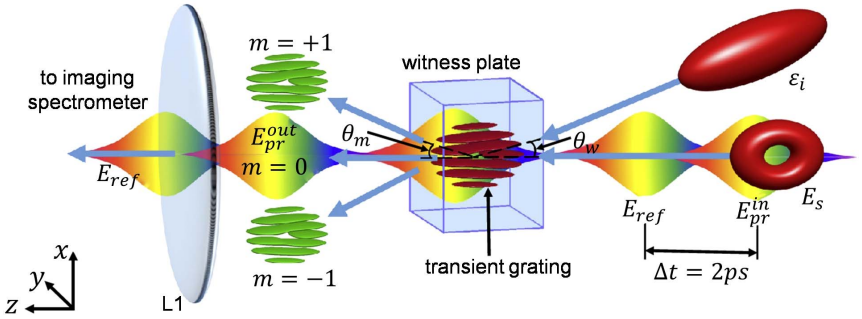


**Fig. 32** Schematic of transient-grating single-shot supercontinuum spectral interferometry for single-frame characterization of STWP[276]. The object pulse $E_s$ and the reference pulse $\varepsilon_i$ interfered with each other at an angle $\theta_w$ in a fused silica witness plate, forming a transient grating. Such a grating is recorded by a probe pulse $E_{\mathrm{pr}}$.

$E_s$, the reference pulse $E_{\mathrm{ref}}$, the probe pulse $E_{\mathrm{pr}}^{\mathrm{in}}$, and an additional reference pulse $\varepsilon_i$. In this setup, the object pulse $E_s$ interferes with the reference pulse $\varepsilon_i$ at an angle within a witness plate, producing a set of interference fringes (referred to as a transient grating) that are recorded by the witness plate. The resulting interference pattern is given by $I_{s\varepsilon} = |E_s|^2 + |\varepsilon_i|^2 + E_s\varepsilon_i^* + E_s^*\varepsilon_i$. The probe pulse $E_{\mathrm{pr}}^{\mathrm{in}}$ interacts nonlinearly with this transient grating, generating an output field $E_{\mathrm{pr}}^{\mathrm{out}} \propto \chi^{(3)} I_{s\varepsilon} E_{\mathrm{pr}}^{\mathrm{in}}$. The amplitude and phase information of the object pulse $E_s$ are then encoded in the output field $E_{\mathrm{pr}}^{\mathrm{out}}$. While TG-SSSI offers the advantage of single-shot measurement for both the amplitude and phase of an ultrashort pulse, its practical application is limited by the requirement for high pulse energy, with typical pulse energies exceeding 3 μJ to effectively excite the third-order nonlinear process.

## 5 Applications of STWPs

STWPs, such as STOVs with transverse OAM, diffraction-free light sheets, and vectorial toroidal pulses, are pivotal in modern physics and engineering. They describe wave profiles in the 3D space-time domain and exhibit unique propagation and interaction properties. Their interaction with matter promises novel effects, leading to rapid investigations in fundamental physics and photonic engineering. Researchers are exploring STWPs to enhance light-matter interaction understanding and develop advanced technologies, including ultrafast interactions, innovative communication systems, optical information processing, and new quantum rules.

### 5.1 Light–Matter Interaction and Optical Trapping

Light, possessing both linear and angular momentum, plays a crucial role in particle manipulation. Optical angular momentum itself manifests in many forms. The first distinction is drawn between OAM and spin angular momentum. Optical trapping refers to the interaction between light and matter that manipulates micro-objects through the transfer of such momentum. The conservation of these momenta underpins the operation of optical microtools, such as tweezers, traps, and spanners. Vortex beams, characterized by their spatial helicoidal phase and longitudinal OAM, have emerged as a powerful tool for controlling particle rotation. While previous studies have primarily focused on longitudinal OAM transfer along the beam's propagation axis, limiting particle motion to axial rotation, recent advancements have explored the potential for exploiting transverse OAM to induce complex, three-dimensional particle manipulation. In 2022, Stilgoe *et al.* reported the observation and measurement of transverse angular momentum transfer to birefringent vaterite particles, several wavelengths in size, trapped using optical tweezers in a transmission optical system[277], as illustrated in Fig. 33(a). A custom-designed beam, shown propagating from the bottom of the page, interacts with the larger birefringent particle, inducing spinning and rotation about the axis indicated by the curved arrow. The authors utilized Stokes parameters and cross-polarization measurement techniques to characterize the angular momentum transfer to the particles. Figure 33(b) shows two sequences of frames depicting a naturally occurring small particle moving through the focal plane. The position and brightness of the particle reflect its three-dimensional rotational state, driven by the transverse momentum. The transverse OAM originates from the helical phase in the $x$ or $y$–$z$ plane. To achieve this, Hu *et al.* generated transverse OAM within the interference field of two parallel, counter-propagating, linearly polarized focused beams, those $y$-axially separated by a distance $2\delta_y$, synthesizing an array of identical handedness vortices carrying intrinsic transverse OAM, as shown in Fig. 33(c)[278]. When $\delta_y > 0$, the transverse OAM is generated at the optical antinode, where the nanorod is trapped. The transverse OAM of the beam is transferred to the nanorod, driving it to rotate in the $y$–$z$ plane [Fig. 33(d) top]. When $\delta_y = 0$, there is no rotation, and the nanorod is harmonically confined in all five degrees of freedom [Fig. 33(d) bottom]. Additionally, using the complex spatiotemporal sculpting techniques described, ultrafast pulses with time-varying and transiently switchable transverse OAM can be generated[214]. These tailored STWP bursts have the potential to enable novel applications in ultrafast light-matter interactions, including the study of the effects of chirality on matter[279,280].

### 5.2 STWPs as Information Carriers for Data Encoding and Decoding

Optical communication systems depend on the encoding, transmission, routing, and decoding of optical pulses to transmit digital information. In these systems, optical pulses are modulated to represent binary data, enabling high-speed and efficient communication over optical networks. To enhance the bandwidth and capacity of optical communication systems, there is a

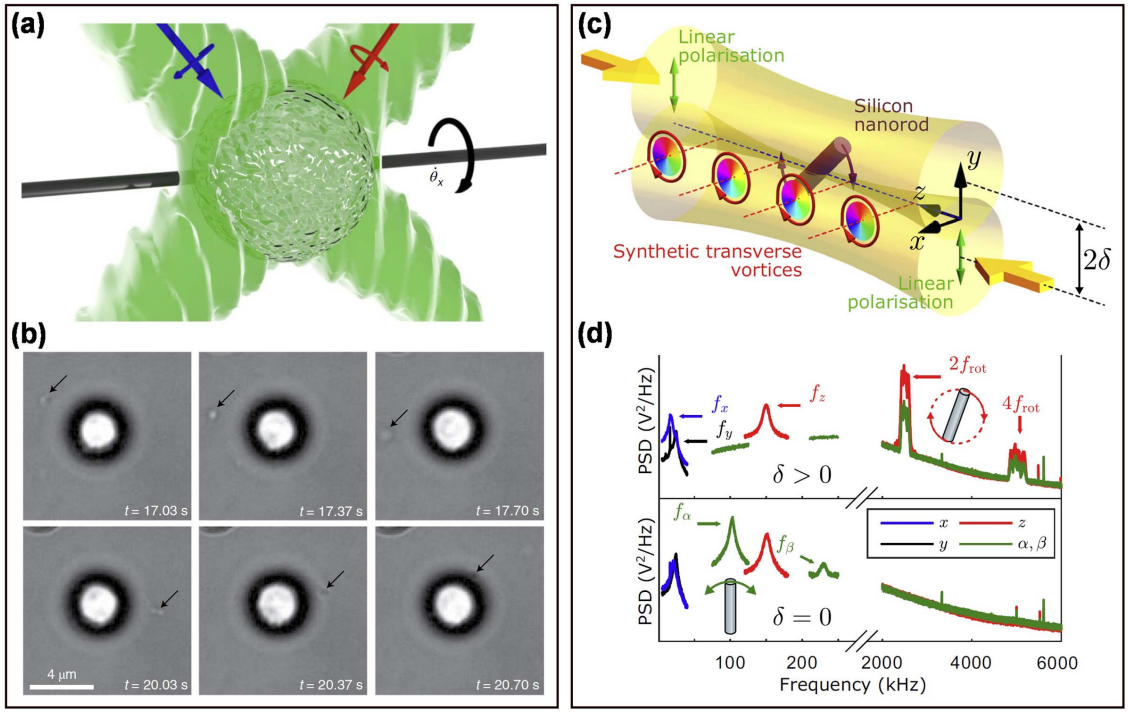


**Fig. 33** Optical trapping using transverse OAM. (a) Rotation of birefringent microparticles with transverse OAM caused by the superposition of two orthogonal circularly polarized beams (red and blue arrows)[277]. (b) Small particles driven around a larger vaterite particle undergoing transverse spinning. (c) Generation of transverse OAM beam; when two focused, counter-propagating, linearly polarized Gaussian beams are separated along the polarization axis, an array of optical vortices carrying transverse angular momentum is generated, causing a suspended silicon nanorod to experience torque and rotate in the $y$–$z$ plane[278]. (d) Power spectral density (PSD) of the nanorod motion when driven to rotate at a frequency $f_{\mathrm{rot}}$ by transverse OAM (top) and without transverse OAM (bottom).

growing focus on incorporating multi-dimensional information into the coding and decoding processes. These advanced approaches leverage various dimensions of optical signals, including intensity, wavelength, phase, spatial modes, polarization, and angular momentum, to encode information simultaneously. By utilizing these additional dimensions, optical communication can achieve higher data rates and greater capacity. While optical communications can be conducted through both free space and optical fibers, there is a predominant focus on fiber-optic solutions. However, transmitting STWPs, such as STOVs, through optical fibers or waveguides presents significant challenges. These difficulties arise from the complex spatiotemporal coupling within the STWP and the modal and spectral dispersion introduced by the materials. Very recently, the first experimental demonstration of STOV pulse propagation through a few-mode optical fiber has been reported by Cao *et al.*[281]. Figure 34(a) shows a schematic of the experimental setup used to generate, transmit, and measure an STOV pulse through a 1-m-long commercial few-mode optical fiber. Figure 34(b) displays an example of an output STOV with a topological charge $l = +1$ after propagating through the fiber. In this instance, the input STOV pulse was pre-chirped to a GDD of $+0.36$ ps$^2$ before coupling into the fiber. The results confirm that the phase singularity of the STOV pulse is preserved after traveling 1 m through the few-mode fiber. However, to transmit higher-order STOV pulses, the fiber must support additional guiding modes and the STOV pulse may need precise spatial engineering before coupling into the fiber. Recently, Huang *et al.* have demonstrated that long STOV strings, generated by phase manipulation of input pulses, offer significant advancements in optical communication by enabling high-bit coding and decoding with minimal STOV modes[282]. The generation of STOV strings and the detection of their topological charges and positions within the string can be viewed as coding and decoding processes, respectively, as illustrated in Fig. 34(c). Unlike conventional vortex beams that require multiple OAM states for $m$-ary coding, STOV strings utilize the positions of STOVs as an additional dimension, significantly increasing coding efficiency and potential data transmission capacity. This novel approach, known as multistate transverse OAM shift keying (MS-TOAMSK), paves the way for innovative applications in fields such as optical computing, offering a more powerful and flexible platform compared to traditional OAM-based communication systems. Overall, integrating multiple controllable dimensions into STWPs enhances data efficiency and throughput, thereby advancing the development of high-capacity and high-speed optical networks.

### *5.3 Optical Analog Computation with STWPs*

Optical analog computation has the potential to significantly accelerate massively parallel operations while avoiding the costly analog-to-digital conversions required by electronic systems.

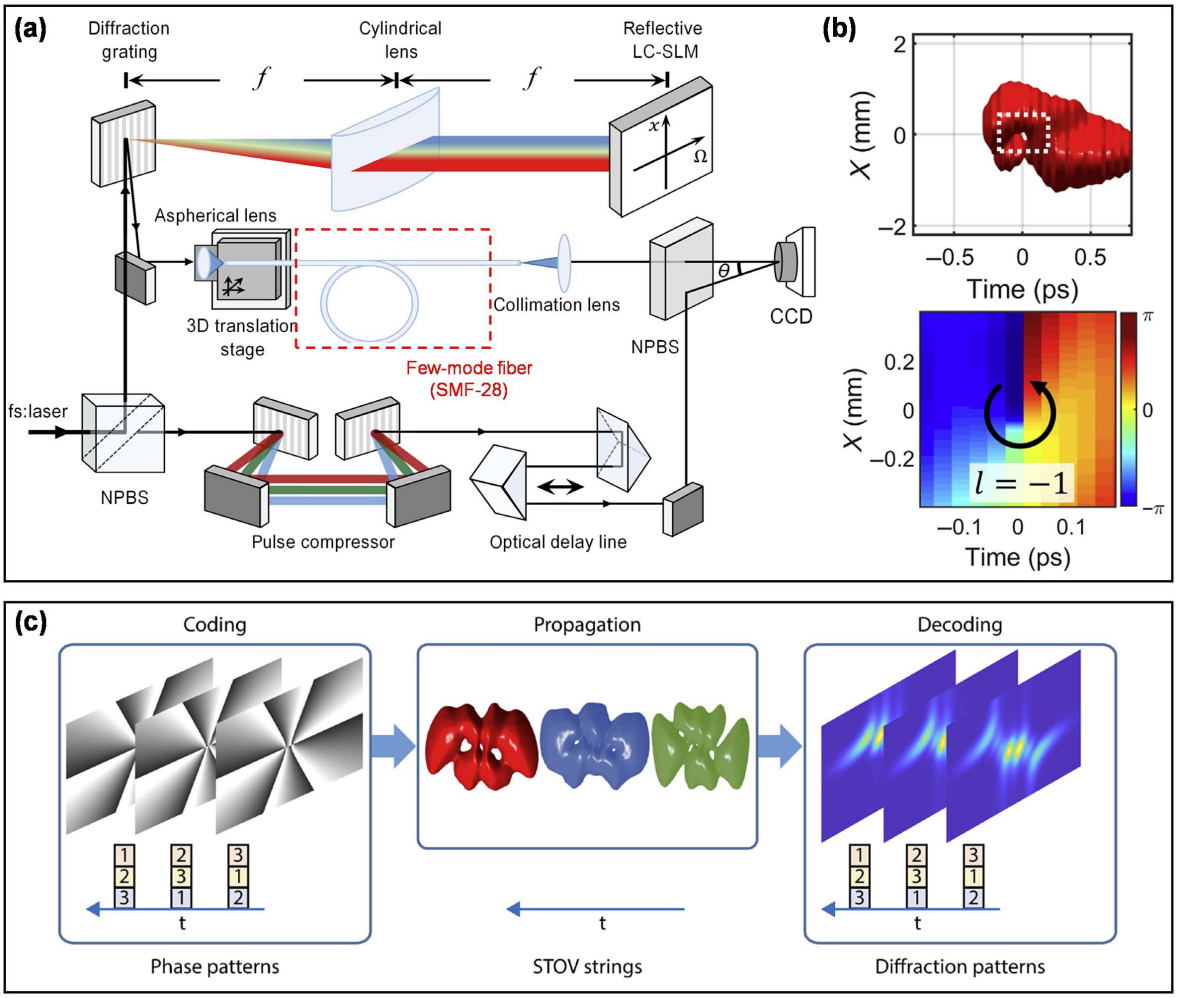


**Fig. 34** (a) Experimental demonstration of transmitting STOVs through few-mode optical fiber[281]. An STOV pulse from the 2D pulse shaper is coupled into a few-mode fiber (SMF-28) by a high-numerical-aperture aspherical lens mounted on a 3D translation stage. (b) Measured intensity and phase results for positively chirped STOV pulse transmitted by few-mode optical fiber; the topological charge is −1. (c) Scheme of data transmission based on STOV strings[282]. The three colored wavepackets shown in the middle represent three 3-STOV strings with topological charge arrangements of 123, 231, and 312.

It also offers greater energy efficiency compared to electronic counterparts. Photonic structures designed with spatial dispersion and 2D spatial filters are capable of performing analog computations. For instance, these devices can achieve spatial differentiation, enhancing edge contrast in imaging applications for both amplitude and phase objects. Recently, Ruan *et al.* have reported an optical differentiator in both spatial and temporal dimensions by designing a photonics structure that generates STOVs. Their spatiotemporal differentiator consists of a 1D periodic grating with broken spatial mirror symmetry[185], as illustrated in Fig. 11(b). Figure 35(a) (left) displays an original complex image of the "Zhejiang University" logo, representing both amplitude and phase in the spatiotemporal domain before it passes through the differentiator. After the pulse has traversed the spatiotemporal differentiator, the resulting STWP exhibits edge enhancement patterns in the space-time plane, as shown on the right side of Fig. 35(a). The spatiotemporal differentiator for single-shot ultrafast wavepackets has been experimentally verified in Ref. [283] using a nonlocal meta-grating. This meta-grating, with broken mirror symmetry, exhibits a nonlocal coherent response, where the transfer function depends linearly on both the spatial wavevector and temporal frequency. Figure 35(b) depicts the experimental setup for demonstrating this spatiotemporal differentiator, where a meta-lens is employed to generate a tilted-pulse front wavepacket. Figure 35(c) presents the results of directly measured wavepackets after passing through the meta-lens without the meta-grating, revealing a tilted wavefront in both space and time. After the wavepacket passes through the meta-grating, it exhibits a central zero-intensity in the spatiotemporal profiles, corresponding to the regions of slowest spatiotemporal variation in the incident pulses, as shown in Fig. 35(d). The differentiation resolution can be improved by using meta-gratings with broader linear ranges in both the temporal and spatial frequency domains.

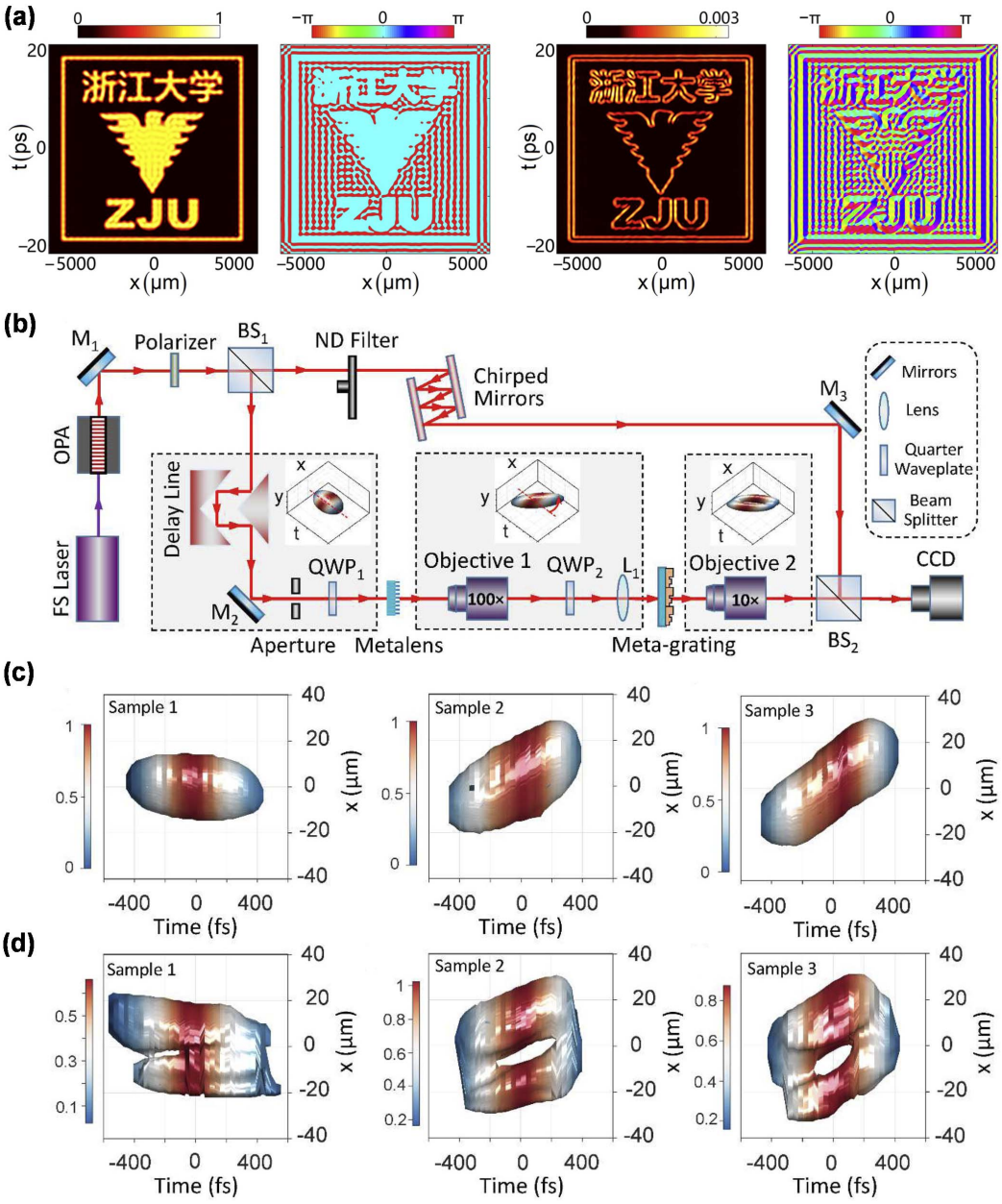


**Fig. 35** Spatiotemporal differentiation metasurfaces. (a) The spatiotemporal amplitude and phase of the "Zhejiang University" logo pattern and the corresponding amplitude and phase after passing through a meta-grating with breaking mirror symmetry[185]. (b) Spatiotemporal differentiator for optical nonlocal meta-grating computing[283]. Experimental setup consists of three parts: (1) a delay line for pulse characterization; (2) dispersion-engineered metalens for tilting the pulse; and (3) a meta-grating for spatiotemporal differentiation. (c) Retrieved iso-intensity profiles of incident pulses generated by different dispersion-engineered metalenses (without spatiotemporal differentiator) with various tilted angles. (d) Retrieved iso-intensity profiles of pulses passing through the spatiotemporal differentiation meta-grating. The intensity profiles of these retrieved pulses are normalized to the peak intensity of their individual incident pulses.

### *5.4 STWPs-Driven Superintense Field*

Optical vortices were initially limited to weak laser fields due to the low damage thresholds of their transmission components, which could not withstand high-power lasers. However, with advancements in superintense ultrafast laser technology, laser intensities have surpassed $10^{22}$ W/cm$^2$, enabling interactions with laser-driven plasmas and opening up new possibilities for relativistic particle interactions, including applications such as particle acceleration, X-ray and $\gamma$-ray generation, and vortex harmonics generation. Likewise, it is anticipated that extending vortex lights from nonrelativistic to relativistic regimes will enable novel multidimensional manipulations within relativistic particle interactions. Recently, Sun *et al.* proposed a relativistic

STOV pulse using reflecting optical elements to realize the modulation and acceleration of an isolated attosecond (~600 as) electron sheet in 3D particle-in-cell (PIC) numerical modeling[284]. In 3D PIC simulations, relativistic STOV pulses produced by a pulse shaper configuration are employed to drive a nanowire target, resulting in the generation of a relativistic isolated attosecond electron sheet (RIAES). This process is schematically illustrated in Fig. 36(a), where the insert displays the generated STOV electric fields. Figures 36(b)–36(e) illustrate the acceleration of an attosecond electron sheet driven by an intense STOV pulse. It shows that at $t = 16$ T, electrons are dispersed by the leading edge of the STOV pulse [Figs. 36(b) and 36(c)]. By $t = 60$ T, a selected electron sheet is concentrated within the intensity singularity of the STOV pulse, guided by the hollow ponderomotive force around the $z$-axis [Figs. 36(d) and 36(e)]. This suggests that the spatiotemporal phase singularity in the STOV pulse offers an additional degree of spatiotemporal freedom, enabling the generation of a single-electron sheet. Additionally, a recent study demonstrated the generation of well-collimated $\gamma$-photons and photon pairs with extrinsic transverse OAM via the head-on collision of an intense STOV pulse with a high-energy electron beam[285].

Although the transfer of transverse OAM in SHG and HHG processes driven by an STOV pulse has been investigated, demonstrating the conservation of transverse OAM, the transfer of transverse OAM in other strong-field processes remains unclear. In this context, Chen *et al.* recently investigated atomic photoionization driven by STOV pulses[286]. They focused on a scenario where an H atom is ionized by an STOV pulse with a central wavelength of 1600 nm, assisted by an XUV pulse. By precisely adjusting the spatial position and time delay of the XUV pulse relative to the STOV, they achieved control over

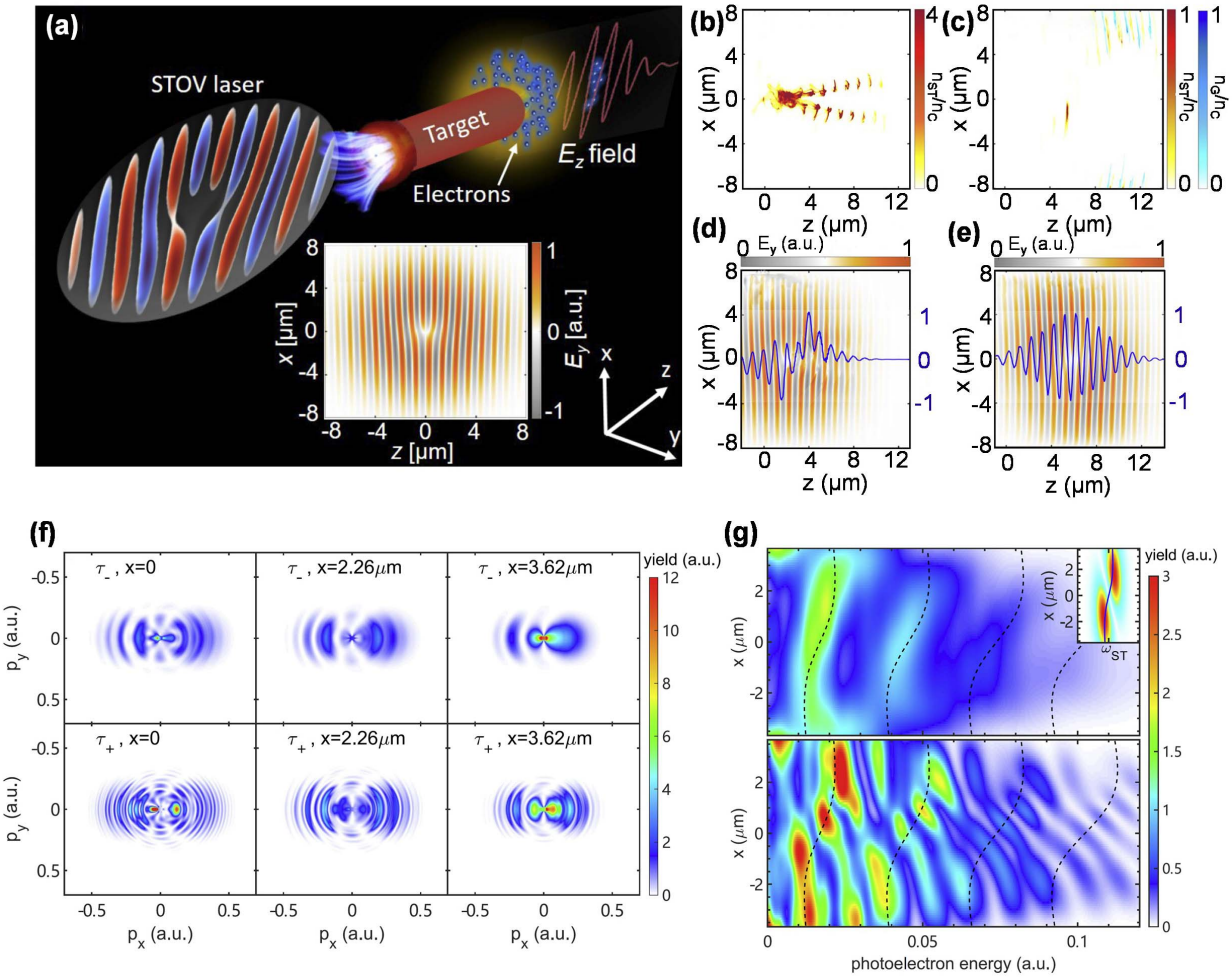


**Fig. 36** (a) Generation of isolated attosecond electron sheet via relativistic spatiotemporal optical manipulation. The STOV pulse is incident from the left and radiates onto the nanowire target[284]. The electrons can be initially dragged out from the target and further phase-locked and accelerated by the longitudinal electric field ($E_z$) inside the STOV laser. (b)–(e) Electron density driven by an STOV pulse at (b), (c) $t = 16$ T and (d), (e) $t = 60$ T. (f), (g) Atomic photoionization by STOV pulses. (f) Calculated photoelectron momentum distributions (PMDs) for the photoionization of an H atom by an STOV pulse assisted by an XUV pulse[286]. (g) Calculated spatially resolved photoelectron energy spectra for time delays (top) $\tau_-$ and (bottom) $\tau_+$ of the XUV pulse obtained by the 3D-TDSE.

strong field ionization in both space and time. The resulting photoelectron momentum distribution (PMD) reflected the spatial chirp of the STOV pulse's electric field, as depicted in Fig. 36(f). Additionally, the spatially resolved photoelectron energy spectra, influenced by the spatiotemporal singularity, fully characterized the OAM states, showing distinct interference patterns that depend on the XUV pulse's spatial location [Fig. 36(g)]. Besides, spatiotemporal high-harmonic generation in the relativistic regime using an intense STOV beam on a plasma target has also been demonstrated, where the plasma surface acts as a spatiotemporally coupled relativistic oscillating mirror[287]. The harmonics inherit the spatiotemporal features, with transverse OAM scaling with harmonic order, achieving relativistic-level intensities due to plasma's ultrahigh damage threshold. Strong field physics driven by STWPs has been extensively studied numerically, showcasing the unique advantages of these wavepackets. However, these findings are still in their infancy and require further experimental verification.

### 5.5 Metrology and Sensing Using STWPs

STWPs' spatial and temporal properties are intertwined in a way that their behavior is not separable into independent spatial and temporal components. In simpler terms, these wavepackets have their spatial and temporal characteristics linked such that changes in one domain (spatial or temporal) affect the other, and exhibit behaviors where their spatial shape and temporal dynamics are intrinsically linked, leading to unique propagation characteristics and applications. In general, generating an STWP involves trading one spatial dimension in 2D space to operate in the time or frequency domain, resulting in entanglement between one spatial and one temporal dimension. For sensing applications, the 2D spatial extent of the field is adjusted to sample the external environment adequately (e.g., ambient or physical materials). However, this increases sensitivity to parasitic fluctuations and vibrations. A possible solution is to reduce the transverse dimensionality of the field from 2D to 1D, balancing sensitivity to the analyte with minimized phase fluctuations. Space-time light sheets represent a distinctive category of 1D fields that hold promise for further investigation. These light sheets are notable for their resistance to diffraction, dispersion, and speckle formation[288]. Their propagation invariance arises from the classical entanglement of the spatial and temporal frequencies involved[289]. In 2023, Diouf *et al.* examined the phase stability of space-time light sheets using Michelson interferometry, comparing them with standard Gaussian beam illumination[290]. Given that interferometers are sensitive to path-length variations, the optical intensity at the interferometer output varies over time. Figure 37(a) illustrates the experimental setup, where the space-time light sheet is coupled into a Michelson interferometer. Figure 37(b) displays the measured interference stability: space-time light sheet illumination achieves over 23% greater phase stability compared to the Gaussian light sheet, and approximately 80% more stability than Gaussian beam illumination. Both space-time light sheets and Gaussian light sheets demonstrate significantly higher phase stability compared to Gaussian beams. However, space-time light sheets offer an additional advantage: they are resistant to speckle generation, even when a thin diffuser is introduced into the interferometer. Besides, three-dimensional toroidal electromagnetic pulses, characterized by sophisticated topological and non-separable structures, have also been explored for 3D positioning applications. Wang *et al.* demonstrated free-space microwave 3D positioning by leveraging the space-time nonseparability and skyrmion topology of toroidal pulses[291]. This approach allows for super-resolution 3D spatial positioning with centimeter-level accuracy using a single emitting antenna. Each point within the primary distribution region of the toroidal field possesses unique time/frequency-polarization information, which can be distinctly characterized by its time-polarization or frequency-polarization state, as illustrated in Fig. 37(c). By measuring this time/frequency-polarization state at any given spatial point and cross-referencing it with a positioning information database, accurate spatial coordinates for target positioning can be determined, as shown in Fig. 37(d).

## 6 Further Prospects and Conclusions

Despite rapid advancements in spatiotemporal sculpturing of light in recent years, this field remains emerging with much still to explore. Below, we discuss several potential future directions: some are aspirations, others are inspired by past developments in spatially structured light, and some are speculative.

### 6.1 Ultracompact Synthesis of STWPs

The current mainstream method for generating and controlling STWPs involves using ultrafast pulse shapers and spatial light modulators. These systems typically utilize a diffraction grating to spatially resolve the initial pulse spectrum, allowing for the modulation of each wavelength. However, these approaches depend on bulky optical setups that require precise alignment and are less efficient. Consequently, advancing compact optical systems and elements, such as diffractive optical elements, metasurfaces, and nano-photonics devices, could significantly enhance the development of spatiotemporally structured STWPs.

Chirped Bragg volume gratings (CBGs) provide an alternative method for spatially resolving the spectrum[292,293]. Recently, Yessenov and Mhibik *et al.* proposed a compact system to synthesize space-time wavepackets, in which a chirped volume Bragg grating (c-CBG) that is rotated by 45° with respect to the plane-parallel device facets is employed[294,295], as shown in Figs. 38(a)–38(d). Such a device has several more salutary features than conventional grating-based setups: (1) The input beam is incident normally on one facet, and the spectrally resolved field exits through a different facet, also normally; (2) The emerging spectrum is collimated without the need for a lens and does not require additional free-space propagation; (3) The device's length and width are decoupled, allowing its cross-section to be a narrow rectangle rather than a large square; and (4) A pair of r-CBGs can be cascaded to first resolve and then recombine the spectrum, thereby reconstituting the input pulse at the output. Following this device, the diffraction efficiency of an r-CBG is kept at 80% with the total efficiency of the setup reaching 60%.

Although three-dimensional extension of STWPs using cascaded spatial modulation systems like MPLC devices is possible, it is challenging to synthesize 3D STWPs with this method, as it requires an extra spatial dimension to spread the temporal spectrum. Nano-photonics is poised to play a crucial role in the field of STWPs and spatiotemporally structured optical fields. A key challenge is designing nanophotonic systems capable of generating an STWP from a generic pulsed beam. In 2021, Guo *et al.* proposed generating 3D space–time

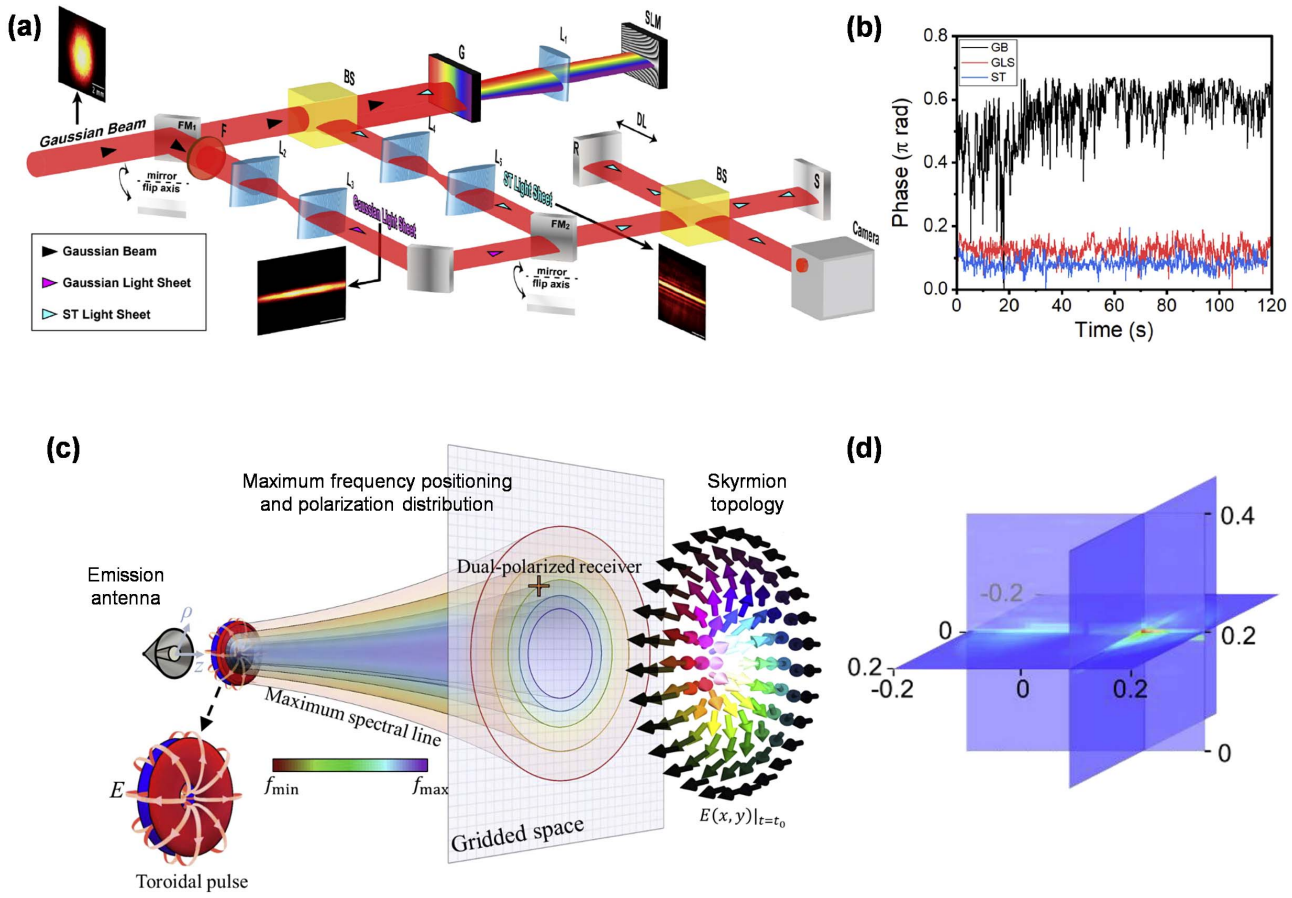


**Fig. 37** (a) Experimental setup for the generation of the space–time light sheet and interferometric phase stability analysis[290]. The generated space–time light sheet is coupled into a Michelson interferometry. (b) Measured interferometric phase recorded over 2 min for the Gaussian beam (black), GLS (red), and ST light sheet (blue). (c) Schematic diagram of 3D positioning method based on toroidal pulses[291]. (d) Computed 3D positioning pseudo-spectrum based on toroidal pulses.

light bullets propagating in free space using a single passive nonlocal optical surface[296]. This approach utilizes nonlocal nano-photonics to achieve space–time coupling without relying on bulky pulse-shaping and spatial modulation techniques [Fig. 38(e)]. Recently, Cheng *et al.* introduced an asymmetric grating structure for compactly generating optical toroidal vortices[297]. Figure 38(f) illustrates the device schematic, where a cylindrical vector wavepacket is transformed into a transmitted 3D toroidal vortex pulse. A recent experiment demonstrated a metasurface capable of beam steering at picosecond timescales[298]. This metasurface integrated the functions of a traditional grating and lens, allowing it to spatially resolve the spectrum of an incident laser frequency comb and focus the comb wavelengths at a specific plane, as shown in Fig. 38(g). In the far field, this setup generates a tilted pulse front with a differentiable angular dispersion. Observations at a fixed axial plane reveal the tilted pulse front as a pulsed spot moving across the plane, which is interpreted as beam steering.

### *6.2 Space–Time Mode Sorting and Quantum Control*

Modal state sorting involves distinguishing and organizing optical beams based on their OAM, where beams are classified by their helicoidal phase structure, often represented by an integer quantum number $l$. This process typically includes identifying the OAM values, separating beams using optical devices, and sorting them into different categories or channels. OAM sorting is crucial for applications such as increasing the capacity of optical communication systems, enhancing imaging techniques, and advancing quantum computing by utilizing the unique properties of different OAM modes. STWPs offer more controllable degrees of freedom in the space-time domain, such as transverse OAM, which can enhance information transmission capabilities. The ultrashort duration of STWPs poses a challenge for detecting and sorting their OAM, as the rapid temporal variations can complicate accurate measurement and classification. Recognizing and spatially sorting their modal states can significantly benefit applications in optical communication by enabling more efficient data encoding, improved channel multiplexing, and advanced information processing. Now, the mode conversion between STLG and STHG wavepackets can be used to recognize radial and azimuthal quantum numbers[134] [Fig. 39(a)]. Moreover, to achieve electric readout of OAM modes, an orbital photogalvanic effect has been proposed to directly detect OAM modes by using a 2D Weyl semimetal material[299] [Fig. 39(b)]. These effects will further advance

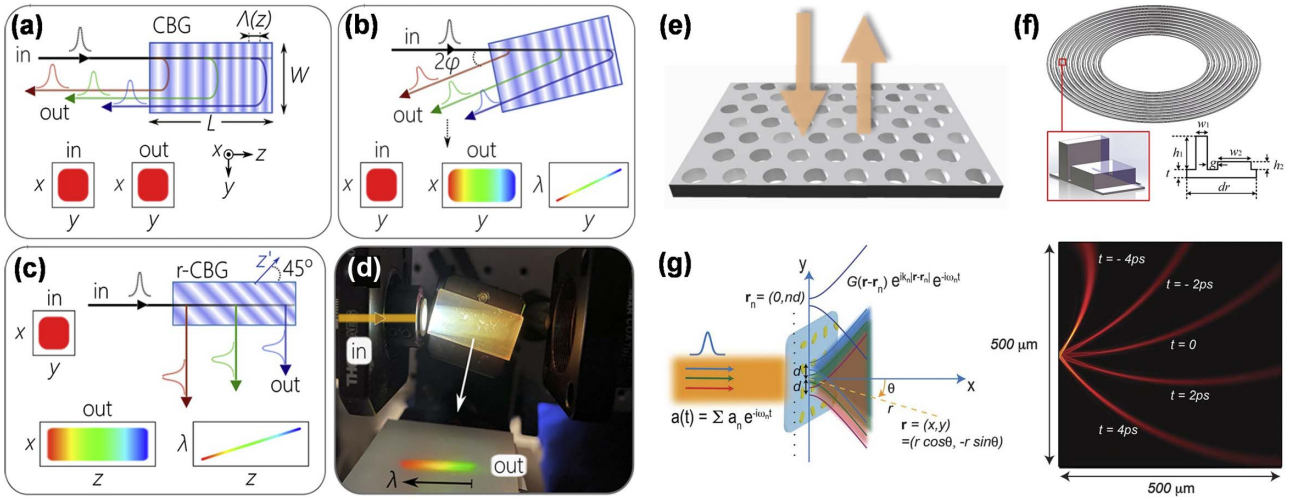


**Fig. 38** (a)–(d) Concept of chirped Bragg volume gratings (r-CBGs) with various configurations[294,295]. (a) Pulse normally incident on a CBG is temporally stretched but not spectrally resolved. (b) Pulse obliquely incident on a CBG is spectrally resolved. (c) Spectrally resolving a pulse normally incident on an r-CBG. (d) The spectrum spreading of white light by an r-CBG. (e) A passive nonlocal optical surface for the generation of 3D space–time light bullets[296]. (f) An asymmetric grating structure for the generation of optical toroidal vortices[297]. (g) Spatiotemporal light control with frequency-gradient metasurfaces[298].

the applications of STOV wavepackets, particularly those requiring fast responses, such as telecommunications and data encoding where quantum numbers of STLG pulses may play important roles. Furthermore, spatiotemporal vectorial pulse shaping can generate ultrafast optical pulses that enable unprecedented coherent control over light–matter interactions. Given that quantum systems are inherently 3D and vectorial, this method allows for the creation of complex spatiotemporal vectorial structures[300]. This advancement significantly broadens the possibilities for wavepacket structuring and is expected to impact areas requiring vectorial coherent control, such as vectorized optoelectronic control within semiconductors[301,302] (Fig. 40).

### 6.3 Toward Ultrahigh-Dimensional STWPs

Light's degrees of freedom include space, time, amplitude, wavelength, phase, and polarization. Beyond these basics, complex behaviors like OAM and space-time nonseparability reveal new optical phenomena and applications. Combining these DoFs, such as in vector vortex beams, enhances tunability and expands practical uses[1–6]. To advance the generation of ultrahigh-dimensional STWPs that encompass multiple parameters such as amplitude, phase, time, space, polarization, spin, and OAM and their combinations, it is essential to integrate several sophisticated techniques. Achieving this requires employing multidimensional pulse-shaping technologies, such as spatial light modulators and quantum means, which allow for precise control over phase, amplitude, and polarization. Adaptive optics and metasurfaces play a crucial role by dynamically tuning these dimensions and enabling advanced spatial and temporal manipulation. Additionally, frequency domain control techniques, including Fourier transform spectroscopy, are pivotal for managing phase and amplitude across various frequencies. Spatial mode decomposition methods and integrated photonic circuits further contribute by addressing spatial dimensions, such as OAM, and facilitating complex multidimensional control on a single chip. Quantum state engineering, leveraging quantum entanglement and superposition, offers a pathway to manipulate spin and polarization with high precision. The integration of machine learning algorithms can optimize these processes, predicting and adjusting parameters to achieve the desired ultrahigh-dimensional states efficiently. Moreover, ultrafast temporal pulse shaping techniques, such as chirped pulse amplification, enhance the control over the temporal dimension of STWPs. Although some laser modes (STLG and STHG wavepackets) in space-time[134] have been proposed and realized in the laboratory, forming an orthogonal and complete basis in the space-time domain, effectively applying these modes to sculpt spatiotemporally structured light[2] (Fig. 41) across various fields remains an ongoing challenge. Significant effort is needed to address this issue. As such, researchers can significantly expand the capabilities and applications of STWPs, including advanced imaging, communication, quantum computing, and beyond, thereby pushing the boundaries of optical technology and scientific discovery.

### 6.4 Complex Spatiotemporal Topology

Optical topological structures are crucial for various advanced technologies. They enhance data storage and transfer by providing stable, high-density storage solutions through robust topological states. In communication, these structures improve signal stability and reduce losses, facilitating more efficient information transmission. Additionally, they enable the development of novel photonic devices such as sensors with increased sensitivity and resolution, and advanced imaging systems that can capture and analyze complex light patterns. Their robustness to defects and perturbations makes them valuable for applications in quantum computing and information processing,

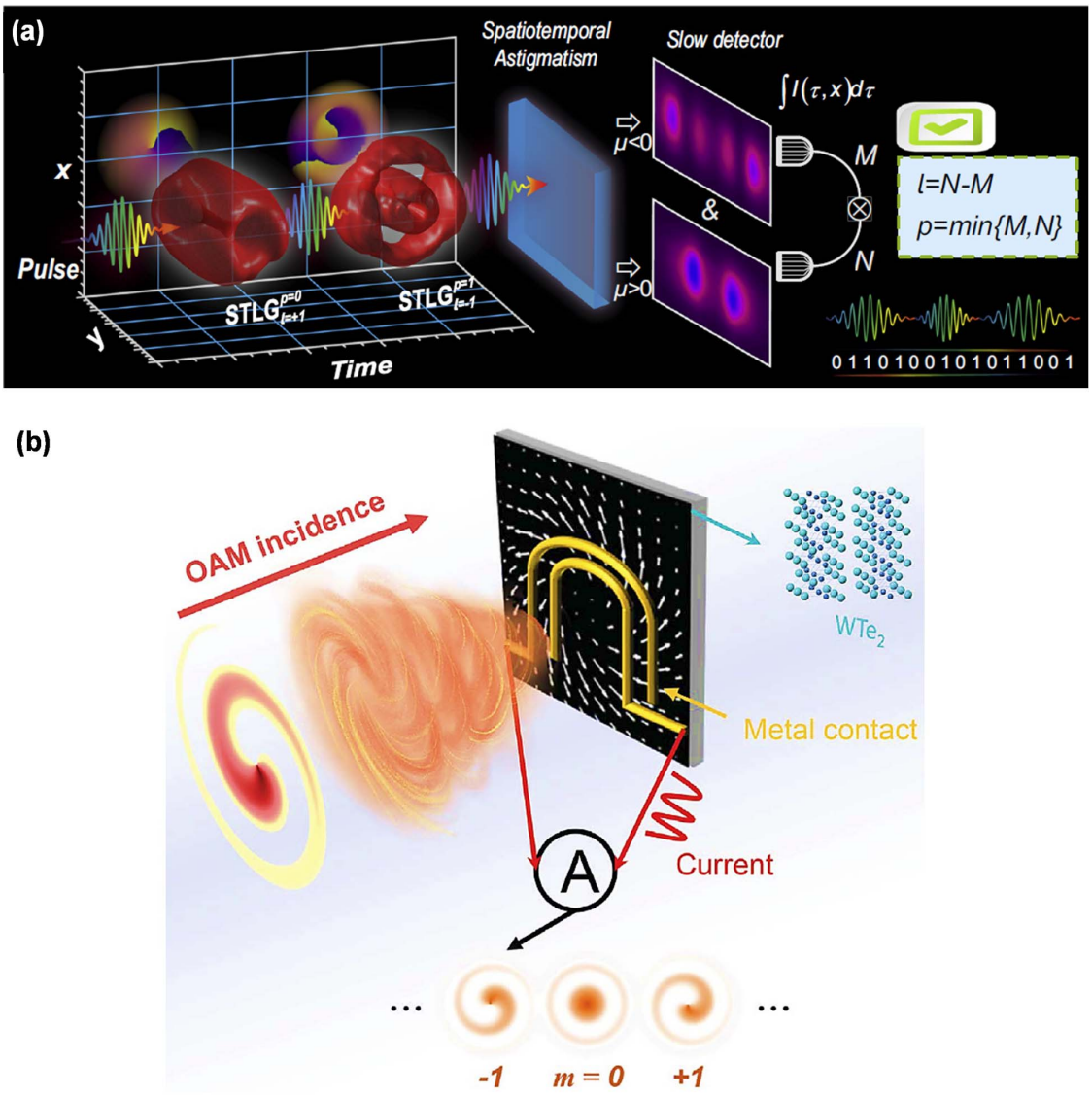


**Fig. 39** Modal state detection and sorting in the space–time domain. (a) Scheme for recognizing radial quantum number and azimuthal quantum number of STLG wavepackets based on mode conversion[134]. (b) Schematic of the photocurrent measurement from optical beams carrying OAM[299].

where precise control of light and data integrity are essential. Recent advancements in spatiotemporal light fields have enabled the creation of more intricate topological structures by exploiting the coupling between spatial and temporal degrees of freedom[303,304]; this approach allows for the formation of complex spatiotemporal topologies, such as higher-dimensional knotted textures and multi-dimensional space-time topology crystals[305] (Fig. 42), which exhibit rich, dynamic behavior and enable novel applications in advanced information processing and wave manipulation. It is noteworthy that recently proposed STOV pulse bursts[214] could be a promising candidate for further experimentally realizing space-time hopfion crystals.

### *6.5 Quantum Entanglement within STWPs*

In the realm of quantum mechanics, STWPs are crucial for exploring and harnessing quantum entanglement. Entanglement, where quantum states of particles become interconnected such that the state of one particle instantaneously influences the state of another, is a cornerstone of quantum information science. Spatiotemporal coupling can be used to generate and manipulate entangled states with greater flexibility and efficiency. This capability is essential for developing advanced quantum technologies such as quantum computing, quantum cryptography, and quantum teleportation. By fine-tuning the spatiotemporal properties of entangled photons, researchers can improve the fidelity and range of quantum communication channels and enhance the performance of quantum algorithms.

Looking ahead, the integration of spatiotemporal coupling with quantum entanglement holds promise for breakthroughs in both theoretical and applied quantum physics. It may lead to new methods for entanglement distribution over longer distances, which is critical for creating a global quantum internet. Additionally, it could enable the exploration of novel quantum

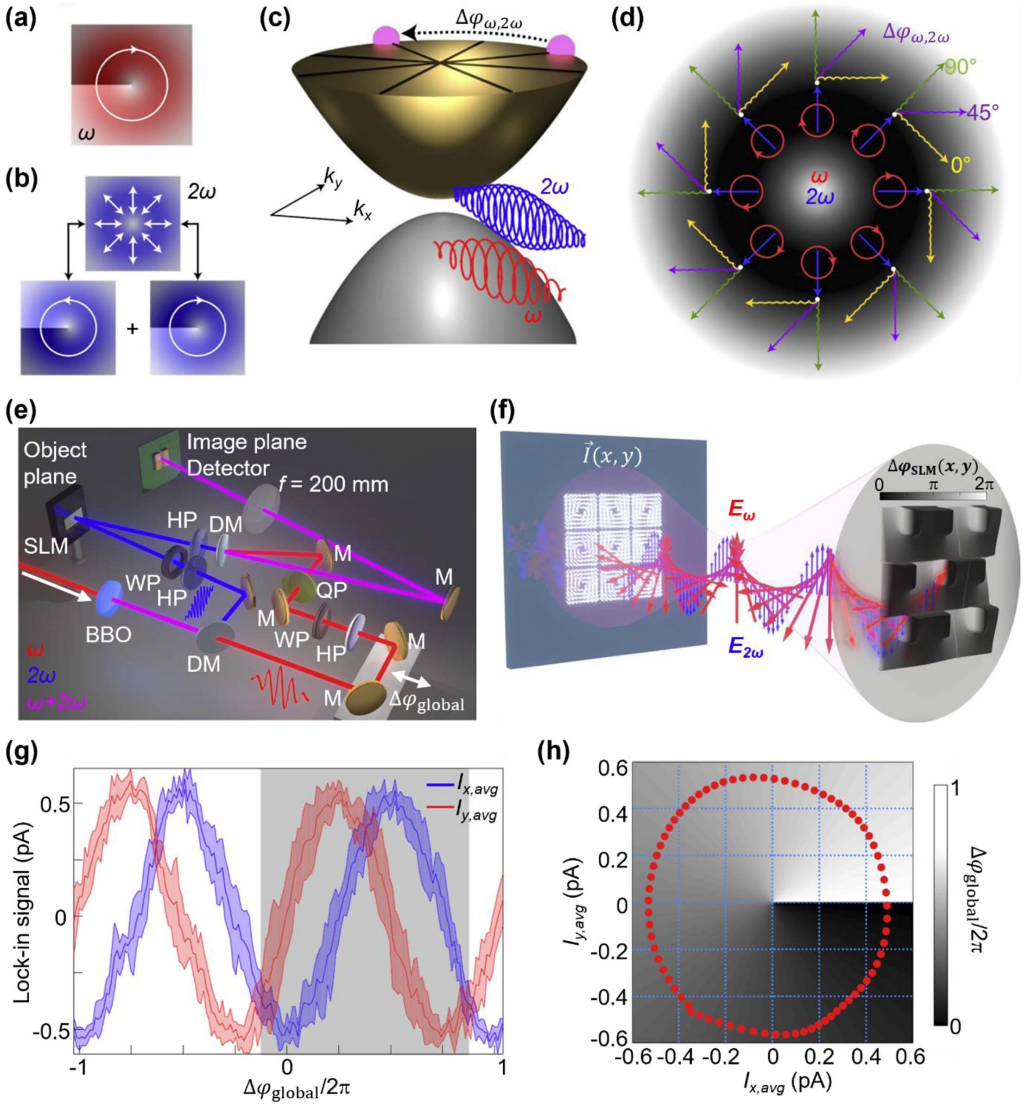


**Fig. 40** Vectorized optoelectronic control by structured light[301,302]. (a) Schematic of left-hand circularly polarized $\omega$ optical vortex with topological charge $m = +1$. (b) Sketch of the $2\omega$ radial polarized beam that can be equivalently represented as a superposition of two circularly polarized beams with opposite handedness possessing $m = -1$ and $m = +1$. (c) Illustration of coherent control in a semiconductor using two circularly polarized beams. Circular polarization enables control over the $x$- and $y$-momentum components by adjustment of $\Delta\varphi_{\omega,2\omega}$. (d) Spatial arrangement of the controlled currents for different $\Delta\varphi_{\omega,2\omega}$. (e) Schematic of the experimental configuration for reconfiguring electronic circuits. (f) The spatial distribution of $\Delta\varphi_{\omega,2\omega}$ generated by a spatial light modulator. (g) Measurement of the $x$ (blue) and $y$ (red) current components in one detection pixel as the global relative phase. (h) Measured vectorial current from $x$ and $y$ components of (g) on a phase map, demonstrating that $\Delta\varphi_{\omega,2\omega}$ can be used to precisely control the direction of currents.

states and phenomena, enriching our understanding of quantum mechanics and expanding the capabilities of quantum technologies. The mutual coupling of multiple degrees of freedom in ultrahigh-dimensional space–time wavepackets can facilitate the realization of quantum entanglement effects across these dimensions. For instance, this coupling can enable the manifestation of quantum entanglement phenomena in OAM and SAM, demonstrating how entanglement can be effectively distributed and manipulated across various degrees of freedom within complex wavepackets[306,307] (Fig. 43). As experimental techniques and theoretical models continue to advance, the interplay between spatiotemporal dynamics and quantum entanglement is likely to unlock transformative opportunities in science and technology.

### 6.6 Nonlinear Microscope and Laser Processing Empowered by STWPs

STWPs not only feature structured spatial patterns but also possess ultrafast temporal envelopes. These properties are coupled in both the spatial and temporal dimensions, creating complex optical degrees of freedom. As a result, such wave packets,

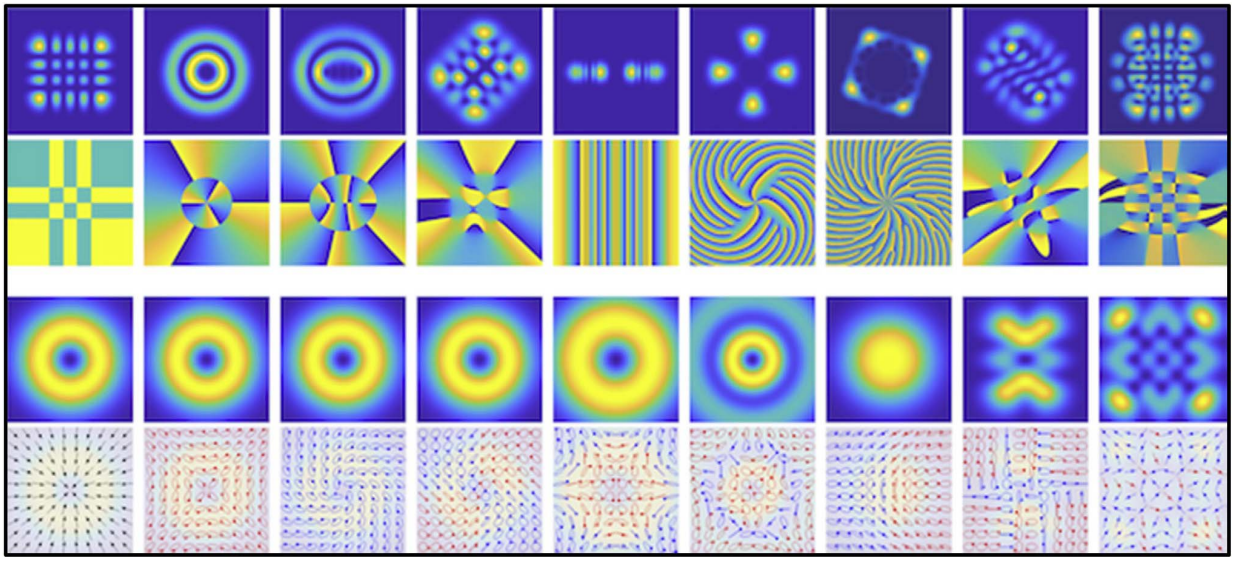

**Fig. 41** A collage of structured light. Examples of the various forms of structured light[2] are shown as scalar beams (top) and vector beams (bottom). The first row in each is the intensity and the second row is the phase (scalar beams) and polarization (vector) structure.

influenced by both spatial diffraction and temporal dispersion, exhibit unique advantages during transmission, focusing, and interactions with matter. Simultaneous spatiotemporal focusing (SSTF) has emerged as a powerful technique in nonlinear microscopy, offering enhanced axial confinement and resolution beyond traditional methods[308–312]. By simultaneously controlling both the spatial and temporal properties of ultrashort pulses, SSTF reduces pulse broadening caused by dispersion, maximizing nonlinear effects like two-photon fluorescence. This capability significantly improves imaging depth and resolution, particularly in scattering tissues, by minimizing out-of-focus background and optimizing focal spot size. In addition, SSTF could enable precise control over the focal region through techniques such as pulse front tilt, allowing for the generation of multiple, temporally separated focal spots from a single pulse, overcoming the interference limitations of conventional holographic spot spacing. These features are particularly beneficial for high-speed, deep-tissue multiphoton imaging, laser processing, and microfluidic device fabrication, where both spatial and temporal focus control is critical.

Besides, SSTF enabled by STWPs may offer significant advantages in laser material processing by reducing nonlinear distortions that typically occur during laser propagation. SSTF achieves this by spatially separating the spectral components of an ultrafast laser pulse, which leads to a controlled increase in pulse duration before recombining the components at the focus. This approach minimizes nonlinear effects such as self-focusing, filamentation, and spectral broadening, resulting in a more confined and precise laser-material interaction[99,313,314]. In applications like femtosecond laser ablation, SSTF enables finer control over material modifications, such as clean and accurate cuts in transparent materials like glass and biological tissues. By reducing unwanted side effects and enhancing focusing precision, SSTF holds promise for improving the quality and efficiency of laser micromachining, eye surgery, and other high-precision processing tasks.

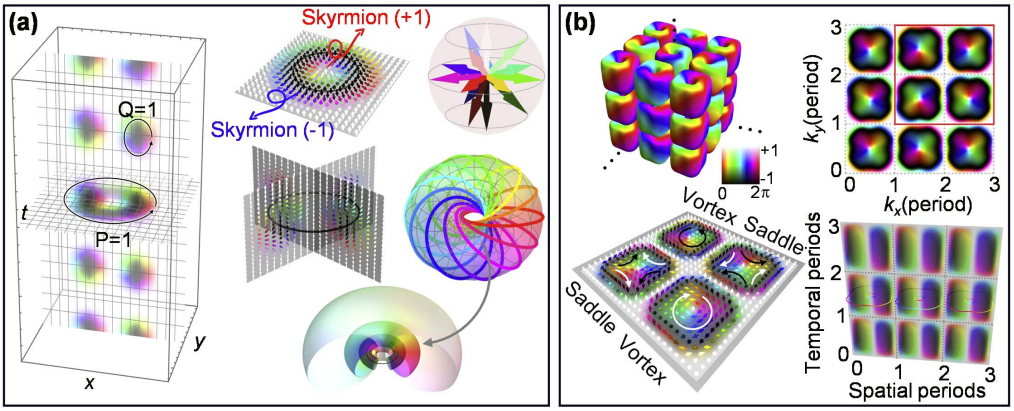


**Fig. 42** Sophisticated space-time topology using STWPs[305]. (a) Illustration of a 1D space–time hopfion crystal where the 3D hopfion texture unit repeats periodically over time. (b) Depiction of a 3D space–time hopfion crystal, showcasing various views of every hopfion unit.

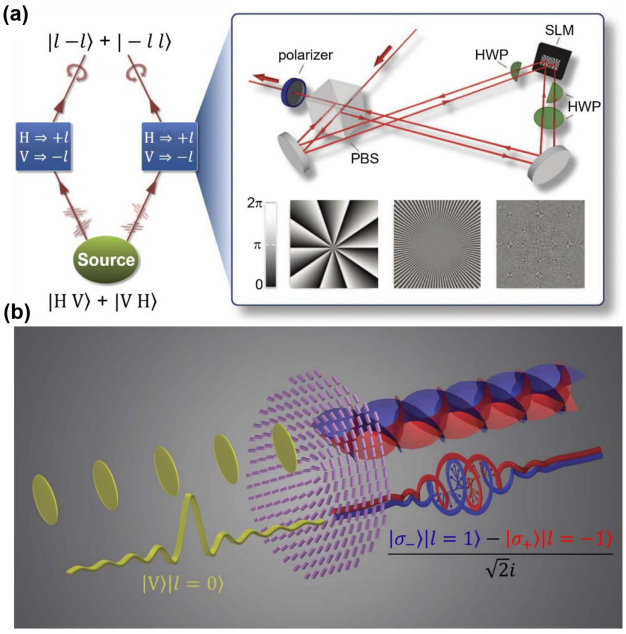


**Fig. 43** Quantum entanglement of OAM beams. (a) Polarization entanglement is created in a parametric down-conversion process and afterward transferred to modes with high quanta of OAM[306]. (b) Entanglement between spin and OAM on a single photon[307]. A single photon vertically polarized is arriving from the left, as illustrated by the yellow wavepacket representing the electric field amplitude. This photon carries zero OAM, as illustrated by the yellow flat phase fronts. The single photon passes through the metasurface nanoantennas (purple) and exits as a single-particle entangled state, depicted as a superposition of the red and blue electric field amplitudes, with the corresponding vortex phase fronts opposite to one another.

### *6.7 Conclusions*

Spatiotemporally structured wavepackets have garnered significant attention in recent years. These wavepackets exhibit intricate control over both spatial and temporal dimensions, enabling more precise manipulation of light fields during propagation compared to conventional beams. Overall, research on spatiotemporally structured wavepackets has made significant strides in recent years, with major advances in both the discovery of fundamental spatiotemporal shaping techniques and the understanding of spatiotemporal dynamics. These developments have been successfully applied across an increasingly broad range of other wave regimes. Current methods for spatiotemporal control primarily rely on linear optics, utilizing bulky dispersion components and spatial light modulators to manage space-spectrum interactions. However, these approaches suffer from low modulation efficiency and are not well-suited for the development of compact, miniaturized devices. While certain nano-structure devices have demonstrated the ability to effectively modulate pulse frequency and generate simple structured wavepackets, such as STOVs, their applications remain limited. To advance the field, the development of metasurfaces and nanophotonic platforms with versatile, multi-degree-of-freedom ($x-y-t$ 3D modulation) modulation capabilities is crucial. These emerging technologies hold promise for enabling more efficient, flexible control of spatiotemporally structured wavepackets, paving the way for practical applications.

Interest in STWPs has surged, particularly with the generation and observation of STOVs and related singularities. This trend parallels the historical development of spatially structured light, which was driven by the study of phase and polarization singularities within spatial light structures. STOVs exhibit topological and conserved properties similar to spatial vortices but with novel characteristics and distinct spatiotemporal evolution dynamics. Variants such as toroidal vortices, hopfions, and knotted optical fields demonstrate unique photonic properties across various optical phenomena, making them increasingly applicable in areas like optical manipulation, spatiotemporal differentiation, subluminal and superluminal pulse propagation, and free-space optical communication. However, much remains to be understood about the physical characteristics of these spatiotemporal singularities and their potential applications. While the future of this rapidly evolving field is difficult to predict, the trajectory of spatial singularity research suggests that new physical mechanisms involving spatiotemporal vortices will likely be uncovered, leading to broader applications in the near future.

Although significant progress has been made in the study of STWPs, current research predominantly focuses on wavepackets with relatively simple structures in the space-time domain. The generation, modulation, and control of more complex, high-dimensional STWPs remain a challenge, as existing techniques are insufficient to fully explore these intricate configurations. Advanced methods for shaping and characterizing such wavepackets are needed to unlock their potential. Moreover, the transmission dynamics of STWPs through various media have yet to be thoroughly investigated experimentally. Key questions remain regarding how these wavepackets behave in complex materials, particularly when high-order dispersion and nonlinear effects are considered. The interaction between space-time coupling and these effects may give rise to new physical mechanisms and phenomena, but this remains largely unexplored. Experimental verification of these theoretical predictions is crucial to advancing the field and understanding the broader implications of spatiotemporal coupling. The development of experimental tools and techniques to probe these interactions will be essential for revealing the full potential of STWPs in material systems. Finally, STWPs show great application potential in the fields of quantum and topological optics and communications. By precisely controlling the space-time characteristics of the light field, STWPs can be used for the transmission and processing of quantum information, especially in improving the manipulation and robustness of quantum entangled states. In addition, the topological properties within STWP provide new means to develop topologically protected quantum states and enhance the system's immunity to noise and scattering. In communications, STWPs may allow the development of more efficient signal encoding and transmission, promote the development of ultrahigh-speed, low-loss free-space communication systems, and bring revolutionary progress to the next generation of optical communication technology.

## *Acknowledgments*

This work was supported by the National Natural Science Foundation of China (Nos. 92050202, 12434012, 12474336, and 12104309), the Zhangjiang Laboratory, Shanghai

Municipal Science and Technology Commission, Shanghai Municipal Education Commission, Shanghai Rising-Star Program (No. 24QA2705800), and the Key Project of Westlake Institute for Optoelectronics (No. 2023GD007).

## References


1. A. Forbes, M. de Oliveira, and M. R. Dennis, "Structured light," *Nat. Photonics* **15**, 253 (2021).
2. A. Forbes, "Structured light from lasers," *Laser Photonics Rev.* **13**, 1900140 (2019).
3. V. Angelsky *et al.*, "Structured light: ideas and concepts," *Front. Phys.* **8**, 114 (2020).
4. C. He, Y. Shen, and A. Forbes, "Towards higher-dimensional structured light," *Light Sci. Appl.* **11**, 205 (2022).
5. W. T. Buono and A. Forbes, "Nonlinear optics with structured light," *Opto-Electron. Adv.* **5**, 210174 (2022).
6. H. Rubinsztein-Dunlop *et al.*, "Roadmap on structured light," *J. Opt.* **19**, 013001 (2016).
7. K. Y. Bliokh *et al.*, "Roadmap on structured waves," *J. Opt.* **25**, 103001 (2023).
8. Y. Shen *et al.*, "Roadmap on spatiotemporal light fields," *J. Opt.* **25**, 093001 (2023).
9. Y. Cai *et al.*, "Generation of partially coherent beams," *Prog. Opt.* **62**, 157 (2017).
10. U. Levy, S. Derevyanko, and Y. Silberberg, "Light modes of free space," *Prog. Opt.* **61**, 237 (2016).
11. Z. Wan *et al.*, "Ultra-degree-of-freedom structured light for ultra-capacity information carriers," *ACS Photonics* **10**, 2149 (2023).
12. M. V. Berry and N. L. Balazs, "Nonspreading wave packets," *Am. J. Phys.* **47**, 264 (1979).
13. G. A. Siviloglou *et al.*, "Observation of accelerating Airy beams," *Phys. Rev. Lett.* **99**, 213901 (2007).
14. G. A. Siviloglou and D. N. Christodoulides, "Accelerating finite energy Airy beams," *Opt. Lett.* **32**, 979 (2007).
15. Y. Zhang, *et al.*, "Guided self-accelerating Airy beams—a mini-review," *Appl. Sci.* **7**, 341 (2017).
16. N. K. Efremidis *et al.*, "Airy beams and accelerating waves: an overview of recent advances," *Optica* **6**, 686 (2019).
17. X. Liu *et al.*, "Generation of novel partially coherent truncated Airy beams via Fourier phase processing," *Opt. Express* **28**, 9777 (2020).
18. Y. Hu *et al.*, "Self-accelerating Airy beams: generation, control, and applications," in *Nonlinear Photonics and Novel Optical Phenomena*, Vol. **170** (Springer, 2012), p. 1.
19. J. Durnin, "Exact solutions for nondiffracting beams. I. The scalar theory," *J. Opt. Soc. Am. A* **4**, 651 (1987).
20. J. DurninJ. J. Miceli, Jr.J. H. Eberly, "Diffraction-free beams," *Phys. Rev. Lett.* **58**, 1499 (1987).
21. N. Chattrapiban *et al.*, "Generation of nondiffracting Bessel beams by use of a spatial light modulator," *Opt. Lett.* **28**, 2183 (2003).
22. S. N. Khonina *et al.*, "Bessel beam: Significance and applications—A progressive review," *Micromachines* **11**, 997 (2020).
23. O. Céspedes Vicente and C. Caloz, "Bessel beams: a unified and extended perspective," *Optica* **8**, 451 (2021).
24. A. V. Christian *et al.*, "Realization of free-space long-distance self-healing Bessel beams," *Laser Photonics Rev.* **13**, 1900103 (2019).
25. A. S. Rao, "A conceptual review on Bessel beams," *Phys. Scr.* **99**, 062007 (2024).
26. P. Zhang *et al.*, "Nonparaxial Mathieu and Weber accelerating beams," *Phys. Rev. Lett.* **109**, 193901 (2012).
27. M. A. Bandres and B. M. Rodríguez-Lara, "Nondiffracting accelerating waves: Weber waves and parabolic momentum," *New J. Phys.* **15**, 013054 (2013).
28. B. M. Rodríguez-Lara, "Normalization of optical Weber waves and Weber-Gauss beams," *J. Opt. Soc. Am. A* **27**, 327 (2010).
29. J. C. Gutiérrez-Vega, M. D. Iturbe-Castillo, and S. Chávez-Cerda, "Alternative formulation for invariant optical fields: Mathieu beams," *Opt. Lett.* **25**, 1493 (2000).
30. L. L. Nguyen Thi and S.-C. Chu, "Generation of on-demand quasi-Mathieu beams with a controlled generation of spatial spectrum of angular Mathieu-Gauss functions with a digital laser," *Opt. Express* **30**, 5283 (2022).
31. M. A. Bandres, "Ince-Gaussian beams," *Opt. Lett.* **29**, 144 (2004).
32. J. B. Bentley *et al.*, "Generation of helical Ince-Gaussian beams with a liquid-crystal display," *Opt. Lett.* **31**, 649 (2006).
33. H. T. Eyyuboğlu, "Propagation analysis of Ince–Gaussian beams in turbulent atmosphere," *Appl. Opt.* **53**, 2290 (2014).
34. A. Yepiz, B. Perez-Garcia, and R. I. Hernandez-Aranda, "Partially coherent Ince–Gaussian beams," *Opt. Lett.* **45**, 3276 (2020).
35. P. Vaveliuk *et al.*, "Caustics, catastrophes, and symmetries in curved beams," *Phys. Rev. A* **92**, 033850 (2015).
36. A. Zannotti *et al.*, "Shaping caustics into propagation-invariant light," *Nat. Commun.* **11**, 3597 (2020).
37. J. D. Ring *et al.*, "Auto-focusing and self-healing of Pearcey beams," *Opt. Express* **20**, 18955 (2012).
38. D. Deng *et al.*, "Virtual source of a Pearcey beam," *Opt. Lett.* **39**, 2703 (2014).
39. Z. Ren *et al.*, "Generation of a family of Pearcey beams based on Fresnel diffraction catastrophes," *J. Opt.* **17**, 105608 (2015).
40. X. Liu *et al.*, "Flexible autofocusing properties of ring Pearcey beams by means of a cross phase," *Opt. Lett.* **46**, 70 (2021).
41. X. Zhou, Z. Pang and D. Zhao, "Partially coherent Pearcey–Gauss beams," *Opt. Lett.* **45**, 5496 (2020).
42. L. Allen *et al.*, "Orbital angular momentum of light and the transformation of Laguerre–Gaussian laser modes," *Phys. Rev. A* **45**, 8185 (1992).
43. Y. Yang, Y. Li, and C. Wang, "Generation and expansion of Laguerre–Gaussian beams," *J. Opt.* **51**, 910 (2022).
44. X. Liu *et al.*, "Experimental realization of scalar and vector perfect Laguerre–Gaussian beams," *Appl. Phys. Lett.* **119**, 021105 (2021).
45. F. Pampaloni and J. Enderlein, "Gaussian, Hermite-Gaussian, and Laguerre–Gaussian beams: A primer," arXiv:0410021 (2004).
46. W. N. Plick and M. Krenn, "Physical meaning of the radial index of Laguerre–Gauss beams," *Phys. Rev. A* **92**, 063841 (2015).
47. M. A. Porras, R. Borghi, and M. Santarsiero, "Relationship between elegant Laguerre–Gauss and Bessel–Gauss beams," *J. Opt. Soc. Am. A* **18**, 177 (2001).
48. E. Zauderer, "Complex argument Hermite–Gaussian and Laguerre–Gaussian beams," *J. Opt. Soc. Am. A* **3**, 465 (1986).
49. E. G. Abramochkin and V. G. Volostnikov, "Generalized Gaussian beams," *J. Opt.* **6**, S157 (2004).
50. G. Liang and Q. Wang, "Controllable conversion between Hermite Gaussian and Laguerre Gaussian modes due to cross phase," *Opt. Express* **27**, 10684 (2019).
51. Y. Wang *et al.*, "Generalised Hermite–Gaussian beams and mode transformations," *J. Opt.* **18**, 055001 (2016).
52. Y. Cai and Q. Lin, "Decentered elliptical Hermite–Gaussian beam," *J. Opt. Soc. Am. A* **20**, 1111 (2003).
53. V. V. Kotlyar and A. A. Kovalev, "Hermite–Gaussian modal laser beams with orbital angular momentum," *J. Opt. Soc. Am. A* **31**, 274 (2014).
54. M. Mazilu *et al.*, "Light beats the spread: "non-diffracting" beams," *Laser Photonics Rev.* **4**, 529 (2010).
55. Y. Ren *et al.*, "Non-diffracting light wave: fundamentals and biomedical applications," *Front. Phys.* **9**, 698343 (2021).
56. Y. Shen *et al.*, "Self-healing of structured light: a review," *J. Opt.* **24**, 103001 (2022).
57. J. Broky *et al.*, "Self-healing properties of optical Airy beams," *Opt. Express* **16**, 12880 (2008).

58. Q. Zhan, "Cylindrical vector beams: from mathematical concepts to applications," *Adv. Opt. Photonics* **1**, 1 (2009).
59. J. Chen, C. Wan, and Q. Zhan, "Engineering photonic angular momentum with structured light: a review," *Adv. Photonics* **3**, 064001 (2021).
60. X. Wang *et al.*, "Generation of arbitrary vector beams with a spatial light modulator and a common path interferometric arrangement," *Opt. Lett.* **32**, 3549 (2007).
61. C. Maurer *et al.*, "Tailoring of arbitrary optical vector beams," *New J. Phys.* **9**, 78 (2007).
62. K. Y. Bliokh *et al.*, "Spin–orbit interactions of light," *Nat. Photonics* **9**, 796 (2015).
63. K. Y. Bliokh and F. Nori, "Transverse and longitudinal angular momenta of light," *Phys. Rep.* **592**, 1 (2015).
64. M. J. Padgett, "Orbital angular momentum 25 years on," *Opt. Express* **25**, 11265 (2017).
65. X. Wang *et al.*, "Recent advances on optical vortex generation," *Nanophotonics* **7**, 1533 (2018).
66. Y. Shen *et al.*, "Optical vortices 30 years on: OAM manipulation from topological charge to multiple singularities," *Light Sci. Appl.* **8**, 90 (2019).
67. H. Zhang *et al.*, "Review on fractional vortex beam," *Nanophotonics* **11**, 241 (2022).
68. L. Mandel and E. Wolf, *Optical Coherence and Quantum Optics* (Cambridge University Press, 1995).
69. Y. Cai, Y. Chen, and F. Wang, "Generation and propagation of partially coherent beams with nonconventional correlation functions: a review [Invited]," *J. Opt. Soc. Am. A* **31**, 2083 (2014).
70. F. Wang, X. Liu, and Y. Cai, "Propagation of partially coherent beam in turbulent atmosphere: a review (invited review)," *Prog. Electromagn. Res.* **150**, 123 (2015).
71. Y. Chen, F. Wang, and Y. Cai, "Partially coherent light beam shaping via complex spatial coherence structure engineering," *Adv. Phys. X* **7**, 2009742 (2022).
72. J. P. Angelo *et al.*, "Review of structured light in diffuse optical imaging," *J. Biomed. Opt.* **24**, 071602 (2018).
73. A. Mosk *et al.*, "Controlling waves in space and time for imaging and focusing in complex media," *Nat. Photonics* **6**, 283 (2012).
74. C. Liang *et al.*, "Optimizing illumination's complex coherence state for overcoming Rayleigh's resolution limit," *Chin. Opt. Lett.* **19**, 052601 (2021).
75. N. Bender *et al.*, "Circumventing the optical diffraction limit with customized speckles," *Optica* **8**, 122 (2021).
76. M. Pascucci *et al.*, "Superresolution imaging of optical vortices in a speckle pattern," *Phys. Rev. Lett.* **116**, 093904 (2016).
77. X. Chen, M. E. Kandel, and G. Popescu, "Spatial light interference microscopy: principle and applications to biomedicine," *Adv. Opt. Photonics* **13**, 353 (2021).
78. M. G. Gustafsson, "Nonlinear structured-illumination microscopy: wide-field fluorescence imaging with theoretically unlimited resolution," *Proc. Natl. Acad. Sci.* **102**, 13081 (2005).
79. Y. Yang *et al.*, "Optical trapping with structured light: a review," *Adv. Photonics* **3**, 034001 (2021).
80. E. Otte and C. Denz, "Optical trapping gets structure: Structured light for advanced optical manipulation," *Appl. Phys. Rev.* **7**, 041308 (2020).
81. X. Lin *et al.*, "All-optical machine learning using diffractive deep neural networks," *Science* **361**, 1004 (2018).
82. X. Liu *et al.*, "Axial correlation revivals and number factorization with structured random waves," *Phys. Rev. Appl.* **20**, L021004 (2023).
83. X. Li *et al.*, "Prime number factorization with light beams carrying orbital angular momentum," *APL Photonics* **9**, 046107 (2024).
84. J. Wang *et al.*, "Terabit free-space data transmission employing orbital angular momentum multiplexing," *Nat. Photonics* **6**, 488 (2012).
85. T. Lei *et al.*, "Massive individual orbital angular momentum channels for multiplexing enabled by Dammann gratings," *Light Sci. Appl.* **4**, e257 (2015).
86. M. Duocastella and C. B. Arnold, "Bessel and annular beams for materials processing," *Laser Photonics Rev.* **6**, 607 (2012).
87. S. Syubaev *et al.*, "Direct laser printing of chiral plasmonic nanojets by vortex beams," *Opt. Express* **25**, 10214 (2017).
88. M. Erhard *et al.*, "Twisted photons: new quantum perspectives in high dimensions," *Light Sci. Appl.* **7**, 17146 (2018).
89. X. L. Wang *et al.*, "Quantum teleportation of multiple degrees of freedom of a single photon," *Nature* **518**, 516 (2015).
90. A. M. Weiner, "Femtosecond pulse shaping using spatial light modulators," *Rev. Sci. Instrum.* **71**, 1929 (2000).
91. A. M. Weiner, "Ultrafast optical pulse shaping: A tutorial review," *Opt. Commun.* **284**, 3669 (2011).
92. Z. Jiang *et al.*, "Optical arbitrary waveform processing of more than 100 spectral comb lines," *Nat. Photonics* **1**, 463 (2007).
93. S. T. Cundiff and A. M. Weiner, "Optical arbitrary waveform generation," *Nat. Photonics* **4**, 760 (2010).
94. C. Zhou, "Chirped pulse amplification: review and prospective from diffractive optics," *Chin. Opt. Lett.* **18**, 110502 (2020).
95. W. Zhang *et al.*, "Review of pulse compression gratings for chirped pulse amplification system," *Opt. Eng.* **60**, 020902 (2021).
96. V. Torres-Company and A. M. Weiner, "Optical frequency comb technology for ultra-broadband radio-frequency photonics," *Laser Photonics Rev.* **8**, 368 (2014).
97. F. Ferdous *et al.*, "Spectral line-by-line pulse shaping of on-chip microresonator frequency combs," *Nat. Photonics* **5**, 770 (2011).
98. L. Chang, S. Liu, and J. E. Bowers, "Integrated optical frequency comb technologies," *Nat. Photonics* **16**, 95 (2022).
99. C. Kerse *et al.*, "Ablation-cooled material removal with ultrafast bursts of pulses," *Nature* **537**, 84 (2016).
100. V. Stummer *et al.*, "Programmable generation of terahertz bursts in chirped-pulse laser amplification," *Optica* **7**, 1758 (2020).
101. K. Shimada *et al.*, "Spectrum shuttle for producing spatially shapable GHz burst pulses," *Adv. Photonics Nexus* **3**, 016002 (2024).
102. J. N. Brittingham, "Focus wave modes in homogeneous Maxwell's equations: Transverse electric mode," *J. Appl. Phys.* **54**, 1179 (1983).
103. K. Reivelt and P. Saari, "Experimental demonstration of realizability of optical focus wave modes," *Phys. Rev. E* **66**, 056611 (2002).
104. J. Y. Lu and J. F. Greenleaf, "Nondiffracting X-waves. Exact solutions to free space scalar wave equation and their finite aperture realizations," *IEEE Trans. Ultrason. Ferroelec. Freq. Control* **39**, 19 (1992).
105. P. Di Trapani *et al.*, "Spontaneously generated X-shaped light bullets," *Phys. Rev. Lett.* **91**, 093904 (2003).
106. P. Saari and K. Reivelt, "Evidence of X-shaped propagation-invariant localized light waves," *Phys. Rev. Lett.* **79**, 4135 (1997).
107. M. A. Porras *et al.*, "Paraxial envelope X waves," *Opt. Lett.* **28**, 1090 (2003).
108. C. Conti *et al.*, "Nonlinear electromagnetic X waves," *Phys. Rev. Lett.* **90**, 170406 (2003).
109. M. A. Porras and P. Di Trapani, "Localized and stationary light wave modes in dispersive media," *Phys. Rev. E* **69**, 066606 (2004).
110. M. A. Porras *et al.*, "From X to O-shaped spatiotemporal spectra of light filaments in water," *Opt. Lett.* **30**, 3398 (2005).
111. S. Malaguti and S. Trillo, "Envelope localized waves of the conical type in linear normally dispersive media," *Phys. Rev. A* **79**, 063803 (2009).
112. S. Longhi, "Localized subluminal envelope pulses in dispersive media," *Opt. Lett.* **29**, 147 (2004).
113. A. Chong *et al.*, "Airy-Bessel wave packets as versatile linear light bullets," *Nat. Photonics* **4**, 103 (2010).

114. W. P. Zhong, M. Belić, and Y. Zhang, "Three-dimensional localized Airy–Laguerre–Gaussian wave packets in free space," *Opt. Express* **23**, 23867 (2015).
115. M. A. Porras, "Nonsinusoidal few-cycle pulsed light beams in free space," *J. Opt. Soc. Am. B* **16**, 1468 (1999).
116. M. A. Porras, "Diffraction-free and dispersion-free pulsed beam propagation in dispersive media," *Opt. Lett.* **26**, 1364 (2001).
117. S. W. Hancock *et al.*, "Free-space propagation of spatiotemporal optical vortices," *Optica* **6**, 1547 (2019).
118. A. Chong *et al.*, "Generation of spatiotemporal optical vortices with controllable transverse orbital angular momentum," *Nat. Photonics* **14**, 350 (2020).
119. C. Wan, A. Chong, and Q. Zhan, "Optical spatiotemporal vortices," *eLight* **3**, 11 (2003).
120. W. Chen, Y. Liu, and Y. Q. Lu, "Spatiotemporal optical vortices: toward tailoring orbital angular momentum of light in full spacetime," *ACS Photonics* **10**, 2011 (2023).
121. A. Bekshaev, "Spatiotemporal optical vortices: principles of description and basic properties," *APL Photonics* **9**, 110806 (2024).
122. Q. Zhan, "Spatiotemporal sculpturing of light: a tutorial," *Adv. Opt. Photonics* **16**, 163 (2024).
123. H. E. Kondakci and A. F. Abouraddy, "Diffraction-free pulsed optical beams via space-time correlations," *Opt. Express* **24**, 28659 (2016).
124. K. J. Parker and M. A. Alonso, "Longitudinal iso-phase condition and needle pulses," *Opt. Express* **24**, 28669 (2016).
125. M. Yessenov *et al.*, "Space-time wave packets," *Adv. Opt. Photonics* **14**, 455 (2022).
126. H. E. Kondakci and A. F. Abouraddy, "Diffraction-free space–time light sheets," *Nat. Photonics* **11**, 733 (2017).
127. L. Rego *et al.*, "Generation of extreme-ultraviolet beams with time-varying orbital angular momentum," *Science* **364**, eaaw9486 (2019).
128. Z. Zhao *et al.*, "Dynamic spatiotemporal beams that combine two independent and controllable orbital-angular-momenta using multiple optical-frequency-comb lines," *Nat. Commun.* **11**, 4099 (2020).
129. C. Wan *et al.*, "Toroidal vortices of light," *Nat. Photonics* **16**, 519 (2022).
130. A. Zdagkas *et al.*, "Observation of toroidal pulses of light," *Nat. Photonics* **16**, 523 (2022).
131. B. H. Kolner, "Space-time duality and the theory of temporal imaging," *IEEE J. Quantum Electron.* **30**, 1951 (1994).
132. A. M. Weiner, *Ultrafast Optics* (Wiley, 2011).
133. O. E. Martinez, "Grating and prism compressors in the case of finite beam size," *J. Opt. Soc. Am. B* **3**, 929 (1986).
134. X. Liu *et al.*, "Spatiotemporal optical vortices with controllable radial and azimuthal quantum numbers," *Nat. Commun.* **15**, 5435 (2024).
135. Q. Cao *et al.*, "Spatiotemporal hologram," *Nat. Commun.* **15**, 7821 (2024).
136. W. Chen *et al.*, "Tailoring spatiotemporal wavepackets via two-dimensional space-time duality," arXiv:2402.07794 (2024).
137. D. Kim *et al.*, "Shaping space-time wavepackets beyond the paraxial limit using a dispersion magnifier," arXiv:2409.10454 (2024).
138. Y. Saito, K. Shin-ichi, and O. Hitoshi, "Scale and rotation invariant real time optical correlator using computer generated hologram," *Opt. Commun.* **47**, 8 (1983).
139. W. J. Hossack, A. M. Darling, and A. Dahdouh, "Coordinate transformations with multiple computer-generated optical elements," *J. Mod. Opt.* **34**, 1235 (1987).
140. O. Bryngdahl, "Geometrical transformations in optics," *J. Opt. Soc. Am. A* **64**, 1092 (1974).
141. G. C. G. Berkhout *et al.*, "Efficient sorting of orbital angular momentum states of light," *Phys. Rev. Lett.* **105**, 153601 (2010).
142. Y. Wen *et al.*, "Spiral transformation for high-resolution and efficient sorting of optical vortex modes," *Phys. Rev. Lett.* **120**, 193904 (2018).
143. Y. Wen *et al.*, "Arbitrary multiplication and division of the orbital angular momentum of light," *Phys. Rev. Lett.* **124**, 213901 (2020).
144. G. Ruffato, M. Michele, and R. Filippo, "Multiplication and division of the orbital angular momentum of light with diffractive transformation optics," *Light Sci. Appl.* **8**, 113 (2019).
145. J. Cheng, C. Wan, and Q. Zhan, "Generalized spiral transformation for high-resolution sorting of vortex modes," *Opt. Lett.* **48**, 1762 (2023).
146. Z. Zeng *et al.*, "Multiplication and division of orbital angular momentum beams by Fermat's spiral transformation," *Photonics Res.* **11**, 165 (2023).
147. H. Zhou *et al.*, "Orbital angular momentum divider of light," *IEEE Photonics J.* **9**, 6500208 (2016).
148. G. Ruffato *et al.*, "Test of mode-division multiplexing and demultiplexing in free-space with diffractive transformation optics," *Opt. Express* **25**, 7859 (2017).
149. Y. Zhang and N. K. Fontaine, "Multi-plane light conversion: a practical tutorial," arXiv:2304.11323 (2023).
150. N. K. Fontaine *et al.*, "Design of high order mode-multiplexers using multiplane light conversion," in *European Conference on Optical Communication* (2017).
151. N. K. Fontaine *et al.*, "Laguerre–Gaussian mode sorter," *Nat. Commun.* **10**, 1865 (2019).
152. H. Kupianskyi *et al.*, "High-dimensional spatial mode sorting and optical circuit design using multi-plane light conversion," *APL Photonics* **8**, 026101 (2023).
153. O. Lib, K. Sulimany, and Y. Bromberg, "Processing entangled photons in high dimensions with a programmable light converter," *Phys. Rev. Appl.* **18**, 014063 (2022).
154. M. Eriksson *et al.*, "Sensing rotations with multiplane light conversion," *Phys. Rev. Appl.* **20**, 024052 (2023).
155. A. I. Kuznetsovet *et al.*, "Roadmap for optical metasurfaces," *ACS Photonics* **11**, 816 (2024).
156. S. A. Schulz *et al.*, "Roadmap on photonic metasurfaces," *Appl. Phys. Lett.* **124**, 260701 (2024).
157. S. Hend *et al.*, "High-purity orbital angular momentum states from a visible metasurface laser," *Nat. Photonics* **14**, 498 (2020).
158. N. Yu *et al.*, "Light propagation with phase discontinuities: generalized laws of reflection and refraction," *Science* **334**, 333 (2011).
159. Y.-Y. Xie *et al.*, "Metasurface-integrated vertical cavity surface-emitting lasers for programmable directional lasing emissions," *Nat. Nanotechnol.* **15**, 125 (2020).
160. M. Decker *et al.*, "High-efficiency dielectric Huygens' surfaces," *Adv. Opt. Mater.* **3**, 813 (2015).
161. K. Chong *et al.*, "Polarization-independent silicon metadevices for efficient optical wavefront control," *Nano Lett.* **15**, 5369 (2015).
162. G. Zheng *et al.*, "Metasurface holograms reaching 80% efficiency," *Nat. Nanotechnol.* **10**, 308 (2015).
163. D. Lin *et al.*, "Dielectric gradient metasurface optical elements," *Science* **345**, 298 (2014).
164. A. Arbabi *et al.*, "Dielectric metasurfaces for complete control of phase and polarization with subwavelength spatial resolution and high transmission," *Nat. Nanotechnol.* **10**, 937 (2015).
165. J. P. Balthasar Mueller *et al.*, "Metasurface Polarization Optics: Independent Phase Control of Arbitrary Orthogonal States of Polarization," *Phys. Rev. Lett.* **118**, 113901 (2017).
166. R. Devlin *et al.*, "Arbitrary spin-to–orbital angular momentum conversion of light," *Science* **358**, 896 (2017).
167. H. Ren *et al.*, "Complex-amplitude metasurface-based orbital angular momentum holography in momentum space," *Nat. Nanotech.* **15**, 948 (2020).

168. S. Divitt *et al.*, "Ultrafast optical pulse shaping using dielectric metasurfaces," *Science* **364**, 890 (2019).
169. A. P. Sukhorukov and V. V. Yangirova, "Spatio-temporal vortices: properties, generation and recording," *Proc. SPIE* **5949**, 594906 (2005).
170. K. Y. Bliokh and F. Nori, "Spatiotemporal vortex beams and angular momentum," *Phys. Rev. A* **86**, 033824 (2012).
171. K. Y. Bliokh, "Spatiotemporal vortex pulses: angular momenta and spin-orbit interaction," *Phys. Rev. Lett.* **126**, 243601 (2021).
172. N. Jhajj *et al.*, "Spatiotemporal Optical Vortices," *Phys. Rev. X* **6**, 031037 (2016).
173. Q. Cao *et al.*, "Non-spreading Bessel spatiotemporal optical vortices," *Sci. Bull.* **67**, 133 (2022).
174. W. Chen *et al.*, "Time diffraction-free transverse orbital angular momentum beams," *Nat. Commun.* **13**, 4021 (2022).
175. S. A. Ponomarenko and D. Hebri, "Perfect space–time vortices," *Opt. Lett.* **49**, 4322 (2024).
176. G. Gbur and R. Tyson, "Vortex beam propagation through atmospheric turbulence and topological charge conservation," *J. Opt. Soc. Am. A* **25**, 225 (2008).
177. M. Dong *et al.*, "Partially coherent vortex beams: fundamentals and applications," *Sci. China Phys. Mech. Astron.* **64**, 224201 (2021).
178. H. V. Hyde, "Twisted space-frequency and space-time partially coherent beams," *Sci. Rep.* **10**, 12443 (2020).
179. M. V. Hyde, "Twisted spatiotemporal optical vortex beams in dispersive media," *Opt. Commun.* **566**, 130682 (2024).
180. M. V. Hyde, O. Korotkova, and M. F. Spencer, "Partially coherent sources whose coherent modes are spatiotemporal optical vortex beams," *J. Opt.* **25**, 035606 (2023).
181. A. Mirando *et al.*, "Generation of spatiotemporal optical vortices with partial temporal coherence," *Opt. Express* **29**, 30426 (2021).
182. C. Ding *et al.*, "Method for generating spatiotemporal coherency vortices and spatiotemporal dislocation curves," *Opt. Express* **32**, 609 (2023).
183. C. Ding *et al.*, "Source coherence-induced control of spatiotemporal coherency vortices," *Opt. Express* **30**, 19871 (2022).
184. H. Wang *et al.*, "Engineering arbitrarily oriented spatiotemporal optical vortices using transmission nodal lines," *Optica* **8**, 966 (2021).
185. J. Huang *et al.*, "Spatiotemporal differentiators generating optical vortices with transverse orbital angular momentum and detecting sharp change of pulse envelope," *Laser Photonics Rev.* **16**, 2100357 (2022).
186. J. Huang *et al.*, "Topologically protected generation of spatiotemporal optical vortices with nonlocal spatial mirror symmetry breaking metasurface," *Phys. Rev. B* **108**, 104106 (2023).
187. P. Huo *et al.*, "Observation of spatiotemporal optical vortices enabled by symmetry-breaking slanted nanograting," *Nat. Commun.* **15**, 3055 (2024).
188. W. Liu *et al.*, "Exploiting topological darkness in photonic crystal slabs for spatiotemporal vortex generation," *Nano Lett.* **24**, 943 (2024).
189. Z. Che *et al.*, "Generation of spatiotemporal vortex pulses by resonant diffractive grating," *Phys. Rev. Lett.* **132**, 044001 (2024).
190. X. Ni *et al.*, "Three-dimensional reconfigurable optical singularities in bilayer photonic crystals," *Phys. Rev. Lett.* **132**, 073804 (2024).
191. S. Huang *et al.*, "Diffraction properties of light with transverse orbital angular momentum," *Optica* **9**, 469 (2022).
192. S. W. Hancock, S. Zahedpour, and H. M. Milchberg, "Mode structure and orbital angular momentum of spatiotemporal optical vortex pulses," *Phys. Rev. Lett.* **127**, 193901 (2021).
193. M. Hyde and A. P. Miguel, "Propagation of spatiotemporal optical vortex beams in linear, second-order dispersive media," *Phys. Rev. A* **108**, 013519 (2023).
194. M. Mazanov *et al.*, "Transverse shifts and time delays of spatiotemporal vortex pulses reflected and refracted at a planar interface," *Nanophotonics* **11**, 737 (2022).
195. F. Tang and L. Chen, "Centroid shifts of spatiotemporal vortex pulses with arbitrarily oriented orbital angular momentum at planar reflection and refraction," *Phys. Rev. A* **109**, 033512 (2024).
196. M. A. Porras, "Propagation of higher-order spatiotemporal vortices," *Opt. Lett.* **48**, 367 (2023).
197. J. Chen *et al.*, "Spin–orbit coupling within tightly focused circularly polarized spatiotemporal vortex wavepacket," *ACS Photonics* **9**, 793 (2022).
198. M. A. Porras and S. W. Jolly, "Procedure for imparting transverse orbital angular momentum by focusing spatiotemporally coupled ultrashort pulses," *Phys. Rev. A* **109**, 033514 (2024).
199. M. S. Le *et al.*, "Self-focused pulse propagation is mediated by spatiotemporal optical vortices," *Phys. Rev. Lett.* **133**, 053803 (2024).
200. S. Huang *et al.*, "Properties of the generation and propagation of spatiotemporal optical vortices," *Opt. Express* **29**, 26995 (2021).
201. J. Song *et al.*, "Propagation dynamics of a spatiotemporal vortex pulse in the spatial fractional system," *Photonics Res.* **12**, 2027 (2024).
202. C. Wan *et al.*, "Photonic orbital angular momentum with controllable orientation," *Natl. Sci. Rev.* **9**, nwab149 (2022).
203. H. Wang *et al.*, "Engineering arbitrarily oriented spatiotemporal optical vortices using transmission nodal lines," *Optica* **8**, 966 (2021).
204. Y. Zang, A. Mirando, and A. Chong, "Spatiotemporal optical vortices with arbitrary orbital angular momentum orientation by astigmatic mode converters," *Nanophotonics* **11**, 745 (2022).
205. M. A. Porras and S. W. Jolly, "Control of vortex orientation of ultrashort optical pulses using a spatial chirp," *Opt. Lett.* **48**, 6448 (2023).
206. Q. Cao *et al.*, "Sculpturing spatiotemporal wavepackets with chirped pulses," *Photonics Res.* **9**, 2261 (2021).
207. L. Gu, Q. Cao, and Q. Zhan, "Spatiotemporal optical vortex wavepackets with phase singularities embedded in multiple domains," *Chin. Opt. Lett.* **21**, 080003 (2023).
208. J. Adams, I. Agha, and A. Chong, "Spatiotemporal optical vortex reconnections of multi-vortices," *Sci. Rep.* **14**, 5483 (2024).
209. J. Chen *et al.*, "Experimental demonstration of cylindrical vector spatiotemporal optical vortex," *Nanophotonics* **10**, 4489 (2021).
210. J. Chen *et al.*, "Orbit–orbit interaction in spatiotemporal optical vortex," *Engineering* (2024).
211. C. Wan *et al.*, "Generation of ultrafast spatiotemporal wave packet embedded with time-varying orbital angular momentum," *Sci. Bull.* **65**, 1334 (2020).
212. S. W. Hancock *et al.*, "Spatiotemporal torquing of light," *Phys. Rev. X* **14**, 011031 (2024).
213. S. Huang *et al.*, "Spatiotemporal vortex strings," *Sci. Adv.* **10**, eadn6206 (2024).
214. X. Liu *et al.*, "Ultrafast bursts of tailored spatiotemporal vortex pulses," arXiv:2407.19747 (2024).
215. G. Gui *et al.*, "Second-harmonic generation and the conservation of spatiotemporal orbital angular momentum of light," *Nat. Photonics* **15**, 608 (2021).
216. S. W. Hancock, S. Zahedpour, and H. M. Milchberg, "Second-harmonic generation of spatiotemporal optical vortices and conservation of orbital angular momentum," *Optica* **8**, 594 (2021).
217. R. W. Boyd, *Nonlinear Optics* (Academic, 2008), p. 69.
218. Y. Fang, S. Lu, and Y. Liu, "Controlling photon transverse orbital angular momentum in high harmonic generation," *Phys. Rev. Lett.* **127**, 273901 (2021).
219. J. Dong *et al.*, "Scheme for generation of spatiotemporal optical vortex attosecond pulse trains," *Photonics Res.* **12**, 2409 (2024).
220. F. Cardano and L. Marrucci, "Smoke rings of light," *Nat. Photonics* **16**, 476 (2022).
221. C. Wan *et al.*, "Scalar optical hopfions," *eLight* **2**, 22 (2022).

222. W. Chen *et al.*, "Observation of Chiral Symmetry Breaking in Toroidal Vortices of Light," *Phys. Rev. Lett.* **132**, 153801 (2024).
223. Q. Lin *et al.*, "Direct space–time manipulation mechanism for spatio-temporal coupling of ultrafast light field," *Nat. Commun.* **15**, 2416 (2024).
224. K. Y. Bliokh, "Orbital angular momentum of optical, acoustic, and quantum-mechanical spatiotemporal vortex pulses," *Phys. Rev. A* **107**, L031501 (2023).
225. H. Ge *et al.*, "Spatiotemporal acoustic vortex beams with transverse orbital angular momentum," *Phys. Rev. Lett.* **131**, 014001 (2023).
226. H. Zhang *et al.*, "Topologically crafted spatiotemporal vortices in acoustics," *Nat. Commun.* **14**, 6238 (2023).
227. S. Liu *et al.*, "Generation of spatiotemporal acoustic vortices with arbitrarily oriented orbital angular momentum," arXiv:2406.18084 (2024).
228. D. Yang *et al.*, "Plasmonic toroidal vortices," *Laser Photonics Rev.* **18**, 2400474 (2024).
229. T. Zhang *et al.*, "Spatiotemporal beating and vortices of van der Waals hyperbolic polaritons," *Proc. Natl. Acad. Sci.* **121**, e2319465121 (2024).
230. H. Kondakci and A. F. Abouraddy, "Airy wave packets accelerating in space-time," *Phys. Rev. Lett.* **120**, 163901 (2018).
231. M. Yessenov *et al.*, "Veiled talbot effect," *Phys. Rev. Lett.* **125**, 243901 (2020).
232. G. Pariente and F. Quéré, "Spatio-temporal light springs: extended encoding of orbital angular momentum in ultrashort pulses," *Opt. Lett.* **40**, 2037 (2015).
233. P. Béjot and B. Kibler, "Spatiotemporal helicon wavepackets," *ACS Photonics* **8**, 2345 (2021).
234. X. Su *et al.*, "Temporally and longitudinally tailored dynamic space-time wave packets," *Opt. Express* **32**, 26653 (2024).
235. H. B. Sedeh, M. M. Salary, and H. Mosallaei, "Time-varying optical vortices enabled by time-modulated metasurfaces," *Nanophotonics* **9**, 2957 (2020).
236. L. Chen *et al.*, "Synthesizing ultrafast optical pulses with arbitrary spatiotemporal control," *Sci. Adv.* **8**, eabq8314 (2022).
237. B. Chen *et al.*, "Integrated optical vortex microcomb," *Nat. Photonics* **18**, 625 (2024).
238. Y. Liu *et al.*, "Integrated vortex soliton microcombs," *Nat. Photonics* **18**, 632 (2024).
239. M. Piccardo *et al.*, "Broadband control of topological–spectral correlations in space–time beams," *Nat. Photonics* **17**, 822 (2023).
240. M. Oliveira and A. Ambrosio, "Sub-cycle modulation of light's Orbital Angular Momentum," arXiv:2405.13723 (2024).
241. D. Cruz-Delgado *et al.*, "Synthesis of ultrafast wavepackets with tailored spatiotemporal properties," *Nat. Photonics* **16**, 686 (2022).
242. D. Cruz-Delgado *et al.*, "Ptychography for Multidimensional Characterization of Spatiotemporal Ultrafast Pulses," *ACS Photonics* **11**, 18 (2024).
243. D. Cruz-Delgado *et al.*, "Spatiotemporal Control of Ultrafast Pulses in Multimode Optical Fibers," arXiv:2402.11783 (2024).
244. N. Papasimakis *et al.*, "Pulse generation scheme for flying electromagnetic doughnuts," *Phys. Rev. B* **97**, 201409 (2018).
245. Y. Shen, N. Papasimakis, and N. I. Zheludev, "Nondiffracting supertoroidal pulses and optical "Kármán vortex streets," *Nat. Commun.* **15**, 4863 (2024).
246. R. Wang *et al.*, "Optical atompilz: propagation-invariant strongly longitudinally polarized toroidal pulses," *Appl. Phys. Lett.* **125**, 111101 (2024).
247. K. Jana *et al.*, "Quantum control of flying doughnut terahertz pulses," *Sci. Adv.* **10**, eadl1803 (2024).
248. R. Wang *et al.*, "Observation of resilient propagation and free-space skyrmions in toroidal electromagnetic pulses," *Appl. Phys. Rev.* **11**, 031411 (2024).
249. R. Wang *et al.*, "Hybrid electromagnetic toroidal vortices," arXiv:2408.10472 (2024).
250. Y. Shen *et al.*, "Supertoroidal light pulses as electromagnetic skyrmions propagating in free space," *Nat. Commun.* **12**, 5891 (2021).
251. J. Zhong, C. Wan, and Q. Zhan, "Optical twisted phase strips," *ACS Photonics* **10**, 3384 (2023).
252. S. W. Jolly, G. Olivier, and Q. Fabien, "Spatio-temporal characterization of ultrashort laser beams: a tutorial," *J. Opt.* **22**, 103501 (2020).
253. B. Alonso, A. Döpp, and S. W. Jolly, "Space–time characterization of ultrashort laser pulses: a perspective," *APL Photonics* **9**, 070901 (2024).
254. H. Li *et al.*, "Three-dimensional laser pulse intensity diagnostic for photoinjectors," *Phys. Rev. Accel. Beams* **14**, 112802 (2011).
255. J. Chen *et al.*, "Automated close-loop system for three-dimensional characterization of spatiotemporal optical vortex," *Front. Phys.* **9**, 633922 (2021).
256. G. Gui *et al.*, "Single-frame characterization of ultrafast pulses with spatiotemporal orbital angular momentum," *ACS Photonics* **9**, 2802 (2022).
257. F. Salin *et al.*, "Single-shot measurement of a 52-fs pulse," *Appl. Opt.* **26**, 4528 (1987).
258. R. Trebino and D. J. Kane, "Using phase retrieval to measure the intensity and phase of ultrashort pulses: frequency-resolved optical gating," *J. Opt. Soc. Am. A.* **10**, 1101 (1993).
259. D. J. Kane and R. Trebino, "Single-shot measurement of the intensity and phase of an arbitrary ultrashort pulse by using frequency-resolved optical gating," *Opt. Lett.* **18**, 823 (1993).
260. J. N. Sweetser, D. N. Fittinghoff, and R. Trebino, "Transient-grating frequency-resolved optical gating," *Opt. Lett.* **22**, 519 (1997).
261. K. W. Delong *et al.*, "Frequency-resolved optical gating with the use of second-harmonic generation," *J. Opt. Soc. Am. B.* **11**, 2206 (1994).
262. P. O'Shea *et al.*, "Highly simplified device for ultrashort-pulse measurement," *Opt. Lett.* **26**, 932 (2001).
263. C. Iaconis and I. A. Walmsley, "Spectral phase interferometry for direct electric-field reconstruction of ultrashort optical pulses," *Opt. Lett.* **23**, 792 (1998).
264. P. Baum, S. Lochbrunner, and E. Riedle, "Zero-additional-phase SPIDER: full characterization of visible and sub-20-fs ultraviolet pulses," *Opt. Lett.* **29**, 210 (2004).
265. M. Hirasawa *et al.*, "Sensitivity improvement of spectral phase interferometry for direct electric-field reconstruction for the characterization of low-intensity femtosecond pulses," *Appl. Phys. B.* **74**, s225 (2002).
266. C. Dorrer, P. Londero, and I. A. Walmsley, "Homodyne detection in spectral phase interferometry for direct electric-field reconstruction," *Opt. Lett.* **26**, 1510 (2001).
267. A. Monmaryrant *et al.*, "Time-domain interferometry for direct electric-field reconstruction by use of an acousto-optic programmable filter and a two-photon detector," *Opt. Lett.* **28**, 278 (2003).
268. E. M. Kosik *et al.*, "Interferometric technique for measuring broadband ultrashort pulses at the sampling limit," *Opt. Lett.* **30**, 326 (2005).
269. Z. Guang *et al.*, "Complete characterization of a spatiotemporally complex pulse by an improved single-frame pulse-measurement technique," *J. Opt. Soc. Am. B* **31**, 2736 (2014).
270. M. Louisy *et al.*, "Compact single-shot d-scan setup for the characterization of few-cycle laser pulses," *Appl. Opt.* **56**, 9084 (2017).
271. K. Y. Kim, I. Alexeev, and H. M. Milchberg, "Single-shot supercontinuum spectral interferometry," *Appl. Phys. Lett.* **81**, 4124 (2002).

272. J. K. Wahlstrand, S. Zahedpour, and H. M. Milchberg, "Optimizing the time resolution of supercontinuum spectral interferometry," *J. Opt. Soc. Am. B* **33**, 1476 (2016).
273. D. Patel *et al.*, "Simplified single-shot supercontinuum spectral interferometry," *Opt. Express* **28**, 11023 (2020).
274. S. P. Le Blanc *et al.*, "Single-shot measurement of temporal phase shifts by frequency-domain holography," *Opt. Lett.* **25**, 764 (2000).
275. J. P. Geindre *et al.*, "Frequency-domain interferometer for measuring the phase and amplitude of a femtosecond pulse probing a laser-produced plasma," *Opt. Lett.* **19**, 1997 (1994).
276. S. W. Hancock, S. Zahedpour, and H. M. Milchberg, "Transient-grating single-shot supercontinuum spectral interferometry (TG-SSSI)," *Opt. Lett.* **46**, 1013 (2021).
277. A. B. Stilgoe, T. A. Nieminen, and H. Rubinsztein-Dunlop, "Controlled transfer of transverse orbital angular momentum to optically trapped birefringent microparticles," *Nat. Photonics* **16**, 346 (2022).
278. Y. Hu, *et al.*, "Structured transverse orbital angular momentum probed by a levitated optomechanical sensor," *Nat. Commun.* **14**, 2638 (2023).
279. Y. Fang *et al.*, "Structured electrons with chiral mass and charge," *Science* **385**, 183 (2024).
280. M. Sakamoto *et al.*, "Chirogenesis and amplification of molecular chirality using optical vortices," *Angew. Chem., Int. Ed.* **60**, 12819 (2021).
281. Q. Cao *et al.*, "Propagation of transverse photonic orbital angular momentum through few-mode fiber," *Adv. Photonics* **5**, 036002 (2023).
282. S. Huang *et al.*, "Spatiotemporal vortex strings," *Sci. Adv.* **10**, eadn6206 (2024).
283. J. Huang *et al.*, "Optical nonlocal meta-grating computing spatiotemporal differentiation," *Research Square Preprint* (2024).
284. F. Sun *et al.*, "Generation of isolated attosecond electron sheet via relativistic spatiotemporal optical manipulation," *Phys. Rev. Res.* **6**, 013075 (2024).
285. C. Zhang, D. Zhang, and B. Xie, "Generation of γ-photons and pairs with transverse orbital angular momentum via spatiotemporal optical vortex pulse," arXiv:2403.16414 (2024).
286. Y. Chen *et al.*, "Atomic photoionization by spatiotemporal optical vortex pulses," *Phys. Rev. A* **107**, 033112 (2023).
287. L. Zhang, L. Ji, and B. Shen, "Intense harmonic generation driven by a relativistic spatiotemporal vortex beam," *High Power Laser Sci.* **10**, e46 (2022).
288. M. Diouf *et al.*, "Demonstration of speckle resistance using space–time light sheets," *Sci. Rep.* **12**, 14064 (2022).
289. H. E. Kondakci, M. A. Alonso, and A. F. Abouraddy, "Classical entanglement underpins the invariant propagation of space–time wave packets," *Opt. Lett.* **44**, 2645 (2019).
290. M. Diouf *et al.*, "Interferometric phase stability from Gaussian and space–time light sheets," *Optica* **10**, 1161 (2023).
291. R. Wang, *et al.*, "Single-antenna super-resolution positioning with nonseparable toroidal pulses," *Commun. Phys.* **7**, 356 (2024).
292. S. Kaim *et al.*, "Stretching and compressing of short laser pulses by chirped volume Bragg gratings: analytic and numerical modeling," *Opt. Eng.* **53**, 051509 (2014).
293. L. Glebov *et al.*, "Volume-chirped Bragg gratings: monolithic components for stretching and compression of ultrashort laser pulses," *Opt. Eng.* **53**, 051514 (2014).
294. O. Mhibik *et al.*, "Rotated chirped volume Bragg gratings for compact spectral analysis," *Opt. Lett.* **48**, 1180 (2023).
295. M. Yessenov *et al.*, "Ultra-compact synthesis of space-time wave packets," *Opt. Lett.* **48**, 2500 (2023).
296. C. Guo *et al.*, "Structured 3D linear space–time light bullets by nonlocal nanophotonics," *Light Sci. Appl.* **10**, 160 (2021).
297. J. Cheng *et al.*, "Compact device for the generation of toroidal spatiotemporal optical vortices," *Opt. Lett.* **49**, 4646 (2024).
298. A. M. Shaltout *et al.*, "Spatiotemporal light control with frequency-gradient metasurfaces," *Science* **365**, 374 (2019).
299. Z. Ji *et al.*, "Photocurrent detection of the orbital angular momentum of light," *Science* **368**, 763 (2020).
300. Q. Cao, P. Zheng, and Q. Zhan, "Vectorial sculpturing of spatiotemporal wavepackets," *APL Photonics* **7**, 096102 (2022).
301. S. Sederberg *et al.*, "Vectorized optoelectronic control and metrology in a semiconductor," *Nat. Photon.* **14**, 680 (2020).
302. K. Jana *et al.*, "Reconfigurable electronic circuits for magnetic fields controlled by structured light," *Nat. Photonics* **15**, 622 (2021).
303. Y. Shen *et al.*, "Optical skyrmions and other topological quasiparticles of light," *Nat. Photonics* **18**, 15 (2024).
304. Y. Shen *et al.*, "Topological transformation and free-space transport of photonic hopfions," *Adv. Photonics* **5**, 015001 (2023).
305. W. Lin *et al.*, "Space-time hopfion crystals," arXiv:2406.06096 (2024).
306. R. Fickler *et al.*, "Quantum entanglement of high angular momenta," *Science* **338**, 640 (2012).
307. T. Stav *et al.*, "Quantum entanglement of the spin and orbital angular momentum of photons using metamaterials," *Science* **361**, 1101 (2018).
308. M. E. Durst, G. Zhu, and C. Xu, "Simultaneous spatial and temporal focusing in nonlinear microscopy," *Opt. Commun.* **281**, 1796 (2008).
309. B. Sun *et al.*, "Four-dimensional light shaping: manipulating ultrafast spatiotemporal foci in space and time," *Light Sci. Appl.* **7**, 17117 (2018).
310. D. Oron and Y. Silberberg, "Spatiotemporal coherent control using shaped, temporally focused pulses," *Opt. Express* **13**, 9903 (2005).
311. F. He *et al.*, "Characterization and control of peak intensity distribution at the focus of a spatiotemporally focused femtosecond laser beam," *Opt. Express* **22**, 9734 (2014).
312. M. Greco *et al.*, "Intuitive analysis of space-time focusing with double-ABCD calculation," *Opt. Express* **20**, 14244 (2012).
313. K. Robert *et al.*, "Enhancing precision in fs-laser material processing by simultaneous spatial and temporal focusing," *Light Sci. Appl.* **3**, e169 (2014).
314. W. Cheng, X-L. Liu, and P. Polynkin, "Simultaneously spatially and temporally focused femtosecond vortex beams for laser micromachining," *J. Opt. Soc. Am. B* **35**, B16 (2018).